SINGLE MOLECULE STUDIES IN A NANOFLUDIC CHANNEL: DETECTION AND SORTING FOR EPIGENETIC ANALYSIS

A Dissertation

Presented to the Faculty of the Graduate School

of Cornell University

in Partial Fulfillment of the Requirements for the Degree of

Doctor of Philosophy

by

Benjamin R. Cipriany

May 2012

SINGLE MOLECULE STUDIES IN A NANOFLUDIC CHANNEL:
DETECTION AND SORTING FOR EPIGENETIC ANALYSIS

Benjamin R. Cipriany, Ph.D.
Cornell University 2012

Microfluidics and nanofluidics have recently emerged as analytical tools for the study of biology. These devices have enabled the miniaturization of biological sample preparation and detection methods, toward consuming less sample volume and improving the sensitivity and speed of analysis.

This thesis explores methods for rapid detection and sorting of individual biomolecules within a nanofluidic channel. In these devices, constructed using thin-film processing techniques, attoliter-scale volume confinement is formed to isolate individual, fluorophore-labeled biomolecules in solution for absolute quantification. These devices enable studies of the unique attributes of each molecule, often masked in ensemble-averaged measurements. Statistical sampling of many molecules is achieved by voltage-actuated, electrokinetic flow within the nanofluidic device to precisely control molecule analysis rate and achieve high throughput single molecule detection (SMD).

This nanofluidic technology is applied to epigenetic analysis, enabling the study of epigenetic modifications at a single molecule level. Viable epigenetic analysis within a nanofluidic device is demonstrated using chromatin, DNA bound with histone proteins, which is shown to remain in its native state during nanofluidic confinement and electrokinetic flow under physiologically-relevant conditions. Detection of an epigenetic modification, DNA methylation, is also demonstrated to elucidate its potential for detecting multiple epigenetic marks on an individual

molecule.

Subsequently, an architecture for automated, high-speed sorting of individual molecules is developed. In this architecture, digital signal processing methods are implemented in a field programmable gate array to achieve real-time SMD. An electric circuit model is developed to actuate and switch electrokinetic flow of molecules, partitioning them into branches of a bifurcated nanofluidic device. An optical system for parallel SMD is realized to experimentally validate the actuation of molecule sorting in-situ. Combined, these components are utilized in automated, fluorescence-activated sorting of individual, methylated DNA molecules, which were then collected for further analysis. This device is reconfigurable and can be generalized for application to fluorescence-activated separations of other molecule types.

Finally, a study of various methods for optofluidic integration is presented. The optical properties of fused-silica, silicon nitride, polydimethylsiloxane, hydrogen silisequioxane, and chemical vapor deposited oxides are investigated to consider their use in SMD applications requiring ultra-low autofluorescence and high confinement of the optical probe volume. Findings were then applied to form an optical waveguide as an fluorescence excitation source toward the dense integration of optical and nanofluidic components.

BIOGRAPHICAL SKETCH

Benjamin R. Cipriany was born and raised in the state of Ohio. In 1999, he graduated high school, joined the Battelle Memorial Institute (Columbus, Ohio) as a research intern, and also began studies at the Ohio State University. Ben completed his Bachelor of Science degree in Electrical and Computer Engineering in 2003, graduating cum laude and with distinction for his undergraduate thesis in field effect transistors for biological sensing. He continued as a full-time staff researcher at Battelle from January 2004 through August 2005, working to realize his inventions in silicon nanophotonics. Ben returned to school in August 2005 to pursue graduate studies in Electrical and Computer Engineering at Cornell University. Following graduation with his Ph.D., Ben will be working as a TCAD engineer at IBM to develop computational tools that model semiconductor fabrication processes for next-generation planar and FinFET transistor technologies.

To my family.

ACKNOWLEDGEMENTS

If you were to read nothing else of my dissertation or know not what is my greatest contribution to science deserving of a Ph.D., you should know that I have embraced an epic journey filled with passion, people, and perseverance that is surely the blessing of the Lord Jesus Christ - to Him be all glory. Amen.

I would like to bestow my sincere, heartfelt thanks to all of the following people who have been a part of my graduate years (and before) at Cornell:

To my advisor and special committee chair, Prof. Harold Craighead. I continue to be in awe of your gift to reduce complicated matters to a simple form where their essence can be resolved with perfect clarity. Through our discussions and careful listening, I have learned a great deal about myself and techniques for presentation to a wide variety of audiences. Most importantly, you have honed my ability to ask critical questions and evaluate their response, which in my opinion is the most enduring skill for lifelong service as a Ph.D. I aspire to attain your expert clarity during my lifetime of scientific service. I would also like to thank you for your trust. Throughout my graduate career, you have helped me to enjoy great scientific freedom, financial support to build entire labs, a collaborative yet independent working environment, and opportunities to attend conferences and study with peers around the world. You have also trusted me to serve in your very own capacity in the classroom, at conferences, in organizing the group, and in guiding your future protege. To me, there is no greater compliment than your willingness to extend such trust to a student and for this I am truly grateful. I hope our interactions will continue for many years.

To my special committee members, Edwin Kan and Richard Lovelace, who have been very supportive of my scientific path despite its unusual progression. The varied and interdisciplinary aspects of this dissertation are a tribute to both

of their excellent classroom teaching and intellectual flexibility for exploring interdisciplinary extensions of their core academic competencies.

To my collaborators in Prof. Soloway's lab - Paul Soloway, Patrick Murphy, Jim Hagarman, Jim Putnam, and (visiting scientist) Prof. Ruqian Zhao. I have deeply enjoyed the scientific challenge of our work in epigenetics and the opportunity to collaborate on such a fascinating topic. You have opened my eyes to molecular biology and your continual enthusiasm has been contagious throughout - it has been a pleasure to work with you. I sincerely hope that our labors will continue as a fruitful collaboration and that our jointly developed nanofluidic platform will find its 'calling' within the tool set for epigenetic analysis.

To Rob Ilic for his mentorship as a scientist, advocate for my career and capabilities, and for his friendship. I have known Rob the longest of anybody at Cornell, stretching back to my first days as an industrial user (June 2004) at the Cornell NanoScale Facility. Rob is a very talented scientist and has taught me many of the nanofabrication skills I now possess. He was an advocate for me to join the Craighead group and come to Cornell. We have enjoyed many discussions, scientific and personal, throughout the years whether on a hiking trail, working all night in the cleanroom, eating one of our innumerable meals at his favorite 4 restaurants in Ithaca (Chili's, Friendly's, Napoli's, or Zaza's), or just chilling in his office while he played the guitar. I have gathered a long list of nicknames from Rob over the years which have made life at Cornell more fun, raised enthusiasm within the Craighead group, and caused numerous CNF staff members to only know me as 'Benny'.

To the experienced cleanroom users that mentor new users with their guidance and enjoyable discussion - Steve Jones (for etch advice and promises for future limousine driver services if/when I win the Nobel Prize), Marcus Gingrich (for

general processing advice and for lively football discussion), and Gregory Simelgor (for expert guidance on just about everything in the cleanroom, for helping me ebeam evaporate 3 microns of Al one time, for emergency stay on his couch, and for numerous thought provoking dinner discussions with Rob).

To the staff at the Cornell Nanoscale facility (CNF), Mike Skvarla, Meredith Metzler, Daron Westly, Garry Bordonaro, Jerry Drumheller, Lynn Rathbun, Kelly Baker, Kathy Springer, who have been great friends and provide excellent support to the varied and chaotic needs of both the Cornell graduate school and users nationwide.

To the many Craighead group members with whom I have enjoyed the privilege of working during these many years. These are my friends and professional colleagues, with whom I hope my day-to-day worklife has made a positive influence. They are an exceptional collection of scientists and people that have made my years at Cornell rich and memorable. Pouring over this list of names brings me a flood of emotion for our times spent together. (Please forgive me if I have left anyone from this list, it is by no means intentional). In some resemblance of order:

Generation 1: Rob Reichenbach, Keith Aubin, Kevan Samiee, Rob Ilic, Grant Meyer, Samuel Stavis, Christian Reccius, Elizabeth Strychalski, Kalina Jordanova, Leon Bellan, Karen Jarvis, Tiberiu Onuta, and Tobias Fuhrmann.

Generation 2: Philip Waggoner, Seung-min Park, Stephen Levy, Jos Moran-Mirabal, Kristin Ceniccola, Christine Tan (more on her later), Nitin Malik, and Juraj Topolancik.

Generation 3: David Latulippe, Christopher Kelly, Jaime Benitez, Robert Barton, Aline Cerf, Thomas Alava, Kylan Szeto, Daniel Joe, Christopher Wallin, and Harvey Tian.

To my 7th grade algebra teacher for forging the title 'Dr. Cip.' Over the years, this title has become both a goal and a reminder of my potential. Though the name has become a bit thread bare from usage over the years, it is a great reminder of how far I have come, how many people have been a part of the journey to educate and uplift me to this great accomplishment, and the importance of encouraging those around me to achieve their full potential.

To the government and taxpayers of the United States of America, who through the National Science Foundation (NSF), Nanobiotechnology Center (NBTC), Cornell NanoScale Facility (CNF), and the National Institutes of Health (NIH), have financially supported my graduate work. The importance of your long-term investment in my education and to that of my peers is paramount to our country's future and to the advancement of science and engineering.

To my dear friends at the Protestant Cooperative Ministries on campus. Rev. Taryn Mattice and her family, Andy Poshadel, Eric Monkman and Katie White, Luwam Dirar, Johanna and Nate Kingsley, Gill, Prof. Ken Hover, and the list goes on and on. You have given me refuge, support, understanding, and Christian love from my first, lonely days at Cornell - you are undoubtedly my family away from home.

To my family, with tears of joy. We did this together. To my graduate school colleague and wife, Christine - Your life has brought light to my darkest moments, laughter to my daily existence, love to last a lifetime, new perspectives to challenge my thinking, and companionship to traverse the journey of life. To my parents, Darrell and Suzanne - for your truly unending support and love, I could not ask for better parents. To my grandparents, Martha and Louis - for helping me live great dreams and remember my blessings. To my brother, Tim - for your love and encouragement. To my extended family for all your support.

TABLE OF CONTENTS

LIST OF TABLES

LIST OF FIGURES

CHAPTER 1

INTRODUCTION

Micro- and nanofluidic systems have emerged as miniaturized analytical and preparatory tools for the study of chemistry and biology. These systems have been applied to topics ranging broadly from environmental studies to early cancer detection, ultimately to improve the accuracy, speed, and sensitivity of diagnostic measurements. Using thin-film processing techniques adapted from the semiconductor industry, these structures can be formed with exquisite spatial control of device features. This has allowed sculpting of bio-compatible materials, such as dielectrics and optical quality polymers, into devices with micrometer and nanometer dimensions for the analysis of DNA, RNA, and proteins. Furthermore, these device dimension permit analysis on significantly less sample material than is required by existing analytical methods. Through experimental studies, scientists have developed the ability to detect, manipulate, and analyze material within these fluidic structures to achieve sophisticated workflows within a chip-scale device.

To achieve analytical functions, micro- and nanofluidic devices guide the flow of analyte to an interrogation region for transduction with an optical [1–4], electrical [5–9], or mechanical [10–12] probe. This transduction can occur through mechanisms such as fluorescence [13–17], chemiluminescence [18–20], impedance variations [21, 22], or modifications to mechanical resonance [23]. For example, fluorophore-labeled biomolecules within a fluidic channel can be probed using a focused laser beam to excite fluorescence from biomolecules as they undergo binding. However, since the position and quantity of molecules within this laser beam can dramatically influence the fluorescence output, it is challenging to draw conclusions regarding the absolute quantity of sample under analysis. Therefore, by reducing the fluidic device cross-section to dimensions on the order of the optical

probe or smaller, the beam can interrogate the channel uniformly and probe only one molecule at a time.

Preparatory functions in micro- and nanofluidic devices differentiate the biological molecules within flow using passive structures or active transduction with a feedback response to separate and extract samples with specific properties. These separations are challenging given the Stokes flow within these fluidic devices. Passive separations are performed by pillars [24], monoliths [25, 26], and bead-packed structures [27] that present a physical obstacle for separating molecules based upon their average match or mismatch to these filters. However, to extract particularly rare molecules from within a complex mixture, active methods are used to separate specific cells or large particles individually, limited primarily by the signal to noise in transduction within volumes ranging from microliter to picoliter. Nanofluidics probed with an optical beam can achieve volume confinement within the attoliter range, dramatically reducing the measurement noise and present an opportunity for separating individual molecules.

1.1 Nanofluidics for Single Molecule Epigenetic Analysis

Studies at the single molecule level serve to investigate the role of each molecule in defining and guiding the life cycle of biological processes. Many of these processes are controlled by rare events that initiate the onset of disease, silence genes, or alter cellular differentiation and development, thereby playing a critical role in the life or death of a biological system. These events are often lost in ensemble-averaged measurements, which effectively disable our observation of the rich, heterogeneity within these biological systems.

Fluorescence detection in nanofluidics represents a unique way of performing analytical studies on biomolecules, that combines the strengths of confocal fluorescence microscopy-based detection and nanofluidics for single molecule confinement

to create a platform for high-throughput single molecule studies. Together, these systems are greater than the sum of their parts. For example, confocal microscopy detection of single molecule fluorescence occurs with high signal-to-noise, but is limited to probing spatial volumes limited by diffraction. However, nanofluidics can confine fluid volumes to sub-diffraction limited scales, thus allowing a samples to be investigated at physiologically-relevant concentrations to more accurately represent their in-vivo properties.

The technologies and methods described within this dissertation are aimed to develop nanofluidic devices for access to single molecule detection, analysis, and manipulation. To provide an application context for the nanofluidic device, this work has fortuitously coincided with the emergence of the field of epigenomics. This field represents a paradigm shift from the Mendelian-model for genetic inheritance wherein parental chromosomes each contribute to the specific phenotype, or traits, coded within the deoxyribonucleic acid (DNA) sequence of their offspring. However, epigenomics has now demonstrated the role of chemical and physical modifications to chromatin that lead to major changes in phenotype, without altering the underlying DNA sequence and occur as the result of environment or dietary factors. Yet, this field would benefit from technology development in analysis methods that explore the complex relationship of these epigenetic marks. Current techniques employ chromatin immunoprecipitation (ChIP) or bisulfite sequencing, to address one type of epigenetic mark at a time and are performed in a serially recursive process, which is both labor intensive and requires large quantities of input material for epigenome-wide analysis. These limitations have been the motivational genesis for developing nanofluidic devices described in this dissertation.

1.2 Organization of this Dissertation

This chapter has highlighted significant scientific and engineering progress in micro- and nanofluidic devices. A discussion of ensemble-measurement limitations has motivated the study of biological systems at the single molecule level. This dissertation develops and demonstrates nanofluidic devices as analytical and preparatory tools for the study of epigenetics, by demonstrating detection, sorting, and recovery of fluorescently-labeled molecules of DNA and chromatin bearing specific epigenetic modifications.

Chapter 2 describes the development of a nanofluidic device to simultaneously detect multiple fluorescent marks on a single chromatin or DNA molecule. Using time-correlated, multi-color detection, these devices are shown to preserve chromatin structural integrity during analysis and to enable detection of DNA methylation, an epigenetic modification, at the single molecule level.

Chapter 3 develops the application of a bifurcated nanofluidic device for automated, fluorescence-activated sorting of single molecules. Capabilities for real-time single molecule analysis are developed using digital signal processing techniques that are executed within hardware to evaluate fluorescence signatures in real-time. The selection of molecules bearing specific fluorescence signatures, representative of epigenetic modifications, demonstrate this device as a preparatory system for extracting individual molecules. Extracted molecules are further analyzed by quantitative polymerase chain reaction (qPCR).

Chapter 4 explores the integration of thin film processes to embed probes that optical excite and detect molecules within a nanofluidic device. Spin-on-glass films are demonstrated to hermetically encapsulate ridge-shaped structures, like an optical waveguide or electrodes or plasmon-focusing antenna, while maintaining low autofluorescence requirements for single molecule detection. These open the pos-

sibility for dense integration of many devices operating in parallel toward enabling single molecule epigenetic studies at the whole-genome scale.

Chapter 5 provides concluding remarks and a perspective on future opportunities for nanofluidic technologies.

References

[1] G. Cote, "Raman detection in microchips and microchannels," in *Optofluidics* (A. Hawkins and H. Schmidt, eds.), New York: Taylor and Francis Books, Inc, 2010.

[2] X. Fan, "Ring resonators," in *Optofluidics* (A. Hawkins and H. Schmidt, eds.), New York: Taylor and Francis Books, Inc, 2010.

[3] M. Foquet, J. Korlach, W. Zipfel, W. W. Webb, and H. G. Craighead, "Dna fragment sizing by single molecule detection in submicrometer-sized closed fluidic channels," *Analytical Chemistry*, vol. 74, no. 6, pp. 1415–1422, 2002.

[4] S. M. Stavis, S. C. Corgie, B. R. Cipriany, and H. G. Craighead, "Single molecule analysis of bacterial polymerase chain reaction products in submicrometer fluidic channels," *Biomicrofluidics*, vol. 1, no. 3, 2007.

[5] T. Cohen-Karni, Q. Qing, Q. Li, Y. Fang, and C. M. Lieber, "Graphene and nanowire transistors for cellular interfaces and electrical recording," *Nano Letters*, vol. 10, no. 3, pp. 1098–1102, 2010.

[6] X. P. A. Gao, G. F. Zheng, and C. M. Lieber, "Subthreshold regime has the optimal sensitivity for nanowire fet biosensors," *Nano Letters*, vol. 10, no. 2, pp. 547–552, 2010.

[7] S. W. Kowalczyk, M. W. Tuijtel, S. P. Donkers, and C. Dekker, "Unraveling single-stranded dna in a solid-state nanopore," *Nano Letters*, vol. 10, no. 4, pp. 1414–1420, 2010.

[8] F. Patolsky, G. Zheng, and C. M. Lieber, "Nanowire sensors for medicine and the life sciences," *Nanomedicine*, vol. 1, no. 1, pp. 51–65, 2006.

[9] E. Stern, J. F. Klemic, D. A. Routenberg, P. N. Wyrembak, D. B. Turner-Evans, A. D. Hamilton, D. A. LaVan, T. M. Fahmy, and M. A. Reed, "Label-free immunodetection with cmos-compatible semiconducting nanowires," *Nature*, vol. 445, no. 7127, pp. 519–522, 2007.

[10] R. A. Barton, B. Ilic, S. S. Verbridge, B. R. Cipriany, J. M. Parpia, and H. G. Craighead, "Fabrication of a nanomechanical mass sensor containing a nanofluidic channel," *Nano Letters*, vol. 10, no. 6, pp. 2058–2063, 2010.

[11] W. H. Grover, A. K. Bryan, M. Diez-Silva, S. Suresh, J. M. Higgins, and S. R. Manalis, "Measuring single-cell density," *Proceedings of the National Academy*

of Sciences of the United States of America, vol. 108, no. 27, pp. 10992–10996, 2011.

[12] M. Javanmard, A. H. Talasaz, M. Nemat-Gorgani, F. Pease, M. Ronaghi, and R. W. Davis, "Electrical detection of protein biomarkers using bioactivated microfluidic channels," *Lab on a Chip*, vol. 9, no. 10, pp. 1429–1434, 2009.

[13] M. Foquet, J. Korlach, W. R. Zipfel, W. W. Webb, and H. G. Craighead, "Focal volume confinement by submicrometer-sized fluidic channels," *Analytical Chemistry*, vol. 76, no. 6, pp. 1618–1626, 2004.

[14] B. R. Cipriany, R. Q. Zhao, P. J. Murphy, S. L. Levy, C. P. Tan, H. G. Craighead, and P. D. Soloway, "Single molecule epigenetic analysis in a nanofluidic channel," *Analytical Chemistry*, vol. 82, no. 6, pp. 2480–2487, 2010.

[15] J. M. Moran-Mirabal, S. C. Corgie, J. C. Bolewski, H. M. Smith, B. R. Cipriany, H. G. Craighead, and L. P. Walker, "Labeling and purification of cellulose-binding proteins for high resolution fluorescence applications," *Analytical Chemistry*, vol. 81, no. 19, pp. 7981–7987, 2009.

[16] J. T. Mannion and H. G. Craighead, "Nanofluidic structures for single biomolecule fluorescent detection," *Biopolymers*, vol. 85, no. 2, pp. 131–143, 2007.

[17] P. M. Lundquist, C. F. Zhong, P. Q. Zhao, A. B. Tomaney, P. S. Peluso, J. Dixon, B. Bettman, Y. Lacroix, D. P. Kwo, E. McCullough, M. Maxham, K. Hester, P. McNitt, D. M. Grey, C. Henriquez, M. Foquet, S. W. Turner, and D. Zaccarin, "Parallel confocal detection of single molecules in real time," *Optics Letters*, vol. 33, no. 9, pp. 1026–1028, 2008.

[18] B. F. Liu, M. Ozaki, H. Hisamoto, Q. M. Luo, Y. Utsumi, T. Hattori, and S. Terabe, "Microfluidic chip toward cellular atp and atp-conjugated metabolic analysis with bioluminescence detection," *Analytical Chemistry*, vol. 77, no. 2, pp. 573–578, 2005.

[19] P. J. Viskari and J. P. Landers, "Unconventional detection methods for microfluidic devices," *Electrophoresis*, vol. 27, no. 9, pp. 1797–1810, 2006.

[20] J. Yakovleva, R. Davidsson, M. Bengtsson, T. Laurell, and J. Emneus, "Microfluidic enzyme immunosensors with immobilised protein a and g using chemiluminescence detection," *Biosensors and Bioelectronics*, vol. 19, no. 1, pp. 21–34, 2003.

[21] L. Yang and R. Bashir, "Electrical/electrochemical impedance for rapid detection of foodborne pathogenic bacteria," *Biotechnology Advances*, vol. 26, no. 2, pp. 135–150, 2008.

[22] Z. W. Zou, J. H. Kai, M. J. Rust, J. Han, and C. H. Ahn, "Functionalized nano interdigitated electrodes arrays on polymer with integrated microfluidics for direct bio-affinity sensing using impedimetric measurement," *Sensors and Actuators a-Physical*, vol. 136, no. 2, pp. 518–526, 2007.

[23] P. S. Waggoner, C. P. Tan, and H. G. Craighead, "Microfluidic integration of nanomechanical resonators for protein analysis in serum," *Sensors and Actuators B-Chemical*, vol. 150, no. 2, pp. 550–555, 2010.

[24] J. Han and H. G. Craighead, "Separation of long dna molecules in a microfabricated entropic trap array," *Science*, vol. 288, no. 5468, pp. 1026–1029, 2000.

[25] F. Svec, E. C. Peters, D. Sykora, and J. M. J. Frechet, "Design of the monolithic polymers used in capillary electrochromatography columns," *Journal Of Chromatography A*, vol. 887, no. 1-2, pp. 3–29, 2000.

[26] C. Yu, M. H. Davey, F. Svec, and J. M. J. Frechet, "Monolithic porous polymer for on-chip solid-phase extraction and preconcentration prepared by photoinitiated in situ polymerization within a microfluidic device," *Analytical Chemistry*, vol. 73, no. 21, pp. 5088–5096, 2001.

[27] J. Wen, L. A. Legendre, J. M. Bienvenue, and J. P. Landers, "Purification of nucleic acids in microfluidic devices," *Analytical Chemistry*, vol. 80, no. 17, pp. 6472–6479, 2008.

CHAPTER 2

SINGLE CHROMATIN ANALYSIS AT THE NANOSCALE

2.1 Introduction

Chromatin within eukaryotic cells includes DNA and histone proteins assembled on DNA into the nucleosome [1]. The DNA sequence carries the genetic code and controls inheritance of traits, however, reversible covalent modifications to specific DNA sequences and their associated histones can influence how the underlying DNA is utilized and can therefore also control traits [2, 3]. These have been referred to as epigenetic modifications. The most common epigenetic modification to DNA in mammals is methylation and hydroxymethylation of DNA, either of which may be placed on the fifth carbon of the cytosine pyrimidine ring. A host of modifications including methylation, acetylation, ribosylation, phosphorylation, sumoylation, ubiquitylation and citrullination occur at more than 30 amino acid residues of the four core histones within the nucleosome.

Specific changes in epigenetic state that occur genome wide appear to regulate cellular differentiation during development [4]. Perturbations in normal epigenetic state in mature tissues contribute to initiation and progression of cancer and other diseases [5]. Additionally, evidence indicates epigenetic states are influenced by environmental variables including diet [6], environmental toxins [7] and maternal behaviors [8]. Given the fundamental role that epigenetic mechanisms play in normal development, environmental responses and how their perturbation affect disease state, there is increasing effort devoted to characterize the human epigenome [9].

Current methods for epigenomic analysis depend on the epigenetic mark queried.

[0]This chapter is reprinted (adapted) with permission from B. R. Cipriany, R. Q. Zhao, P. J. Murphy, S. L. Levy, C. P. Tan, H. G. Craighead, and P. D. Soloway, Single molecule epigenetic analysis in a nanofluidic channel, Analytical Chemistry, vol. 82, no. 6, pp 24802487, 2010. Copyright 2010 American Chemical Society

Histone modifications are most commonly detected using chromatin immunoprecipitation (ChIP), in which modification-specific antibodies are used to immunoprecipitate the associated DNA, which is then detected by hybridization to microarray (ChIP-chip) [10] or deep sequencing (ChIP-seq) [11]. DNA methylation can also be detected by immunoprecipitation using a methylcytosine antibody [12], or with bisulfite sequencing, which offers more comprehensive analysis of DNA methylation states [13]. Genome wide epigenomic analyses using antibodies often use on the order of $10^6 - 10^7$ cells. ChIP has been used with few as 100 cells, however, with this few cells the analysis was locus specific and not genome wide [14]. A far more significant limitation is encountered when studies seek to determine whether or not two or more epigenetic marks are coincident within the genome. Analysis of each epigenetic mark requires an independent immunoprecipitation. When precipitating chromatin from an ensemble of cells with different antibodies, it is difficult to distinguish true coincidence of the detected marks from the existence of multiple populations within the ensemble, each with a different epigenomic profile. This can be somewhat overcome with sequential ChIP, where the material precipitated by one antibody is re-ChIPed with a second antibody [15]. However, these techniques are not amenable to genome wide analysis or for studies in which more than two epigenetic marks are investigated.

Nanofluidic platforms that combine high throughput detection and analysis of single chromatin fragments can overcome the limitations of existing epigenomic methods. Such platforms have been used to size femtogram quantities of DNA [16], to study microRNA gene expression [17], and to quantify mRNA transcript levels [18] and PCR amplification products [19]. However, they have not been adapted for use with chromatin, nor used to examine epigenetic marks. Here we established the conditions for flowing and detecting single native chromatin

molecules through such a device by analyzing time-coincident fluorescent signatures of both the DNA and histone proteins within the chromatin at high throughput. In addition, we extended our analysis to study an epigenetic mark in naked DNA using conditions that paralleled our chromatin studies and a fluorescently labeled probe that can bind to methylated DNA. Our approach, which we refer to as SCAN (single-chromatin analysis at the nanoscale) is the first demonstration of single-molecule high-throughput epigenetic analysis.

2.2 Theoretical Background

2.2.1 Single Molecule Confinement

The observation and identification of single molecules requires distinct, unique identifiers or a physical volume not crowded by other interfering molecules. A single molecule observation implies a detection event that occurs rarely when compared to the total number of possible observations and is well-modeled using Poisson statistics. In our application, the Poisson probability density function describes the condition for single molecule observation or occupancy in a given volume of solution as determined by the concentration of the specie and the volume under investigation.

$$P_c(x) = \frac{e^{-c}c^x}{x!} \tag{2.1}$$

In this equation, c is the average number of molecules per unit volume and x is the number of molecules that instantaneously occupy that volume. Since $P_c(x > 1)$, the probability of observing more than one molecule at a time, is non-zero in most cases, there is a finite probability of detecting more than one molecule

at a time. This can introduce error into single molecule detection experiments [20, 21]. However, in highly dilute systems this contribution becomes virtually negligible. To minimize the probability of detecting more than one molecule at an instant, either the volume or the concentration of the solution, or both, must be reduced to achieve a desired $P_c(x > 1)$.

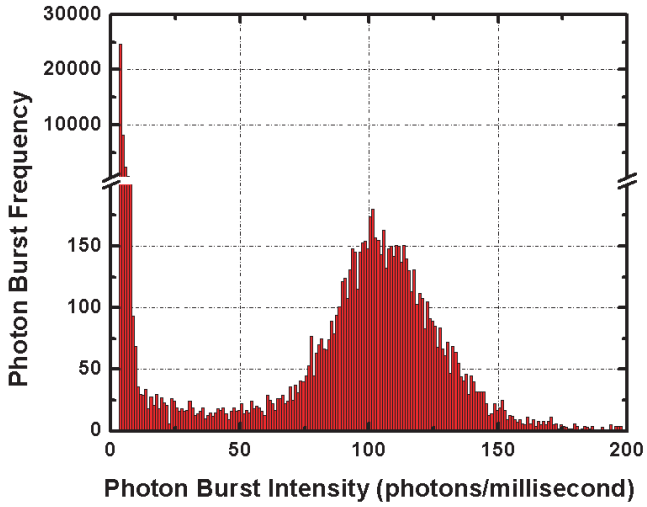

Figure 2.1: Photon counting histogram (PCH) illustrating the Poisson-distributed photon noise and a Gaussian-distributed population of single molecules each with a single fluorophore label. A threshold of 6 photons/ms would provide distinct separation between these distributions and a signal to noise ratio greater than 15.

In practice, most single molecule techniques utilize a threshold to separate single molecule signaling events from background-level observations, or noise, establishing a minimum signal to noise ratio (SNR) for detection. While the basis for threshold determination is discussed later, we note the tradeoff between detection sensitivity, or SNR, and measurement (or integration) time. In practice, the integration time and the method of molecule confinement affect detection throughput. For example, in wide-field imaging-based experiments where molecules can be affixed to a surface, the SNR is maximized by increasing image integration time,

but this reduces the number of molecules that can be observed in a given unit time [22, 23]. By contrast, in flow-driven experiments within microfluidic channels, the rate of flow controls the number of molecules observed within the imaging field in a given time, but imposes limits on the SNR if flow occurs too quickly. These observations indicate that SNR is inversely proportional to the number of molecules observed per unit time, a property which will be explored later in Fluorescence Correlation Spectroscopy (FCS). This dissertation emphasizes the use of optical methods for SMD, as distinguished and preferred from their electrical and mechanical counterparts, primarily due to the large SNRs that have been achieved and the availability of measurement tools that have made fluorescence-based techniques the 'gold standard' of detection in biomedical and analytical biochemistry fields [22, 24].

2.2.2 Electrokinetic Transport

Fluid Dynamics in Microfluidic and Nanofluidic Systems In this section I will provide a primer to briefly explore the fluid dynamics in micro- and nanofluidic systems. While it reflects my view and logical approach to these systems, I wish to recognize guidance from an excellent text by Prof. Brian Kirby [25] and the classroom teachings of Prof. Richard Lovelace.

We begin by considering an arbitrary volume through which fluid can flow using the continuity equation. This allows us to relate the time-dependent flow of mass through this volume to the total fluid flux across the surfaces that bound volume. This ensures the conservation of mass, adapted from Gauss's theorem, and is given by:

$$\frac{\partial}{\partial t}\int_V \rho dV = -\int_S (\rho \mathbf{u}) \cdot \mathbf{n} dA \tag{2.2}$$

Where ρ is the fluid density, V the volume of fluid, $\mathbf{u}$ the fluid velocity, $\mathbf{n}$ unit normal vector, and A the bounding area of surface. In its present form, it is assumed that the fluid density is a scalar constant. Therefore, our discussion applies only to Newtonian fluids that are incompressible. A further statement of this incompressible condition is:

$$\nabla \cdot (\rho \mathbf{u}) = \nabla \cdot \mathbf{u} = 0 \tag{2.3}$$

The incompressible condition is preserved in fluid systems with velocities less than the speed of sound (343 m/s in air) or, equivalently, where the non-dimensional Mach number (Ma) is much less than unity. This condition will be applicable for nearly every micro- and nanofluidic system, where typical flow velocities are considerably less than 1 m/s.

Next we make a statement about the conservation of momentum in fluids, more formally known as the Navier-Stokes equation. This is arguably one of the most profound and complicated nonlinear equations in all of continuum physics, which to this day has no formal derivation. It is the assembly of mathematical terms used to account for inertial components of a fluid flow and equate them to sheer and external forces. The full Navier-Stokes equation, following the simplification of the stress tensor, is given:

$$\rho \left(\frac{\partial \mathbf{u}}{\partial t} + \mathbf{u} \cdot \nabla \mathbf{u} \right) = -\nabla p + \eta \nabla^2 \mathbf{u} + \sum_i \mathbf{F_i} \tag{2.4}$$

This equation is often shown in differential form because all inertial terms are conveniently grouped on the left side of the equality and all stress induced effects from pressure, sheer, and external body forces have been summarized on the right. Take a moment to bask in the physical complexity so humbly represented

in this equation. The first inertial term, $\frac{\partial \mathbf{u}}{\partial t}$, describes time-dependent velocity changes or acceleration of the fluid flow. The second inertial term, $\mathbf{u} \cdot \nabla \mathbf{u}$ describes the momentum outflow from a unit of volume or, in other terms, the convective property. The right side terms describe the gradient of the internal pressure ∇p, the sheer of the velocity field $\nabla^2 \mathbf{u}$ for a solution of viscosity η, and the sum of all externally applied body forces $\mathbf{F_i}$.

Several carefully constructed observations can be used to simplify the Navier-Stokes equation for micro- and nanofluidic applications. The first observation extends from a dimensionless analysis of the dynamical similarity, or similtude, in fluidic systems using the Reynolds Number (Re). Using the condition for incompressible fluid flow and the Navier-Stokes equation, the Re number [26] is given :

$$Re = \frac{\rho U L}{\eta} \tag{2.5}$$

Where non-dimensional quantities describe U for velocity, l for length, ρ for fluid density, and η for fluid viscosity. Immediately, we note that the inertial component in the numerator and the viscous component in the denominator. Therefore, using an argument of similtude, for the same fluid velocity and viscosity, the Reynolds number will be altered by the characteristic length scale, L, causing fluids to behave in more inertial or viscous-dominated ways simply due to the conditions of confinement. For this reason, microfluidic systems have a Re < 1, causing viscous terms to dominate the fluid transport and laminar flow to occur. Our second observation follows - that inertial terms can ignored due to the predominantly steady and uni-directional nature of fluid flow, respectively stated as:

$$\frac{\partial \mathbf{u}}{\partial t} = 0 \tag{2.6}$$

$$\mathbf{u} \cdot \nabla \mathbf{u} = 0 \tag{2.7}$$

This allows us to remove the nonlinear terms of the Navier-Stokes equation, yielding an analytically tractable equation:

$$0 = -\nabla p + \eta \nabla^2 \mathbf{u} + \sum_i \mathbf{F_i} \tag{2.8}$$

This this equation is essentially an expression of a Stokes flow, sometimes called a creeping flow, which is special regime of laminar flow that is time reversible and superimposable. In the next section, we discuss how the pressure and force terms can be used to induce fluid or charge transport. While this formulation is useful for introductory purpose, this model does lack some accuracy when considering higher-order effects, such as ion concentration polarization, that arise from geometry [27–29].

Pressure Driven Transport in Microfluidics Using the applicable form of the Navier-Stokes equation 2.8, we now explore Poiseuille, or pressure-driven, flows in a microfluidic system. In pressure flow, the term for external forces is removed, further simplifying the Navier-Stokes equation to:

$$0 = -\nabla p + \eta \nabla^2 \mathbf{u} \tag{2.9}$$

To develop an appreciation for Poiseuille flow, we will consider a special case in a radially symmetric geometry, like that of a capillary, known as Hagen-Poiseuille flow.

$$\nabla p = \eta \nabla^2 \mathbf{u} \tag{2.10}$$

$$\frac{\partial p}{\partial z} = \eta(\frac{1}{r})\frac{\partial}{\partial r}(r\frac{\partial u_z}{\partial r}) \tag{2.11}$$

We assume that the applied pressure is uniform along the z-direction, such that $\frac{\partial p}{\partial z}$ is a constant and continue with the derivation:

$$\int \frac{\partial p}{\partial z} r dr = \eta \int \frac{\partial}{\partial r}(r\frac{\partial u_z}{\partial r})dr \tag{2.12}$$

$$\frac{\partial p}{\partial z}\frac{r^2}{2} + c_1 = \eta r \frac{\partial u_z}{\partial r} \tag{2.13}$$

$$\int (\frac{\partial p}{\partial z}\frac{r}{2\eta} + \frac{c_1}{\eta r})dr = \int \frac{\partial u_z}{\partial r} dr \tag{2.14}$$

$$\frac{\partial p}{\partial z}\frac{r^2}{4\eta} + \frac{c_1}{\eta}(\ln(r) + c_2) = u_z \tag{2.15}$$

Finally we apply the no-slip condition at the wall boundary, R_{wall}, of the capillary and note that the fluid velocity must be finite in the fluid body:

$$u_z(r = R_{wall}) = 0 \tag{2.16}$$

$$u_z(r = 0) < \infty \tag{2.17}$$

The result is a radially symmetric, parabolic-shaped solution for the velocity profile:

$$u_z = -\frac{1}{4\eta}\frac{\partial p}{\partial z}(R_{wall}^2 - r^2) \tag{2.18}$$

This parabolic velocity profile is an important result for Poiseuille flow microfluidic systems because it indicates a significant non-uniformity in the rate of transport over the cross-section. This property can be disadvantageous in molecule

separations that rely on retention or propagation time as an indicator of molecule property. It also indicates a challenge with device scaling, that pressure actuated transport has a limited range of usable channel dimensions before either the parabolic profile becomes unwieldy or pressures necessary to actuate flow are unrealistic. To further explore this point, let's examine the volumetric flow rate across the entire capillary:

$$V_z = \int_0^{R_{wall}} 2\pi r u_z dr \tag{2.19}$$

$$V_z = \frac{\partial p}{\partial z}\frac{R^4\pi}{8\eta} \tag{2.20}$$

In analogy to a linear circuit model obeying Ohm's law, $\Delta V = (\Delta I)R$, we can write the effective fluid resistance to pressure-driven actuation as:

$$R_{fluid} = \frac{\partial p}{\partial z}\frac{1}{V_z} = \frac{8\eta}{R^4\pi} \tag{2.21}$$

Therefore, the hydrostatic resistance to Poiseuille flow scales proportional to R^{-4}, placing a harsh penalty on scaling pressure flow to nanofluidic dimensions and motivating the use of electrokinetic transport.

A Comment on Electrokinetic Transport As we continue to reduce fluid channel geometries to the nanoscale, transport by pressure driven flow becomes impractical. Returning to the Navier-Stokes equation, we now consider the use of an applied electric field. Using the Coulomb force equation, we can relate an external body force to the applied electric field E on an arbitrary charge q:

$$\mathbf{F} = q\mathbf{E} = ze\mathbf{E} \tag{2.22}$$

More specifically, z is the valency of a charged ion (which can be positive or negative) in solution and e is the magnitude of an electron charge. Charges of positive polarity will be driven in the opposite direction of those with negative polarity. While this seems mathematically benign, this comment is critical in practical implementation, as negative ions or particles are often associated with electrophoretic transport and positive ions with electroosmotic transport. However, because the transport of fluid volume and/or charge from each method is complicated and interrelated, we often discuss the overall transport as electrokinetic.

Electroosmostic Transport in Nanofluidics To describe electroosmotic flow, we use the Navier-Stokes equation previously derived 2.8 and assume the system is isobaric. The external body force term is substituted with the Coulomb force:

$$0 = \eta \nabla^2 \mathbf{u} + q\mathbf{E} \tag{2.23}$$

To understand the basics of electroosmotic flow, we apply 2.23 and consider a simple geometry involving a charged surface, ρ_{fixed}, that bounds a distribution of ions in space. This ionic bulk represents the aqueous buffer solution used in most nanofluidic devices. Intuitively, we anticipate ion accumulation to occur at the wall, which screens the wall's fixed charged in a region called the electric double-layer (EDL). The EDL is a complicated layer of electrostatics that merits considerable discussion for nanofluidic devices [25], but for now we will use the Debye length, λ_D, to approximate the spatial extent of the EDL. Our observations indicate two regions for solving 2.23, one near the bounding wall and the other in the ionic bulk:

$$\rho_{fixed} = \begin{cases} 0 & \text{if } y >> \lambda_D \\ const & \text{if } 0 < y < \lambda_D \end{cases} \tag{2.24}$$

Using the first Maxwell equation we can relate the fixed surface charge to the gradient of the electric displacement vector $\mathbf{D}$ or the Laplacian of the vector potential ϕ.

$$\rho_{fixed} = \nabla \cdot \mathbf{D} = -\epsilon \nabla^2 \phi \tag{2.25}$$

This relationship is substituted into 2.23 and a unidirectional flow is assumed. Considering the region near the charged wall where ρ_{fixed} is non-zero:

$$\epsilon \mathbf{E} \nabla^2 \phi = \eta \nabla^2 \mathbf{u} \tag{2.26}$$

$$\epsilon E_x \frac{\partial^2 \phi}{\partial y^2} = \eta \frac{\partial^2 u_x}{\partial y^2} \tag{2.27}$$

$$\epsilon E_x \int_0^y \int_0^y \frac{\partial^2 \phi}{\partial y^2} dy dy = \eta \int_0^y \int_0^y \frac{\partial^2 u_x}{\partial y^2} dy dy \tag{2.28}$$

$$\epsilon E_x \phi + y C_1 + C_2 = \eta u_x \tag{2.29}$$

We then rearrange the solution to illustrate the electroosmotic flow velocity and apply boundary conditions: the no-slip boundary condition $u_x(y = 0) = 0$ at the wall and a finite-valued velocity such that $u_x(y = \infty) < \infty$. This results in an expression of the flow velocity near the wall:

$$u_x(y) = \frac{\epsilon E_x}{\eta} + \frac{y C_1 + C_2}{\eta} \tag{2.30}$$

$$u_x(y) = \frac{\epsilon E_x}{\eta} (\phi - \phi_{wall}) \tag{2.31}$$

A similar process of derivation is used to solve the velocity in the ionic bulk, where ρ_{fixed} is zero in 2.25. The resulting pair of equations for the velocity include:

$$u_x(y) = \begin{cases} \frac{\epsilon E_x}{\eta}(\phi - \phi_{wall}) & \text{near the wall: } 0 <= y <= \lambda_D \\ -\frac{\epsilon E_x}{\eta}\phi_{wall} & \text{in the bulk: } \lambda_D < y < \infty \end{cases} \tag{2.32}$$

Notice that unlike the result in 2.18 for Hagen-Poiseuille flow, this solution is independent of radius of the fluidic channel. You may also note that a net Coulomb force occurs near the wall, which is counter to the viscous shear force, but in the bulk there is no net force. This observation explains how the velocity profile is approximately uniform within the bulk of an electroosmotic flow, sometimes called plug flow. Notably, these forces near the wall serve to pull the fluid volume in the direction of the applied electric field and result in bulk fluid transport.

Electrophoretic Transport in Nanofluidics Electrophoretic transport, or electrophoresis, refers to the transport of both both positive and negative valence ionic species within the bulk (outside the EDL). Unlike electroosmosis, no bulk fluid transport occurs as the result of electrophoresis. In electrophoresis, the valence of the ionic species in solution inherently causes a separation to occur in the presence of an applied electric field. However, because both electroosmotic and electrophoretic transport mechanisms are actuated by the same externally-applied electric field, decoupling these transport effects in practice is challenging. In mathematical formality, we often describe the ion mobility under each transport according to:

$$\mu_{EO} = \frac{-\epsilon\zeta}{\eta} \tag{2.33}$$

$$\mu_{EP} = \frac{\epsilon\zeta}{\eta} \tag{2.34}$$

$$\mathbf{u} = (\mu_{EO} + \mu_{EP)})\mathbf{E} \tag{2.35}$$

where μ_{EO} is the electroosmotic mobility, μ_{EP} is the electrophoretic mobility, and ζ is the zeta potential or electrokinetic potential for each ionic specie. The zeta potential is unique to each ionic component in solution and is used to describe the phenomenological difference (its typically derived empirically) for each type of transport. In a theoretical case where the EDL is thin compared to the fluid bulk (microfluidics) and the fluid and wall-boundary properties are perfectly uniform, $\zeta = \phi_{wall}$ for the electroomostic mobility. However, this approximation is poor in nanofluidic components where the EDL thickness is significant. Commonly used microfluidic and nanofluidic materials, such as glass or PDMS, have a negative fixed surface charge that cause accumulation or ion crowding of positive ions within the EDL. This causes a preferred direction for transport of the fluid bulk, under electroosmosis, and valence-dependent (often bidirectional) ionic migration, under electrophoresis. Therefore, as one can imagine, these effects must be balanced to achieve the desired transport mode and direction. Furthermore, the experimenter's selection of ionic species is critical - it determines dominate transport mechanism (electrophoretic and electroosmotic) of charged molecules (DNA, proteins) based upon their net effective charge in that solution.

Theoretical Insights to Guide Experimental Practice From these theoretical derivations, we can now appreciate the uniform analysis time and actuation simplicity typical of plug flow in microfluidic systems. Actuation can be achieved by simply placing electrodes into each of two fluidic ports on a device and applying

a voltage. However, the charge-dependent propagation of molecules can be undesirable if the electrostatic properties of the sample are unknown or the analyte is polyvalent. It can be challenging to balance the electroosmotic and electrophoretic contributions that achieve the overall desired molecule transport, especially as device dimensions approach that of the EDL thickness. Fortunately, electroosmotic behaviors can be minimized using polymer surfactants or surface coatings that modulate either the effective viscosity or screen the surface charge at the device walls. Interestingly, these methods of engineering the slip-plane are also used for modulating the solution viscosity or the viscous sheer at high Reynold's numbers and have application to increasing the flow in large pipelines, etc.

In contrast, we should not forget that Poiseuille flow offers molecule transport within the fluid body that is independent of the sample molecules' charge. This attribute is particularly appealing in studies where molecules are nearly charge-neutral or the interrogation of all molecules, regardless of valence, is required. Applying pressure to microfluidic components is considerably more involved than voltage-actuated flow. A complex, off-chip network of valves, fixtures, and pumps are often necessary to actuate pressure driven flows. And while considerable progress has been made to integrate these components on-chip [30] or to use sheath-flows to constrict the effective profile of a fluidic channel, the physics of device scaling ultimately prevent pressure flow from accessing the nanofluidic device scale.

2.2.3 Signals Processing for Single Molecule Detection

Random Signals in Photon Counting The detection of signals from single molecule fluorescence is rooted in random processes. In this section, I will present a mathematical framework for detecting these random signals to perform single

molecule detection. For readers deeply interested in the theoretical basis for SMD, I recommend [21, 31, 32]. We begin with the simplest statement of a continuous-time signal:

$$x(t) = s(t) + n(t) \tag{2.36}$$

where $s(t)$ represents the signal information and $n(t)$ the noise. The information in $s(t)$ is produced by a discrete random process, photons of light emitted from a fluorescent dye undergoing radiative decay. This spontaneous, radiative decay process occurs as the result of an transition between at least two energy states in an atomic system - namely a ground state and an excited state. The photophysical process of fluorescence typically involves a three-state atomic system with a non-radiative triplet-state.

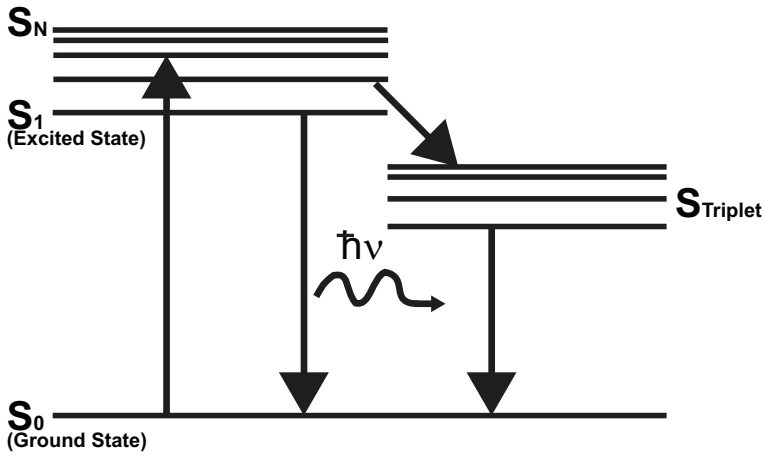

Figure 2.2: Jablonski state diagram illustrating the photophysical process of fluorescence. Fluorescence $\hbar\nu$ is emitted from the transition between excited singlet state S_1 and the ground state S_0. Non-radiative decay occurs between $S_{Triplet}$ and S_0.

However, our mathematical model need only consider the binary outcome - either producing a photon event, or not. Accordingly, we choose a Markov Process

because it is both random and memoryless (i.e. its current state is unaffected by prior state) and its probability densities sum to 1.

$$P_d + P_p = 1 \tag{2.37}$$

Where Pp is the probability of a photon emission event and P_d is the probability of a dark, or no photon, event. To accumulate the probability distribution, we consider n trials of the process, wherein each trial can produce k discrete photon events. This can be written as a series expansion (thanks to Kylan Szeto for reminding me of this expansion):

$$(P_d + P_p)^n = \sum_{k=0}^{n} n! \frac{P_p^k}{k!} \frac{P_d^{n-k}}{(n-k)!} \tag{2.38}$$

So now we can consider the expectation value of $\lambda = nP_p$ following n trials of the process, which allows us to rewrite 2.38.

$$P(\lambda, k) = n!(\frac{(\frac{\lambda}{n})^k}{k!}) \frac{(1-\frac{\lambda}{n})^{n-k}}{n-k!} = \left[\frac{n!}{(n-k)!n^k}\right] \left[\frac{\lambda^k}{k!}(1-\frac{\lambda}{n})^n\right] \tag{2.39}$$

Finally, by assessing the limit of 2.39 as:

$$\lim_{n\to\infty} \left[\frac{n!}{(n-k)!n^k}\right] \left[\frac{\lambda^k}{k!}(1-\frac{\lambda}{n})^n\right] = [1] \left[\frac{\lambda^k}{k!}e^{-\lambda}\right] \tag{2.40}$$

We conclude that the Poisson probability distribution 2.41, is the appropriate description for the discrete random process of radiative decay.

$$P(\lambda, k) = \frac{\lambda^k}{k!}e^{-\lambda} \tag{2.41}$$

Where λ is the expectation value, or mean, of the distribution and k is the number of photon events observed for each trial n. Though the number of trials n no longer appears in our Poisson PDF, it will be a useful quantity to consider later as we translate our description of $x(t)$ into a discrete form.

Random Noise in Photon Counting The noise $n(t)$ in our photon counting system is more difficult to quantify because each of the components has an associated noise specific to the application.

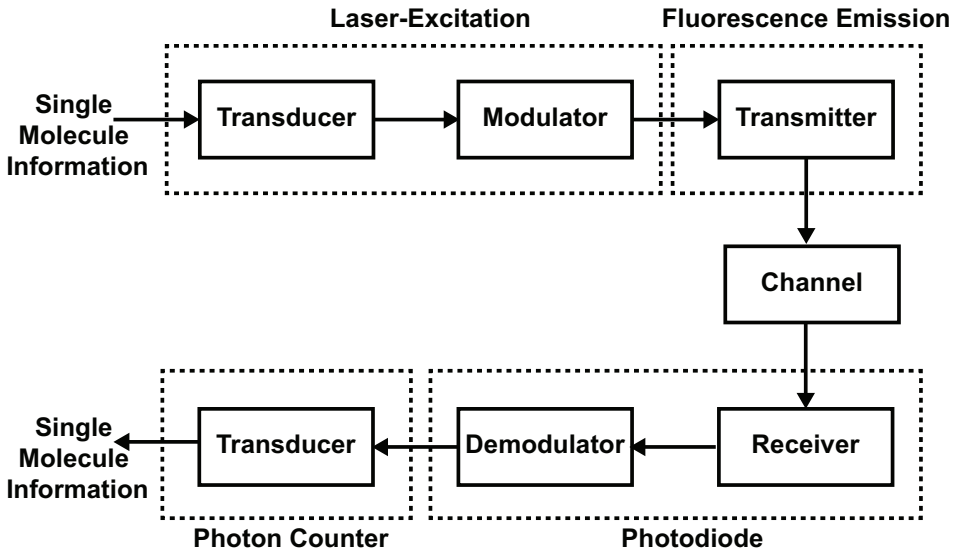

Figure 2.3: Communication system block diagram for single molecule fluorescence detection

In our application, the laser excitation serves to transduce the presence of the molecule (laser modulation is not required, but can be used) and the fluorescence emitted by the dye molecule encodes all information (as both color and number of photons) about each molecule in a format that is ready to propagate through the channel. Our channel is the combination of all optical elements used to direct photons to the receiver, typically a combination of lenses or optical fibers. In the channel, the possible sources of noise include thermal, absorption losses at

impurities leading to spontaneous emission, and non-linear effects (scattering,self-modulation). In our application, the fluorescence intensities and absorption losses during transmission through the channel are extremely low, making non-linear effects and impurity emission negligible. The power spectral density of thermal noise in the communications channel is also negligible and is given by:

$$S_n(f) = \frac{\hbar f}{2(e^{\frac{\hbar f}{kT}} - 1)} \tag{2.42}$$

where $S_n(f)$ is the power spectral density of the noise, $\hbar = 6.6 \times 10^{-34} \frac{J}{s}$ is the Planck constant, $k = 1.38 \times 10^{-23} \frac{J}{K}$ is the Boltzmann constant, T is the temperature in Kelvin, and f is the frequency of the noise. As an example, green-colored fluorescence with a wavelength of 500nm, or equivalently, $f = 9.55 \times 10^{13} Hz$, has a thermal noise power that is -125 dB relative to $\frac{kT}{2}$!!! This is why a optical channels, like an optical fiber, represent the state of the art in low-noise communication channels.

The primary source of noise during photon counting arise from the receiver, a photodiode, which can incorporate flicker, Shot, and Johnson noise. Flicker noise, or $\frac{1}{f}$ noise, is attributed to interface defect states that create electron or hole trapping centers with long (ms) lifetimes. While this noise source caused the characteristic 'popping' in radio broadcasts 40 years ago, it is negligible in modern semiconductor materials. Shot noise is attributed to generation-recombination events within the semiconductor, which are thermally-excited according to Poisson random process. Shot noise is the source of the dark current of a photodetector. Johnson noise, however, is spectrally constant and is determined by the DC resistance of the photoconductor. Therefore, Shot and Johnson noise are the primary noise sources for photodetectors.

However, for photodiodes or phototubes with gain, namely avalanche pho-

todiodes (APD) or photomultiplier tubes (PMT), the amplification by electron multiplication introduces noise. In APDs, the electron multiplication process is achieved by impact ionization, occurring within a diode that is reverse biased near the breakdown voltage. A rigorous mathematical treatment of the noise in APDs from impact ionization is derived elsewhere [33–35].

Random Signals Processing by Sampling So far, we have discussed the photon count $x(t)$ as a random signal in continuous time. We wish to record the signal for further analysis, using the process of sampling it at regularly-spaced, discrete time intervals ΔT. Interestingly, for a system whose signal is governed by random processes and is linear time invariant, each of the n discrete time intervals is equivalent to n trials of a Markov process used to compose the Poisson PDF. Therefore, the sampled signal $x(n\Delta T)$ is equivalent to the continuous-time signal $x(t)$, and as the time support of n sampling intervals increases toward infinity, we achieve a better estimation of the expectation value λ for the underlying Poisson PDF. However, this assumes an infinitely small sampling interval, described a Dirac delta function, for ΔT. In practical systems, such oversampling is unnecessary and would require infinite spectral support (a band-unlimited signal):

$$\frac{1}{\sqrt{2\pi}} \int_{-\infty}^{\infty} [\delta(t)] e^{-j\omega t} dt \Leftrightarrow \frac{1}{\sqrt{2\pi}} \int_{-\infty}^{\infty} [1] e^{j\omega t} d\omega \tag{2.43}$$

where $\delta(t)$ is the Dirac delta function, 1 is a uniform magnitude power spectrum across the frequency range ω.

To operate using bandwidth-limited systems, we use the Nyquist-Shannon sampling theorem, which states that a bandlimited signal can be sampled and perfectly reconstructed if the bandwidth of the sampling frequency is twice that of the band-limited signal. The following is a reproduction of the derivation presented in

Shannon's original work [36]:

$$f(t) = \frac{1}{2\pi}\int_{-\infty}^{\infty} F(\omega)e^{j\omega t}d\omega \tag{2.44}$$

$$f(t) = \frac{1}{2\pi}\int_{-2\pi W}^{2\pi W} F(\omega)e^{j\omega t}d\omega \tag{2.45}$$

$$t = \frac{n}{2W} \tag{2.46}$$

$$f(\frac{n}{2W}) = \frac{1}{2\pi}\int_{-2\pi W}^{2\pi W} F(\omega)e^{j\omega \frac{n}{2W}}d\omega \tag{2.47}$$

where W is the one-sided bandwidth of the signal. This can also be seen intuitively from a graphical representation of a bandlimited signal, wherein its spectral content extends from -W to +W by properties of Hermitian symmetry. Shannon's work also reminds the reader that signal reconstruction can be performed using a rectangular window function:

$$\frac{1}{\sqrt{2\pi a^2}} \cdot rect\frac{\omega}{2\pi a} \Leftrightarrow sinc(at) \tag{2.48}$$

where $rect(\omega)$ is rectangular window function in the frequency domain, $sinc(t)$ is the normalized cardinal sine function, and a an arbitrary scaling factor. Notably, the signal sampling must be performed according to the Nyquist condition to avoid aliasing during signal reconstruction. The process of sampling in the time domain causes periodicity of the sampled spectrum within the frequency domain, as described by the Poisson summation formula using a Fourier series summation:

$$\sum_{k=-\infty}^{\infty} X(\omega - k\omega_s) \Leftrightarrow \sum_{n=-\infty}^{\infty} \underbrace{\Delta T \cdot x(n\Delta T)}_{x[n]}\ e^{-j\omega n\Delta T} \tag{2.49}$$

where k is the integer Fourier series element for the k^{th} copy of the sampled signal's power spectrum. If the sampling frequency ω_s does not meet or exceed the

Nyquist criteria, than there will be spectral overlap between adjacent copies of the signal's power spectrum, leading to aliasing cross-talk that cannot be distinguished.

The consequence of the Nyquist-Shannon sampling theorem is extremely important for our photon counting signals analysis. First, the theorem determines the necessary sampling rate for discretization of a continuous time signal. In our case, the maximum sampling rate is determined by the radiative lifetime of fluorescence processes, typically around 2-10 ns. Therefore, sampling with a time interval (ΔT) of 1 ns, or with a frequency of 1 GHz, will properly record the individual photon events (assuming a detector with similar bandwidth). Sampling with a time interval of 50 μs, or 20 kHz, greatly reduces the data storage requirements, but at the cost of signal information loss between 20 kHz-1 GHz. However, since our goal is to study molecule transport across the laser illuminating a fluidic device, a transit duration typically 250 μs or longer, a 50 μs sampling interval is adequate to capture and reconstruct the signal. Second, the theorem subtly introduces windowing functions to reconstruct the sampled signal. For a perfectly bandlimited signal, Shannon applied a rectangular window, however this window causes considerable aliasing. Improved windowing functions for signal reconstruction will be discussed as matched filters for optimum signal reconstruction.

Single Molecule Detection (SMD) To identify molecules within our time resolved photon record, we apply the statistical properties of a single-variable Poisson process to separate noise from signal using the following relationships:

$$\lambda = E[x[N]] =< x(n\Delta T) > \tag{2.50}$$

$$\sigma^2 = \lambda = E[x[N]^2] - E[x[N]]^2 \tag{2.51}$$

$$\sigma = \sqrt{\lambda} \tag{2.52}$$

where λ is the mean, σ^2 is the variance, and σ is the standard deviation of the sampled signal $x[N]$, or equivalently $x(n\Delta T)$. These values can be extracted by a simple calculation of the mean or standard deviation for all values in a given photon record or by plotting a photon count histogram (PCH) and fitting to a Poisson PDF. The minor problem with the later option being that the fit quality will degrade if the data contains bright, fluorescent molecules that introduce another variable to the Poisson process. Using these Poisson PDF parameters, we establish a threshold condition to identify single molecule detection events:

$$Threshold_{SMD} = \begin{cases} Molecule & \text{if } y(n\Delta T) > \lambda + a\sigma \\ No\ Molecule & \text{if } y(n\Delta T) <= \lambda + a\sigma \end{cases} \tag{2.53}$$

where a is a user-defined quantity to adjust the threshold stringency to prevent random noise events from being identified as individual molecules. To emphasize the statistical stringency often imposed in these experiments, consider a Poisson-distributed noise with $\lambda = 0.5$. If we observe an event with intensity $\lambda + 5\sigma$, equivalent to an $SNR = 5$, the probability of this event occurring due to random noise fluctuations is 1.7×10^{-4} based upon the Poisson cumulative distribution function (CDF). In many experiments the SNR is between 10-200, making negligible the probability of random noise fluctuations appearing as SMD events.

Detection by Auto-Correlation and Cross-Correlation Fluctuation correlation spectroscopy, later and more popularly named Fluorescence Correlation Spectroscopy (FCS) [37–39]. Based upon the autocorrelation function, we can study the fluorescence fluctuations of a dye-labeled biomolecule - deducing such parameters as its triplet state lifetime, drift transport, and diffusive transport through mathematical fitting - making this a powerful method for studying photo-

physical phenomena and the characteristic signal-to-noise ratio (SNR) of a detection system. Considerable scientific effort has focused on developing the analytical forms for correlation functions that apply to the boundary conditions of various experimental geometries, including but not limited to, free-solution, confinement in 1-D and 2-D nanostructures, cell membranes, and so forth. Frankly, while these are interesting and useful conditions for many biophysical studies, my experience with has taught several valuable lessons as it applies to FCS for single molecule studies in nanofluidics: first, the inherent ensemble averaging of FCS can be easily skewed by a few outlying events that completely destroy correlation function fitting to a tractable mathematical model; second, while I have practiced deriving such mathematical models, it is a painstaking endeavor that I wish not to repeat; third, FCS is most useful as a tool operated in complement to single molecule detection.

To further detail of the third point, the autocorrelation function in FCS provides useful qualitative information regarding the photophysical dynamics of a single molecule fluorescence measurement. At zero time lag, $\tau = 0$, the fluorescently-labeled molecule enters an inspection volume and begins to emit fluorescence. The amplitude of $G(\tau = 0)$ is proportional to the average number of molecules within the inspection volume. During the molecule's lifetime within the inspection volume (i.e. until $G(\tau) = 0$, we can observe the triplet state formation and dominant transport regimes. The correlation function also provides a useful tool for signal analysis. Normally, random wide sense stationary processes are not-square integrable and cannot be analyzed using Fourier transform methods. However, through a calculation of the expectation value of random signal, the autocorrelation function, the result can be analyzed with a Fourier transform using the Wiener-Khinchin theorem.

$$G_{xx}(\tau) =< x(t)x^*(t-\tau) > \tag{2.54}$$

$$G_{xy}(\tau) =< x(t)y^*(t-\tau) > \tag{2.55}$$

$$S(\omega) = \frac{1}{\sqrt{2\pi}} \int_{-\infty}^{\infty} G(\tau) e^{-j\omega\tau} d\tau \tag{2.56}$$

where G_{xx} is the autocorrelation and G_{xy} is the cross-correlation of the continuous-time signals, and $S(f)$ is the power spectrum following the Fourier transform. Using the Weiner-Khinchin relationship, we estimate the signal's average power spectral density, which can be used to design noise-reducing filters. It also provides a reminder of useful transform relationships for the purpose of calculating the auto-correlation and cross-correlation. We can now chain together several Fourier transform pairs to equate the convolution of two signals to their expectation value:

$$\frac{1}{\sqrt{2\pi}} \int_{-\infty}^{\infty} [x_1(t) * x_2(t)] e^{-j\omega t} dt \Leftrightarrow \frac{1}{\sqrt{2\pi}} \int_{-\infty}^{\infty} [x_1(\omega) x_2(\omega)] e^{j\omega t} d\omega \tag{2.57}$$

$$\frac{1}{\sqrt{2\pi}} \int_{-\infty}^{\infty} [x_1(\omega) x_2(\omega)] e^{j\omega t} d\omega \Leftrightarrow \frac{1}{\sqrt{2\pi}} \int_{-\infty}^{\infty} [G_{12}(\tau)] e^{-j\omega\tau} d\tau \tag{2.58}$$

$$x_1(t) * x_2(t) = G_{12}(\tau) \tag{2.59}$$

where $x_1(t)$ and $x_2(t)$ are independent signals and $G_{12}(\tau)$ is their cross-correlation. While this is a long-method to relate time-convolution to correlation, it has helped me arrive upon a method to numerically evaluate cross-correlation, which preserves the exact molecule count during computation of correlated detection events.

Correlation in Single Particle Measurements To perform direct, time-correlated detection and quantification of single molecules we combine both Poisson statistics and some concepts originating in particle counting for nuclear physics. The process of correlated detection of a single event can be considered geometrically, by a process of self-windowing. In this process, the characteristic time of a single molecule

detection event defines the bounds or window of time to examine correlated detection with other signals. While this method is conceptually simple, it suffers from several shortcomings. First, the correlation is conditional and therefore biased to the signal defining the window. Second, a geometric inspection illustrates that this method could allow correlation of a molecule within the laser inspection volume with one immediately outside.

Instead, let's return to the mathematical formulation for convolution, where we consider two independent signals $f(t)$ and $g(t)$. This convolution can be evaluated numerically as:

$$f(t) * g(t) = \int_{-\infty}^{\infty} f^*(\tau)\ g(t+\tau) d\tau \tag{2.60}$$

$$f[n] * g[n] = \sum_{m=-\infty}^{\infty} f^*[m]\ g[n+m] d\tau \tag{2.61}$$

Notably, I have found that a slightly reduced representation of the sampled signals $f[n]$ and $g[n]$, wherein the allowed value are either 1 or 0 to represent the centroid of a SMD event, offers a powerful way to evaluate the correlation while conveniently maintaining a record of the exact number of molecules involved in the correlation. Using a convolution over a window of time samples $6\sigma(\Delta T)$ in length, we can evaluate both the time-correlated coincidence within the Gaussian beam of charcteristic widht $2\sigma(\Delta T)$ and also measure directly the probability of randomly correlated detection events. To illustrate this correlation, I implemented a time coincidence histogram (TCH) that will be used further in the work.

2.3 Experimental Details

2.3.1 Sample Preparation

HeLa Cell Chromatin Extraction HeLa cells constitutively expressing green fluorescent protein on histone H2B (H2B-GFP) were provided by Geoffrey M. Wahl at The Salk Institute for Biological Studies, USA. Cell cultures were cultured as monolayers in Dulbecco's modified Eagle's medium (DMEM) supplemented with 5% fetal calf serum. Native chromatin fragments were prepared from HeLa cells as described [40]. Briefly, cells from two 15 cm plates were scraped and washed once with 1xRSB (10 mM Tris pH 7.6, 15 mM NaCl, 1.5 mM $MgCl_2$), resuspended in 5 mL 1xRSB buffer with 1% Triton-X 100 and homogenized using a Dounce homogenizer fitted with a loose pestle using eight strokes. Nuclei were recovered by centrifugation, resuspended in 1.5 ml Buffer A (15 mM Tris pH 7.6, 15 mM NaCl, 60 mM KCl, 0.34 M Sucrose, 0.5 mM Spermidine, 0.15 mM Spermine, 0.25 mM PMSF and 0.1% -mercaptoethanol), to which we added 15 μL 0.1 M $CaCl_2$ and 1.5 μL of micrococcal nuclease (MNase) at a concentration of 3 units/μL and incubated for various times, using 5 μL of 0.5 M EDTA to stop the digestion. Digests were centrifuged, the supernatants discarded, and each 140 μL aliquot of nuclei were resuspended in 450 μL 10 mM EDTA, 50 μL 5 M NaCl to solubilize the chromatin. Soluble chromatin was separated from the insoluble debris by centrifugation. For gel analysis of DNA, we took 60 μL of chromatin, added 24 μL H_2O, 6 μL 10% SDS and 24 μL 5 M NaCl, then extracted DNA with a 1:1 mixture of phenol-chloroform and 10 μL supernatant was analyzed by 1.5% agarose gel electrophoresis, as shown in Figure 2.4 and 2.5. Batch-to-batch variations in preparation are attributed to MNase activity. We used a fluorimeter to measure the fluorescence of the intact chromatin and a spectrophotometer to measure the

amount of DNA extracted from the chromatin. This served to calibrate the fluorimeter reading, allowing direct estimation of the sample concentration during subsequent chromatin isolation preparations without removing histones. The calibration was reproducible between preparations.

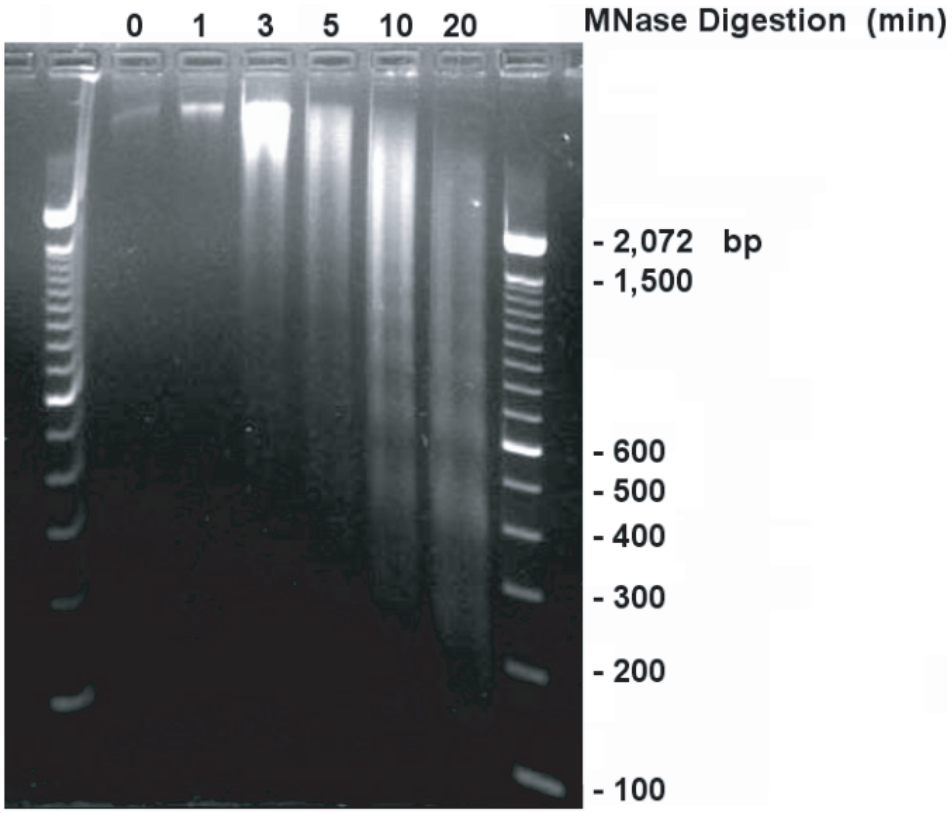

Figure 2.4: Chromatin DNA Fragment Sizing by Gel Electrophoresis. Chromatin was extracted from HeLa nuclei using MNase, resulting in decreased chromatin fragment sizes. Histone proteins were removed by Protenase K digestion to allow DNA sizing. The 5 min digestion yielded fragment lengths above the 2,072 bp marker.

Lambda DNA Growth and In-Vitro Methylation Lambda DNA from phage was grown in a methylation deficient host (Promega D1521), digested with *HindIII*, and methylated in vitro with *SssI* methylatranserase, which can methylate all 3,113 CpGs in the 48.5 kbp genome. Efficacy of the methylation reaction

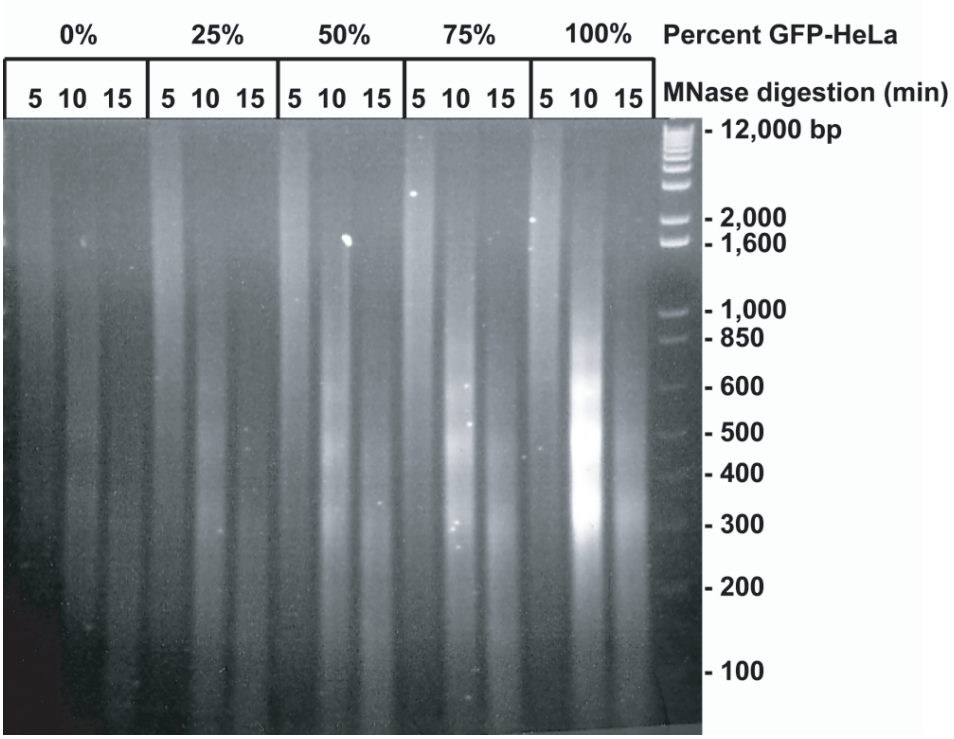

Figure 2.5: Chromatin Dilutions for Varied MNase Treatments. GFP-HeLa and wild-type chromatin were MNase digested for 5, 15, and 30 minutes. Digestions from this preparation illustrated a more disperse range of fragments, nominally centered between 1-2 kbp.

was assessed by resistance to digestion by the methylation sensitive enzyme *HpaII* as shown in Figure 2.6.

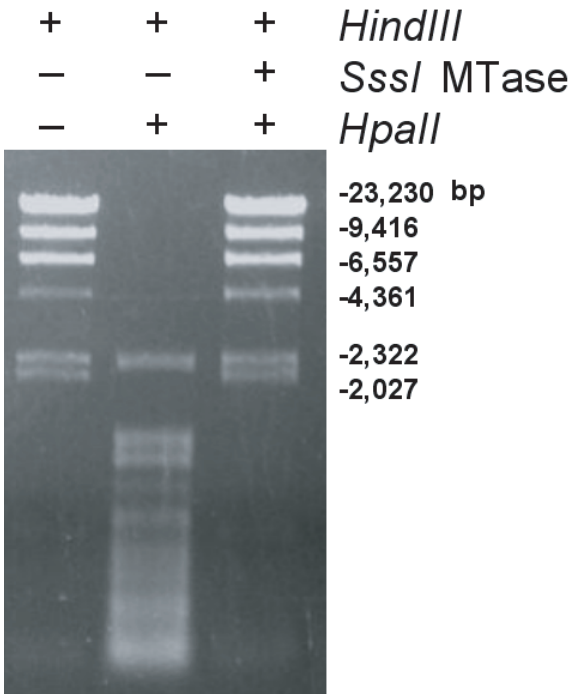

Figure 2.6: In-Vitro DNA Methylation Test with *HpaII*. Lambda DNA was left unmethylated or methylated in vitro with *SssI* methylatranserase. Aliquots of DNAs were then digested with *HindIII* or with both *HindIII* and *HpaII*. Resistance to digestion by HpaII is evidence for DNA methylation. Base pair sizes of *HindIII* fragments are shown.

Methyl Binding Domain Protein Synthesis and Labeling The methylation sensitive binding domain (MBD) from MBD1 was cloned into the pET-30b plasmid for *E.coli* bacterial expression of 1xMBD (pET-1xMBD) using material provided by Adrian P. Bird at The Wellcome Trust Centre for Cell Biology, University of Edinburgh, UK. IPTG induced E.coli were lysed and the recombinant His6-tagged MBD1 was purified from 100 mL induced BL21(DE3) cultures on Ni-NTA agarose (Qiagen) using denaturation and on column renaturation cycles to refold the protein. Following purification the fusion protein was labeled with

Alexa 488 using Invitrogen's microscale labeling kit (A30006), which labels free amines. Three additional rounds of resin purification were preformed to better purify away free labels. The integrity of the labeled MBD probe was assayed with a slot-southwestern blot in Figure 2.7. Though absorbance measurements indicated an average degree of labeling of 1.5 dye per MBD, we believe that three sub-populations remained within the labeled mixture: dye-labeled MBD, free unbound dye, and MBD with no dye. If three subpopulations exist within the dye-labeled MBD solution, the number of bound MBD-DNA complexes would be under-reported.

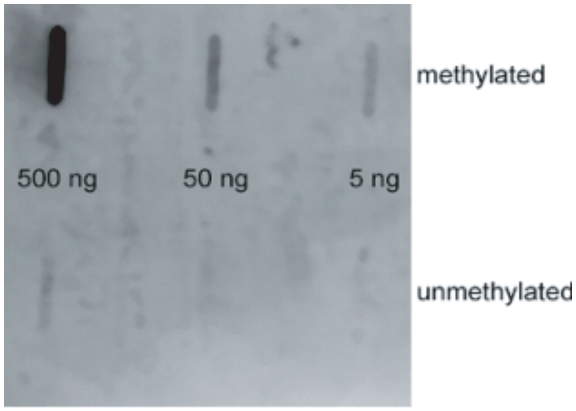

Figure 2.7: Southwestern Blot Analysis of MBD-1 Activity and Methylation Specificity. Both unmethylated and in-vitro methylated lambda DNA were bound to a nitrocellulose membrane in varying quantities using a slot blotting apparatus. The Alexa 488 labeled MBD1 protein was then used to probe the entire blot. Following over night incubation at 4 °C the blot was washed and scanned with Typhoon imager to detect the Alexa Fluor 488 label. This image demonstrates that the MBD1 probe binds to methylated DNA with high specificity.

MBD-DNA Affinity Reaction In a mixture of methylated and unmethylated DNA suspended at 50 ng/μL in 1x Tris Buffered Saline (1x TBS, 50mM Tris-HCl and 138mM NaCl and 2.7mM KCl, pH 8.0), we performed DNA staining using

TOTO-3. Approximately 1 μg of labeled DNA was then diluted into 20 μL of buffer containing 1x TBS with 2% bovine serum albumin and 0.1% TritonX-100 (v/v). A volume of 1 μL MBD1, stored at 280 ng/L, and labeled with AlexaFluor488 was then added to the DNA to perform the binding reaction under conditions of molar excess. The binding reaction occurred for 2 hours at room temperature.

DNA Labeling We use the cell-impermeant intercalator TOTO-3 (Invitrogen). The labeling reaction was conducted by mixing the diluted DNA or chromatin and the diluted dye according to the method described by the manufacturer. All samples were prepared with a 1:5 dye to base pair ratio, unless otherwise noted. Following the labeling reaction, samples were protected from light and stored overnight at 4 °C. TOTO-3 exhibits significant fluorescence enhancement upon binding, which alleviated the need for purification to remove unbound dye following the labeling reaction.

2.3.2 Device Fabrication and Operation

Fabrication of Nanofluidic Channels Nanofluidic channels were fabricated in a fused silica substrate. Projection photolithography (GCA Autostep 200) was used to pattern fluidic channels with a 500 nm critical dimension. This method allowed rapid patterning of 27 fluidic channel arrays, totaling 432 fluidic channels, on a 100 mm diameter wafer. Patterns formed in the developed photoresist were transferred approximately 250 nm into the silica using reactive ion etching (Oxford 80, Oxford Instruments). The fluidic channels were protected with photoresist during subsequent through-wafer drilling using a focused jet of alumina abrasive to form the access ports at the ends of the channels. The wafer surface was cleaned with a hot Piranha solution (3 H_2SO_4: 1 H_2O_2) and RCA standard clean

(5 H_2O : 1 NH_4OH : 1 H_2O_2, heated to 70 °C). Direct touch bonding with a 170 μm thick coverslip wafer was performed to cap the fluidic channel. A subsequent high-temperature anneal to 1050 °C permanently bonded the stack of fused silica wafers together. An optical-grade epoxy (Norland Products) was used to attach fluid reservoirs to the wafer surface.

Electrokinetic Flow in Nanofluidics Samples were kept in their respective storage buffer until DNA labeling and/or MBD binding reactions. Following these reactions, samples were serially diluted in 1x Tris-Borate-EDTA (1x TBE, 89 mM TRIS borate and 2mM EDTA, pH 8.0), with additives 0.5% polyvinylpyrrilodone (PVP) measured (w/v) and 0.1% TritonX-100 measured (v/v) (both from Sigma Aldrich, St. Louis, MO). The final dilution suspended the samples at an estimated concentration of 600 pM, nominally 1-2 ng/μL for chromatin samples, and about 0.25 ng/μL for methylated DNA samples. The polymer additives in the buffer served to limit electroosmotic flow and prevent non-specific interactions with the fluidic channel walls without denaturing proteins. We loaded 50 μL of the sample solution into the input reservoir of a fluidic channel array and then connected to the negative electrode. The output reservoir contained only the buffer solution and was connected to the positive electrode. Samples were flowed at an applied bias of 50 V for all chromatin samples and 100 V for all methylated DNA samples. Stable electrokinetic flow was established during a pre-flow time of 20 min to ensure steady-state flow conditions had been achieved prior to data collection. Each sample was examined for a total of 15 min, always using the same fluidic channel within the array. Following single molecule detection, the fluidic channel array was rinsed iteratively for a total of 30 min and then checked to verify the absence of fluorescently-labeled molecules, prior to loading the next sample. Fluid channel arrays used with chromatin experiments were not reused with DNA methylation

experiments.

2.3.3 Optical Measurement Setup

Laser Induced Fluorescence Confocal Microscopy Single molecule fluorescence was observed using an inverted microscope (IX-71, Olympus) equipped with a side laser port. Laser illumination of 330 μW at 488 nm (Sapphire, Coherent) and 1300 μW at 635 nm (Cube, Coherent) were overlapped in free-space, incident on a dual-band dichroic mirror (488/647rpc, Chroma Technology) and then focused onto the nanofluidic channel using a 60x, 1.2 numerical aperture water-immersion objective (UPlanSAPO, Olympus), and aided with an electron multiplied CCD camera (Cascade 512B, Photometrics). A dual-band laser notch filter (NF01-488/647, Semrock) attenuated stray laser light and passed single molecule fluorescence. Confocal spatial filtering occurred using a 50 μm diameter pin-hole (901PH, Newport). Two color fluorescence was then chromatically split using a second dichroic mirror (FF560-Di01, Semrock) and then filtered by bandpass fluorescence filters (525/50M and 680/40M, Chroma). Each color of fluorescence was then collected using a 100 μm diameter core multimode optical fiber (OZ Optics). Photons were detected by avalanche photodiodes (APD) in single photon counting mode (SPCM, Perkin-Elmer) and recorded at 100 kHz using a high-speed correlator (correlator.com) and a personal computer.

2.3.4 Analysis Method

Statistical Analysis Propagated error analysis was performed to evaluate the proportion of bound molecules, chromatin or MBD-DNA, with respect to total DNA. First, we define a window region that encompasses the full width of the Gaussian distribution in a time coincidence histogram. Adjacent to the window

region are the sidebands, which were used to characterize the background of uncorrelated molecules. The background contribution in the window region was calculated based upon the uncorrelated molecules per 50 μs bin in the sidebands, reported as the mean and standard deviation, and then scaled by the number of bins within the window region. The total molecules counted within the window region was summed and reported with a Poisson counting error. The number of bound molecules was then calculated by subtracting the total molecules from the background molecules within the window region and propagating the error. Second, the number of total DNA molecules observed was counted and reported with a Poisson counting error. The ratio of bound molecules and total DNA molecules was then calculated and the errors of each were propagated. As applicable, we plot the average value and error bars that represent the propagated error.

Fitting error analysis was performed to measure the concentration of molecules measured within a nanofluidic channel. The inter-event time separation was plotted as a histogram and then fitted to single-term exponential decay using Matlab's built-in fitting routine. The fitted mean inter-event time was calculated with a 95% confidence interval. The mean and confidence interval were then evaluated using a Poisson model, to describe molecule occupancy within the inspection volume, to report concentration values.

2.4 Results and Discussion

2.4.1 A Nanofluidic Platform for Single Molecule Analysis

Our strategy for high throughput analysis of single molecules of methylated DNA and chromatin entailed time-resolved detection and spectral identification of fluorescent labels bound to individual molecules containing epigenetic marks of inter-

est. We flowed and detected DNA and chromatin in a solution confined within a nanofluidic channel. These channels reduce the optical excitation volume for fluorescent analysis, thus enabling us to interrogate individual molecules in solutions of relatively high concentration [41]. The nanofluidic channels were fabricated in a fused silica substrate using photolithography and reactive ion etching. Figure 2.8 shows a single nanofluidic channel made by this process with cross-sectional dimensions of approximately 250 nm wide by 500 nm deep. We formed 27 separate fluidic channel arrays, each with 16 parallel channels, on a 100 mm diameter wafer [42]. Each array also had access ports with a reservoir at the ends of the channels, which we used to load the samples and to insert electrodes for controlling electrokinetic flow.

To analyze individual molecules of DNA and chromatin flowing through channels, we mounted the silica wafer on a laser confocal microscope and illuminated the samples flowing through an individual channel with two overlapping Gaussian shaped laser profiles, each with a diameter of approximately 1.3 μm as illustrated in Figure 2.9. The laser profiles were larger than the channel width, so that every fluorescent molecule was interrogated with the same illumination profile. The illuminated inspection volume within the channel was 0.16 fL. A burst of fluorescence, associated with the different labeled components, was emitted as each molecule passed through the illumination profile. The colors composing a molecule's signature were separated with optical filters and then detected with avalanche photodiode detectors. A record of the red and green fluorescence bursts were accumulated at 100 kHz onto a personal computer and then analyzed with a custom Matlab algorithm to identify single molecule detection (SMD) events [18, 43].

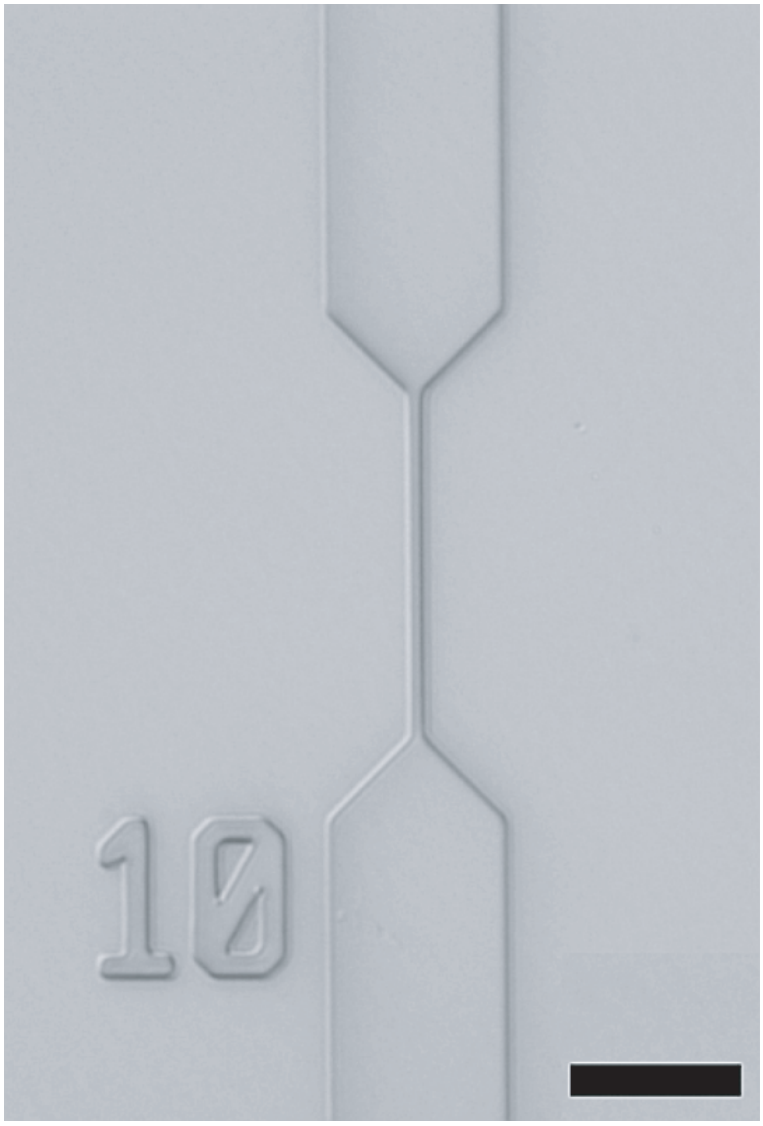

Figure 2.8: A differential interference contrast optical micrograph of a typical nanofluidic channel used in SCAN. The narrow region, with a 500 nm wide and 250 nm deep cross-section, was used during fluorescence detection. We formed 432 of these channels on a single 100 mm diameter fused silica wafer. The scale bar is 10 μm.

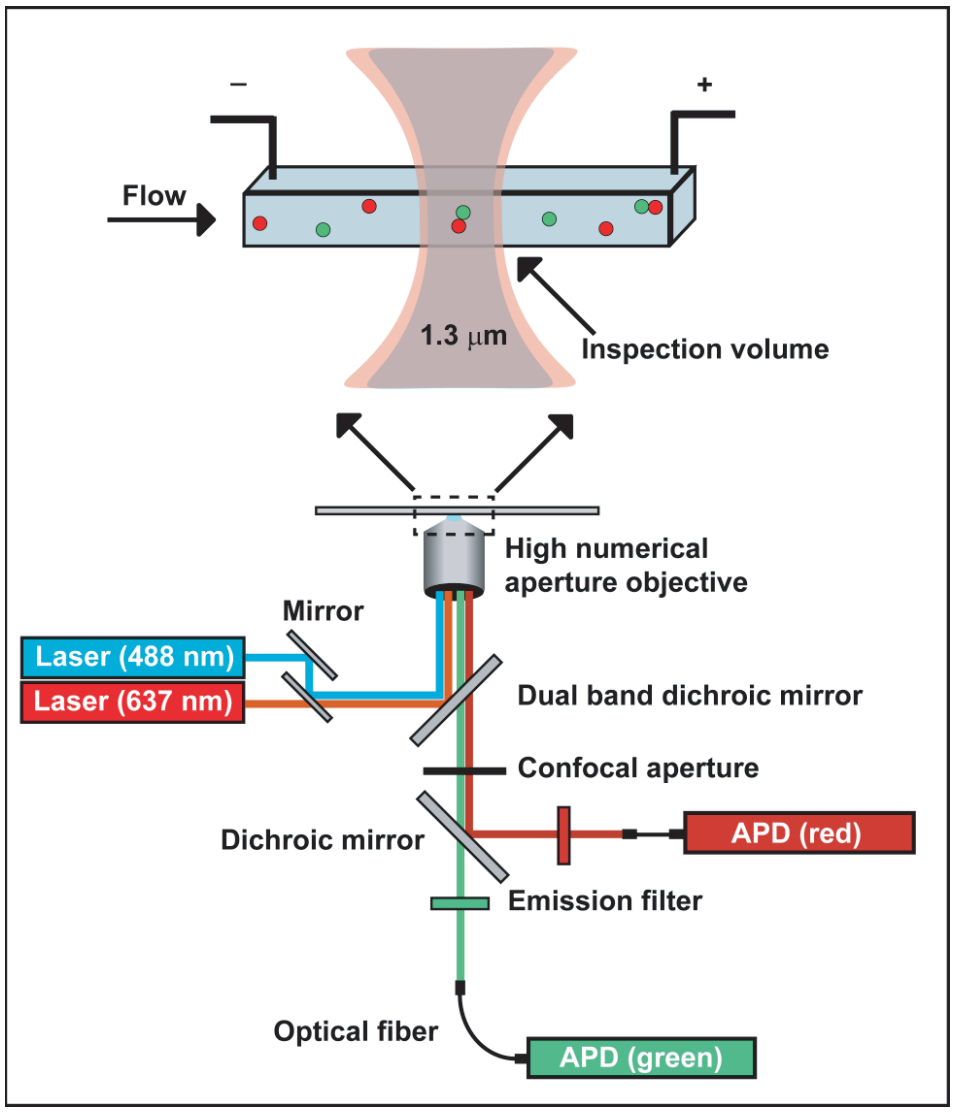

Figure 2.9: Schematic diagram of a wafer mounted on a confocal fluorescence microscope. Two overlapped lasers illuminated a 1.3 μm length of the nanofluidic channel and formed an inspection volume of 0.16 fL. Collection of the dim, fluorescent signature for each molecule was achieved using a confocal aperture, which spatially restricted the optical collection to the inspection volume, and avalanche photodiodes (APDs), which provided single photon detection.

2.4.2 Nucleosome Detection on Native Chromatin

In order for this platform to be a viable tool for epigenomic analysis, we needed to demonstrate that chromatin could be directed through the nanofluidic channel, remain intact, meaning nucleosomes remained on the DNA, and that we could detect fluorescent signatures of the histone and DNA components. For this test we used chromatin extracted from HeLa cells bearing a transgene expressing an green fluorescent protein (GFP) fusion on H2B [44]. H2B-GFP incorporated into nucleosomes allowed the chromatin to fluoresce. We prepared native chromatin from the cells using standard methods, treating isolated nuclei with micrococcal nuclease (MNase) and then extracting the soluble native chromatin using a high salt buffer. We next labeled the DNA within our chromatin preparations with TOTO-3, a red nucleic acid stain that is spectrally distinct from GFP. We wanted to analyze this dual labeled chromatin for two reasons. First, it permitted us to determine whether chromatin remained intact during nanofluidic electrokinetic flow, which is essential for any successful application of this method for epigeneomic analysis. Intact chromatin will produce time-coincident TOTO-3 and GFP fluorescent SMD events that indicate DNA and histones were bound. Second, we wanted to demonstrate that simultaneous, multi-color detection of chromatin could be performed at high rates. This is a requirement if our platform is to be used to identify multiple epigenetic marks simultaneously on intact chromatin, on a genome wide basis.

Figure 2.10 illustrates a 0.25 s SCAN using chromatin extracted after a 5 min MNase digestion and then driven through a nanofluidic channel at 50 V. The top panel shows photon bursts corresponding to TOTO-3, which marks the DNA, while the bottom panel shows GFP fluorescence that marks the H2B. In order to identify the single molecule peaks shown in Figure 2.10, successive photon arrival times differing by less than 200 μs were grouped as a burst. This time is about one-

third that required for a molecule to pass through the inspection volume. Bursts with a total of 10 or more photons were designated as SMD events. The mean noise detected with buffer only was 0.22 photon/50 μs.

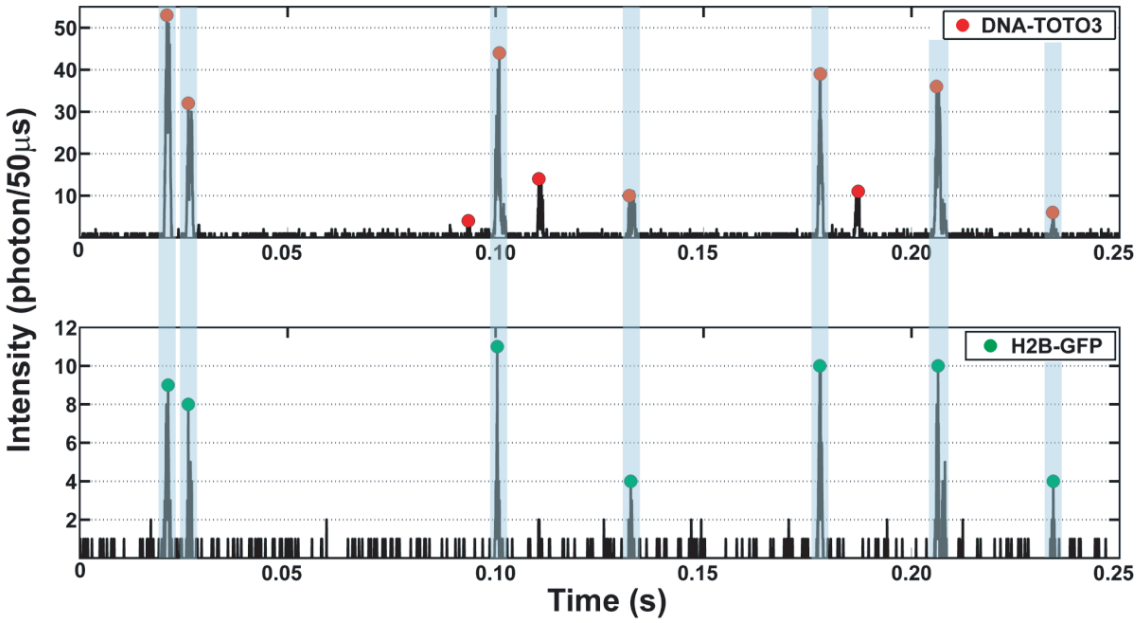

Figure 2.10: Process of Single Molecule Detection and Two-Color Coincidence Analysis. Time-trace record of photon bursts observed by each APD, showing 0.25 seconds of a 15 minute nanofluidic SCAN. A burst with a sum of 10 or more photons satisfied a threshold condition and was designated a SMD event, shown here by a red or green marker identifying DNA and histone H2B respectively. Intact chromatin fragments, highlighted in blue, were identified by time-coincident detection of both a red and green event.

The burst duration (t) for each fluorescent dye color was examined separately and then fitted with a Gaussian model with free parameters μ, for the mean burst duration, and σ, corresponding to standard deviation in the burst duration. The fitted, mean burst duration is provided on each plot with a 95% confidence interval. The Gaussian model used was:

$$\frac{e^{-\frac{(t-\mu)^2}{\sqrt{2\sigma^2}}}}{\sqrt{2\pi\sigma^2}} \tag{2.62}$$

Given the approximate laser beam diameter (x_{laser}) of 1.3 μm and the mean burst duration (t_{burst}) of 585 μs and 495 μs for the DNA and H2B molecules, respectively, we calculated a mean velocity of 2.2 mm/s and 2.6 mm/s using:

$$v = \frac{x_{laser}}{t_{burst}} \tag{2.63}$$

The results of this fitting procedure are given below in Figure 2.11

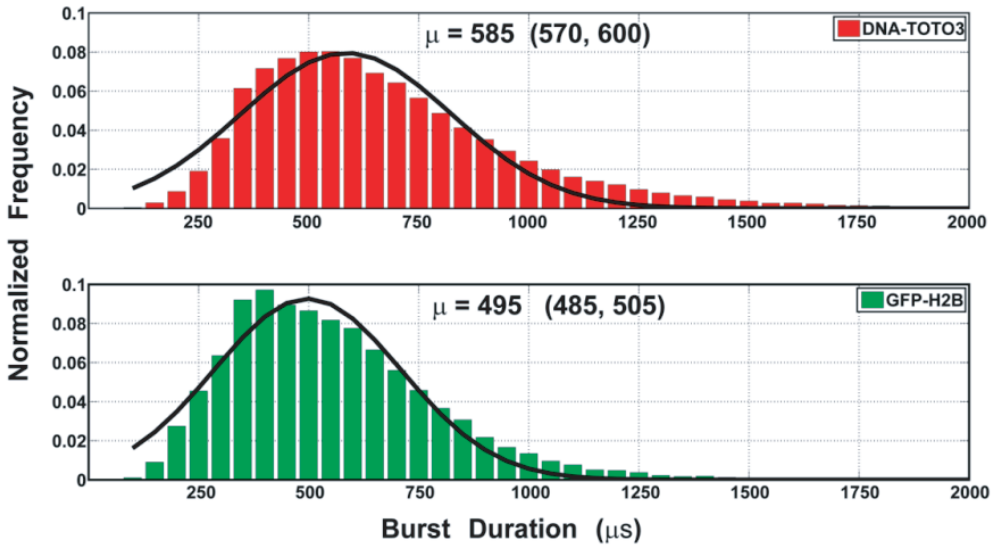

Figure 2.11: Burst Duration Analysis by Gaussian Fitting.

Since the sample solution was loaded into the reservoir connected to the negative electrode, only molecules carrying a net negative charge will be driven into the channel. In the pH 8.0 buffer used, only histone-free DNA and intact chromatin carry net negative charge. The net positive charge of individual free histones was evaluated using the amino acid sequence for each of the four histones entered into

an online calculator (http://www.scripps.edu/ cdputnam/protcalc.html). From this calculation, we estimated a positive charge of 16.5 (or greater) for each histone protein, given the pH8.0 used in this work, which indicated that free histones will remain in the loading reservoir. The time-coincident SMD events are marked by blue bars spanning the plots, the majority of which are intact chromatin. Accurate identification of dual labeled chromatin was ensured by using optical filters that achieved more than 20 dB of spectral isolation of green GFP bursts from red TOTO-3 bursts, essentially eliminating fluorescence spectrum cross-talk or bleed-through during detection.

The effect of TOTO-3 intercalation to chromatin was assessed to achieve the possible highest fluorescence intensity while not dissociating histones from the chromatin. These results are summarized in Table 2.1. We found the 1:5 dye to base pair ratio to be optimum for identification of coincident molecules bound with DNA. Since all samples in this test were examined in the same fluidic channel and the TOTO-3 labeled samples were examined first, we observed a small level of TOTO-3 adsorption to the fused silica surface of the channel. This adsorbed dye was subsequently collected by unstained chromatin and resulted in a 5.2% coincident detection rate.This further confirmed that TOTO-3 labeling did not dissociate the histones [45, 46].

Approximately, ninety-three percent of all GFP molecules identified were coincident with a DNA molecule, indicating chromatin remained intact during electrokinetic flow within our nanofluidic device. We observed that approximately one-third of the TOTO-3 signals were not coincident with GFP. This population of molecules is expected to arise from undigested and histone-free linker DNA known to exist in the genome, and also from intact chromatin that contained only the endogenous unlabeled H2B; half of the H2B in the cells is made from the GFP

Table 2.1: Chromatin observed as a bound molecules due to TOTO-3 labeling.

TOTO-3 Dye:Basepair	Bound:DNA Molecules	Bound:H2B-GFP Molecules
None	0.42 ± 0.05	0.052 ± 0.006
1:15	0.26 ± 0.05	0.83 ± 0.04
1:10	0.31 ± 0.02	0.86 ± 0.03
1:5	0.35 ± 0.01	0.94 ± 0.02

fusion transgene [44].

To further test the authenticity of chromatin detection using SCAN, we prepared chromatin from mixtures of nuclei from wild-type HeLa cells and HeLa cells with the H2B-GFP transgene, maintaining a constant total cell quantity for all mixtures. We anticipated that the rate of coincidence should drop with increasing amounts of wild-type chromatin, yielding fewer fragments with H2B-GFP. Fragments from each mixture were then detected by SCAN to determine the fraction of two-color labeled chromatin present in each mixture. We compiled a record of all coincident SMD events observed during a period of 15 min using a time coincidence histogram (TCH), shown in Figure 2.12. The TCH contains the time-offset between all identified GFP events and TOTO-3 events within a fixed time window. The area under the peak and above the background level, describes the total chromatin fragments with H2B-GFP, which increased with the proportion of GFP-HeLa nuclei. We found the proportion of chromatin fragments with H2B-GFP to exhibit a linear increase with GFP-HeLa proportion for both the 5 and 15 min digestion series, as given in Figure 2.13. The direct proportion between chromatin fragments with H2B-GFP and input of GFP-HeLa nuclei validates the authentic detection of chromatin. Note that the slopes differ for the two digestion

times with the prolonged digestion producing a smaller slope. The coincidence per DNA was principally reduced due to an increase in mononucleosome fragments and linker DNA fragments produced at longer digestion times, for a constant number of H2B-GFP nuclei within a mixture. This trend was also consistent with other chromatin preparations, wherein longer fragments demonstrated a higher coincidence proportion.

We observed variation in the size of chromatin fragments prepared during different batches of MNase digestion. For example, GFP-HeLa chromatin extracted after a 5 min MNase digestion, but prepared from different batches of GFP-HeLa cells on separate dates yielded different fragment sizes, as verified by gel electrophoresis in Figure 2.4. We attribute this to variation in MNase activity. As a result, nanofluidic SCAN detected a 93% coincidence per GFP for samples with a median fragment size above 2 kbp (5 min lane in Figure 2.4); while 50% coincidence per GFP was observed for samples with a median fragment size less than 2 kbp (100% GFP, 5 min lane in Figure 2.5). To eliminate the possibility of systematic variation in the optical setup and/or nanofluidics, we later repeated these SCANs and obtained the same results. Further SCAN with chromatin digested to less than 1 kbp fragments (100% GFP, 15 min lane in Figure 2.5) demonstrated 35% coincidence per GFP, suggesting a trend that decreased nucleosome fragment size is correlated to decreased coincidence per GFP. We hypothesized that shorter nucleosome fragments, especially tightly-wrapped mononucleosome fragments, are less-likely to be identified in a coincident event due to decreased accessibility of TOTO-3 for nucleosomal DNA and an increasing amount of nucleosome free linker DNA that can appear with longer digestion times. This issue may be mitigated using a different fluorescent labeling method, extending SCAN to the study of short nucleosome fragments.

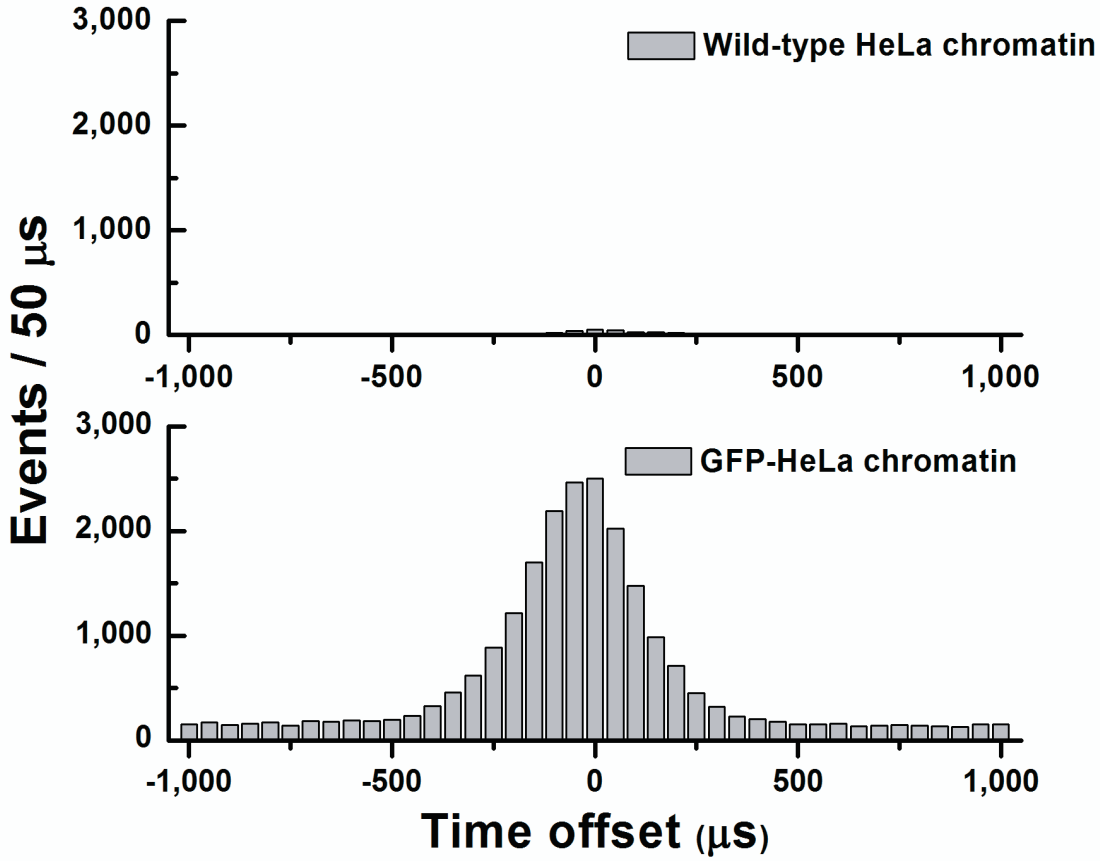

Figure 2.12: A time-coincidence histogram (TCH) illustrates the absence of coincident two-color when analyzing chromatin from wild-type HeLa nuclei. With GFP-HeLa chromatin from the 5 minute digestion, a Gaussian peak, corresponding to intact chromatin molecules emitting two fluorescent colors, emerged from a background of uncorrelated events. By integrating the area under the peak and subtracting the uncorrelated background, we observed more than 16,000 two-color chromatin molecules.

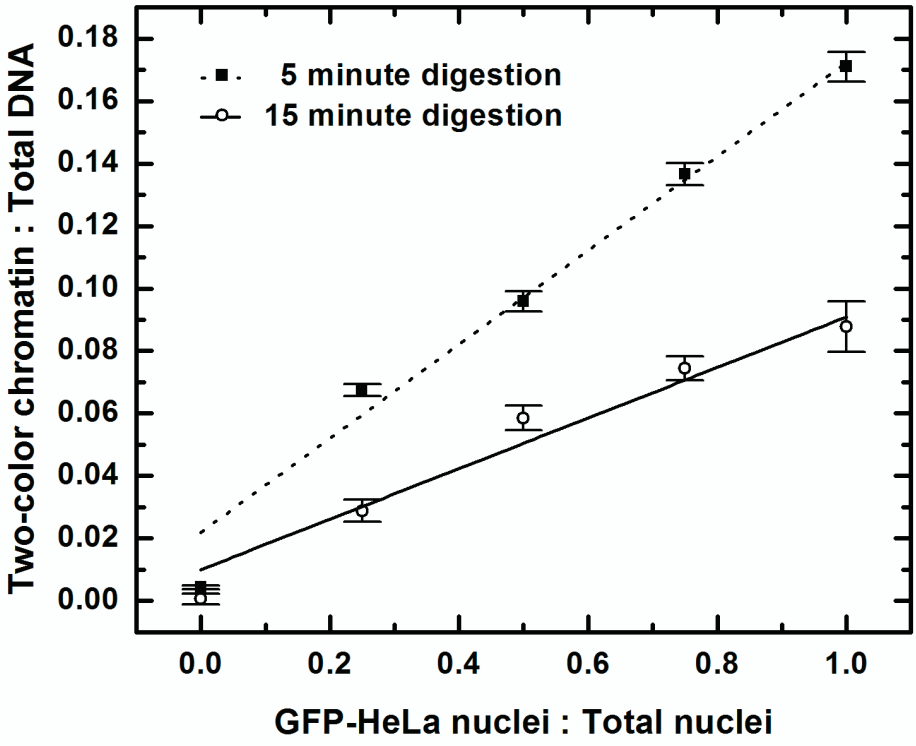

Figure 2.13: Nanofluidic SCAN of GFP-HeLa Chromatin at Different Digestion Times. The proportion of two-color chromatin molecules increased in direct proportion with GFP-HeLa nuclei content, as described by a linear fit with R^2=0.98 and R^2=0.95 for the 5 and 15 minute digestion assays, respectively. Error bars represent the propagated error from SMD of both the bound and unbound molecules.

Table 2.2: Chromatin throughput summary.

MNase Treatment (min)	5	25
DNA Concentration (pM)	588 ± 8	248 ± 2
Dual-Labeled Chromatin (molecules/min)	1067 ± 114	201 ± 36
H2B (molecules/min)	2116 ± 143	568 ± 67
DNA (molecules/min)	6238 ± 611	2287 ± 184
Gel Estimated Average Fragment Size (bp)	1600	500
DNA Throughput (Mbp/min)	10	1

To evaluate the throughput of our nanofluidic device , we utilized SCAN measurements of the 5 and 15 min digestions of 100% GFP-HeLa nuclei to compile Table 2.2. The rates for SMD of both DNA and H2B were averaged over 15 min of analysis. We calculated the detection rate for time-coincident molecules of dual-labeled chromatin by performing a background-corrected TCH analysis for each minute of SCAN. The throughput for all molecule types was consistently higher for chromatin from the 5 min digest, as compared to the 15 min digest, and suggested a higher sample concentration. The average fragment size was estimated separately using gel electrophoresis, as per Figure 2.5, and then combined with the DNA detection rate to derive the analysis throughput.

Sample concentration was verified in-situ by fitting a histogram of the time between each SMD event of a given color with an exponential model to calculate the sample concentration [16]. The burst separation describes the time elapsed between bursts and is related to the concentration of the sample analyzed. The burst separation (t) for each fluorescent dye color was examined separately and then fitted with an exponential model with free parameters β and λ. The fitted, mean burst separation is provided on each plot with a 95% confidence interval.

The exponential model used was:

$$\beta e^{-t\lambda} \tag{2.64a}$$

where

$$\lambda = CA\nu \tag{2.64b}$$

In this model, β is a scaling factor. The fitted parameter λ was related to 'A' is the cross-sectional area of the channel (0.125 μm^2) and ν is the flow speed of the molecules to calculate 'C', the concentration of molecules. The flow speed was derived using the methods outlined with Figure 2.11, which resulted in an in-situ measured concentration of 588 ± 8 pM for the DNA and 248 ± 2 pM for the H2B using the fitted data in Figure 2.14.

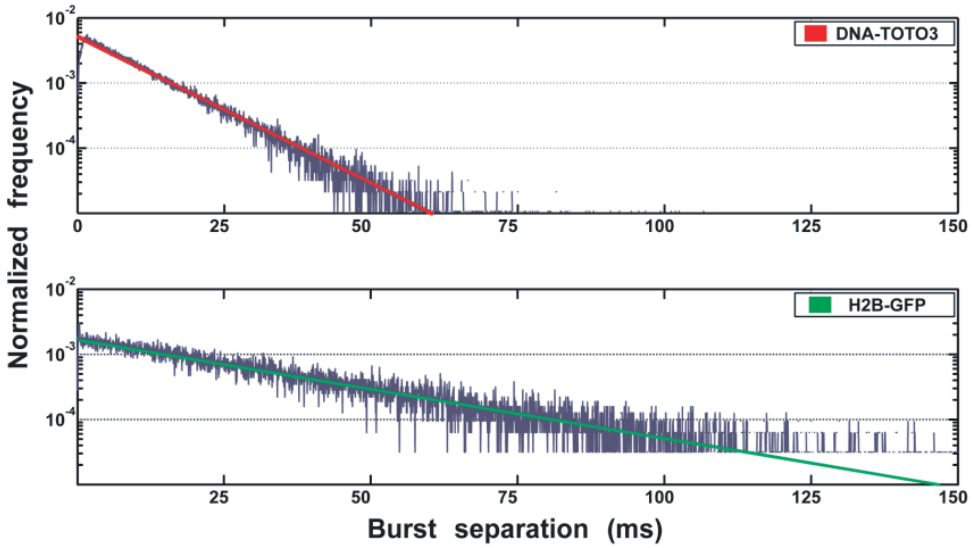

Figure 2.14: Exponential Fit of Single Molecule Burst Separation to Estimate Sample Concentration

2.4.3 Detection of DNA Methylation.

Our next goal was to determine if probes that were successfully applied to epigenomic analysis in the past could be used to detect a bona fide epigenetic mark on our nanofluidic platform. We focused on DNA methylation and used MBD1 as our probe, which has been shown to bind methylated DNA specifically [47]. Our test material was *HindIII* digested lambda DNA from a methylation deficient host, which we left unmethylated, or methylated in vitro using SssI DNA methylatransferase. *SssI* can methylate all 3,113 CpGs in the 48.5 kbp genome. We verified the effectiveness of the methylation reactions by digesting the DNA with the methylation sensitive restriction enzyme *HpaI* in Figure 2.6. Both DNA samples were stained with TOTO-3 and incubated with MBD1, which we labeled with Alexa Fluor 488. Alexa Fluor 488 is spectrally similar to GFP. The Alexa Fluor 488 labeled MBD1 retained its specificity for methylated DNA (Figure 2.7). To facilitate optimum binding to methylated DNA, we added a molar excess of MBD1 to the stained DNA. We found that dilution of this mixture into our 1x TBE-based buffer resulted in stable electrokinetic flow, as indicated by consistent SMD rates and low-levels of non-specific interaction between probes and the nanofluidic structure.

Figure 2.15 illustrates the number of coincident SMD events for MBD1 mixed with unmethylated DNA (top panel) or methylated DNA (bottom panel). Each mixture was analyzed for 15 min at applied potential of 100 V. The background level of coincidence events in the unmethylated DNA sample was due to an excess of probe present in the mixture. However, the central Gaussian peak in the methylated DNA sample showed that bound MBD-DNA complexes were detected above the high background. Methods have been described that could reduce background signals from free fluorescent probes [48].

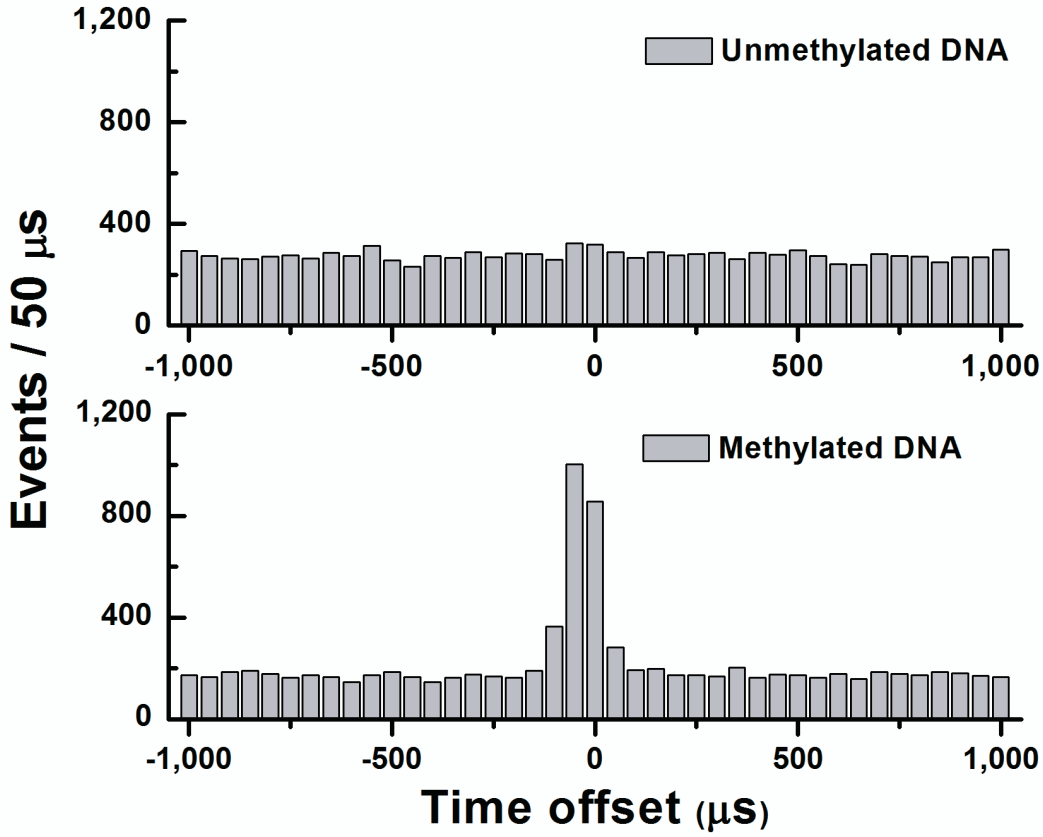

Figure 2.15: Detection of DNA Methylation. Unmethylated (top) and methylated (bottom) DNA samples labeled with TOTO-3 incubated with a molar excess of MBD1 probes labeled with Alexa Fluor 488. The emergent peak in the bottom panel demonstrates SMD of methylated DNA.

Similar to the chromatin analysis, we wanted to verify the authenticity of these detection events, so we prepared a dilution series of methylated and unmethylated DNA. We expected that with diminishing amounts of methylated DNA, we should observe a diminishing frequency of coincident events. This is consistent with our observed results summarized in Figure 2.16. There was a linear increase in the number of MBD-DNA complexes with increasing methylated DNA concentration, verifying the specificity of the signals detected by MBD1, and demonstrating the utility of nanofluidic SCAN for detecting bona fide epigenetic marks on individual molecules. Other fluorescence based approaches have been used to quantify DNA methylation [49], but these were not single molecule methods.

2.5 Summary and Conclusions

We have described the development of SCAN using a nanofluidic platform to analyze individual molecules using the same fluorescently labeled probes that have been used in bulk epigenetic analysis in molecular biology. Confinement using nanofluidic channels enabled single molecule analysis to be performed within the 100-1000 pM concentration range, which was essential for maintaining chromatin structure [50, 51]. We verified through multi-color SCAN that core histone octamers remained bound as nucleosomes within this nanofluidic environment during electrokinetic flow. Dilution of wild-type HeLa and GFP-HeLa nuclei was used to confirm the authenticity of coincidence detection. We observed chromatin fragments with a throughput of about 10 Mbp per minute using a single fluidic channel, indicating we could SCAN the entire genome of a fungal model organism in as few as eight minutes. We envision scaling our current throughput using parallel arrays with tens or hundreds of fluidic channels to perform analysis of larger organisms. For example, using 10 fluidic channels would allow 1x coverage of a 3 Gbp human

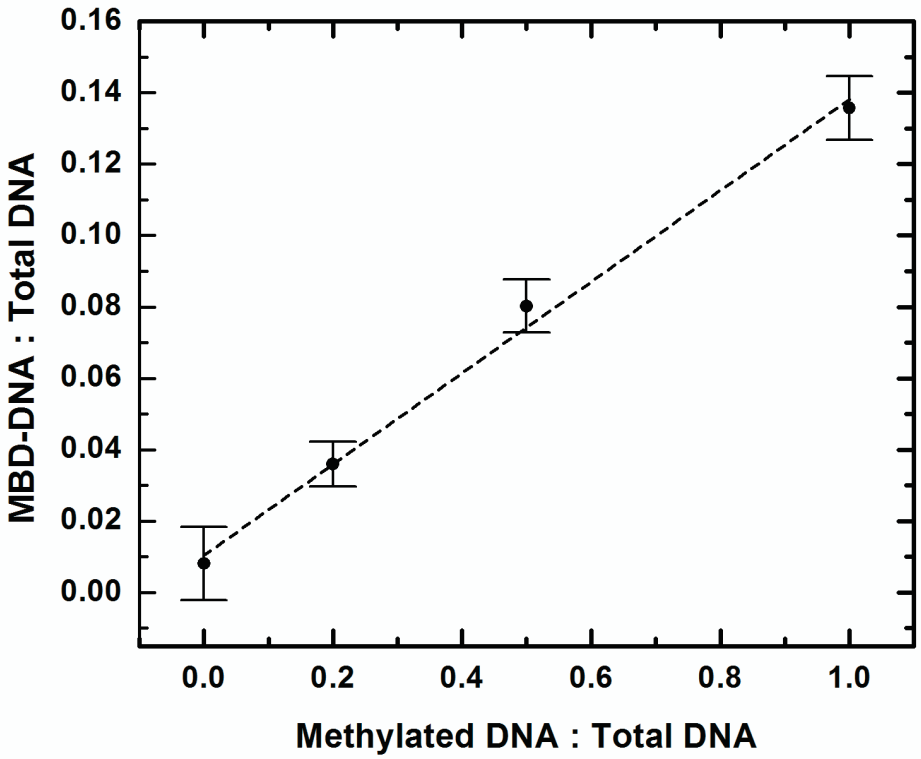

Figure 2.16: We analyzed mixtures of methylated and unmethylated DNA. The proportion of dual-color labeled MBD-DNA was shown to increase with methylated DNA, as described by a linear fit with R^2=0.99. Error bars represent the propagated error from SMD of both the bound and unbound molecules.

genome to be scanned in just 30 minutes.

Further reduction of the nanofluidic channel cross-section would enable SMD at higher concentrations and increase the signal to noise ratio for single molecule fluorescent analysis. Since the probability of detecting a coincident event randomly is related to the sample concentration in the inspection volume, this probability can be engineered by reducing the channel cross-section. With sufficiently narrow channels the flowing chromatin or DNA molecules can be elongated allowing multiple fluorescent labels to be spatially separated and resolved. This may permit molecular mapping with spatial resolution sufficient to identify multiple epigenetic marks on a single nucleosome or to distinguish marks on adjacent nucleosomes. Prior work has shown optical resolution of molecular length to 114 nm, equivalent to about 335 bp, during rapid flow of lambda DNA [52]. This spatial resolution was possible using nanofluidic channels with cross sectional areas on the order of 0.01 μm^2, an order of magnitude less than was used in these experiments. It is likely that smaller channels will allow us to identify molecules with multiple bound probes and resolve their positions on a chromatin fragment.

The applications of SCAN we described so far are analytical in nature, capable of revealing the frequency and coincidence of epigenetic mark placement in the genome. However, just as flow cytometers can have analytical or preparative capabilities, we believe the SCAN platform can be modified to rapidly sort chromatin fragments in real time based on their fluorescence signatures. This could provide an alternative to ChIP by allowing the selection and recovery of individual chromatin fragments with a desired set of epigenetic features. To identify exact epigenetic mark placement in a genome-wide context, SCAN sorted molecules could then be recovered for further analysis using PCR or DNA sequencing. Such an instrument would make SCAN-seq possible, an alternative to ChIP-seq. Im-

portantly SCAN can monitor multiple fluorescent marks simultaneously, enabling multiplexed, genome-wide epigenomic analysis not currently possible with ChIP.

References

[1] K. Luger, A. W. Mader, R. K. Richmond, D. F. Sargent, and T. J. Richmond, "Crystal structure of the nucleosome core particle at 2.8 angstrom resolution," *Nature*, vol. 389, no. 6648, pp. 251–260, 1997.

[2] T. Jenuwein and C. D. Allis, "Translating the histone code," *Science*, vol. 293, no. 5532, pp. 1074–1080, 2001.

[3] R. J. Klose and A. P. Bird, "Genomic dna methylation: the mark and its mediators," *Trends In Biochemical Sciences*, vol. 31, no. 2, pp. 89–97, 2006.

[4] T. S. Mikkelsen, M. C. Ku, D. B. Jaffe, B. Issac, E. Lieberman, G. Giannoukos, P. Alvarez, W. Brockman, T. K. Kim, R. P. Koche, W. Lee, E. Mendenhall, A. O'Donovan, A. Presser, C. Russ, X. H. Xie, A. Meissner, M. Wernig, R. Jaenisch, C. Nusbaum, E. S. Lander, and B. E. Bernstein, "Genome-wide maps of chromatin state in pluripotent and lineage-committed cells," *Nature*, vol. 448, no. 7153, pp. 553–U2, 2007.

[5] A. P. Feinberg, "Phenotypic plasticity and the epigenetics of human disease," *Nature*, vol. 447, no. 7143, pp. 433–440, 2007.

[6] R. A. Waterland and R. L. Jirtle, "Transposable elements: Targets for early nutritional effects on epigenetic gene regulation," *Molecular And Cellular Biology*, vol. 23, no. 15, pp. 5293–5300, 2003.

[7] M. D. Anway, A. S. Cupp, M. Uzumcu, and M. K. Skinner, "Epigenetic transgenerational actions of endocrine disruptors and mate fertility," *Science*, vol. 308, no. 5727, pp. 1466–1469, 2005.

[8] I. C. G. Weaver, N. Cervoni, F. A. Champagne, A. C. D'Alessio, S. Sharma, J. R. Seckl, S. Dymov, M. Szyf, and M. J. Meaney, "Epigenetic programming by maternal behavior," *Nature Neuroscience*, vol. 7, no. 8, pp. 847–854, 2004.

[9] B. E. Bernstein, A. Meissner, and E. S. Lander, "The mammalian epigenome," *Cell*, vol. 128, no. 4, pp. 669–681, 2007.

[10] B. Ren, F. Robert, J. J. Wyrick, O. Aparicio, E. G. Jennings, I. Simon, J. Zeitlinger, J. Schreiber, N. Hannett, E. Kanin, T. L. Volkert, C. J. Wilson, S. P. Bell, and R. A. Young, "Genome-wide location and function of dna binding proteins," *Science*, vol. 290, no. 5500, p. 2306, 2000.

[11] A. Barski, S. Cuddapah, K. R. Cui, T. Y. Roh, D. E. Schones, Z. B. Wang, G. Wei, I. Chepelev, and K. J. Zhao, "High-resolution profiling of histone methylations in the human genome," *Cell*, vol. 129, no. 4, pp. 823–837, 2007.

[12] M. Weber, J. J. Davies, D. Wittig, E. J. Oakeley, M. Haase, W. L. Lam, and D. Schubeler, "Chromosome-wide and promoter-specific analyses identify sites of differential dna methylation in normal and transformed human cells," *Nature Genetics*, vol. 37, no. 8, pp. 853–862, 2005.

[13] X. Y. Zhang, J. Yazaki, A. Sundaresan, S. Cokus, S. W. L. Chan, H. M. Chen, I. R. Henderson, P. Shinn, M. Pellegrini, S. E. Jacobsen, and J. R. Ecker, "Genome-wide high-resolution mapping and functional analysis of dna methylation in arabidopsis," *Cell*, vol. 126, no. 6, pp. 1189–1201, 2006.

[14] L. P. O'Neill, M. D. VerMilyea, and B. M. Turner, "Epigenetic characterization of the early embryo with a chromatin immunoprecipitation protocol applicable to small cell populations," *Nature Genetics*, vol. 38, no. 7, pp. 835–841, 2006.

[15] B. E. Bernstein, T. S. Mikkelsen, X. H. Xie, M. Kamal, D. J. Huebert, J. Cuff, B. Fry, A. Meissner, M. Wernig, K. Plath, R. Jaenisch, A. Wagschal, R. Feil, S. L. Schreiber, and E. S. Lander, "A bivalent chromatin structure marks key developmental genes in embryonic stem cells," *Cell*, vol. 125, no. 2, pp. 315–326, 2006.

[16] M. Foquet, J. Korlach, W. Zipfel, W. W. Webb, and H. G. Craighead, "Dna fragment sizing by single molecule detection in submicrometer-sized closed fluidic channels," *Analytical Chemistry*, vol. 74, no. 6, pp. 1415–1422, 2002.

[17] L. A. Neely, S. Patel, J. Garver, M. Gallo, M. Hackett, S. McLaughlin, M. Nadel, J. Harris, S. Gullans, and J. Rooke, "A single-molecule method for the quantitation of microrna gene expression," *Nature Methods*, vol. 3, no. 1, pp. 41–46, 2006.

[18] R. L. Nolan, H. Cai, J. P. Nolan, and P. M. Goodwin, "A simple quenching method for fluorescence background reduction and its application to the direct, quantitative detection of specific mrna," *Analytical Chemistry*, vol. 75, no. 22, pp. 6236–6243, 2003.

[19] S. M. Stavis, S. C. Corgie, B. R. Cipriany, and H. G. Craighead, "Single molecule analysis of bacterial polymerase chain reaction products in submicrometer fluidic channels," *Biomicrofluidics*, vol. 1, no. 3, 2007.

[20] S. M. Nie, D. T. Chiu, and R. N. Zare, "Real-time detection of single-molecules in solution by confocal fluorescence microscopy," *Analytical Chemistry*, vol. 67, no. 17, pp. 2849–2857, 1995.

[21] J. Enderlein, D. L. Robbins, W. P. Ambrose, and R. A. Keller, "Molecular shot noise, burst size distribution, and single-molecule detection in fluid flow: Effects of multiple occupancy," *Journal Of Physical Chemistry A*, vol. 102, no. 30, pp. 6089–6094, 1998.

[22] X. Michalet, A. N. Kapanidis, T. Laurence, F. Pinaud, S. Doose, M. Pflughoefft, and S. Weiss, "The power and prospects of fluorescence microscopies and spectroscopies," *Annual Review Of Biophysics And Biomolecular Structure*, vol. 32, pp. 161–182, 2003.

[23] W. E. Moerner and D. P. Fromm, "Methods of single-molecule fluorescence spectroscopy and microscopy," *Review Of Scientific Instruments*, vol. 74, no. 8, pp. 3597–3619, 2003.

[24] B. N. G. Giepmans, S. R. Adams, M. H. Ellisman, and R. Y. Tsien, "Review - the fluorescent toolbox for assessing protein location and function," *Science*, vol. 312, no. 5771, pp. 217–224, 2006.

[25] B. Kirby, *Micro- and nanoscale fluid mechanics : transport in microfluidic devices*. New York: Cambridge University Press, 2010.

[26] D. Tritton, *Physical Fluid Dynamics*. New York: Oxford University Press, 2nd ed., 1988.

[27] A. Mani, T. A. Zangle, and J. G. Santiago, "On the propagation of concentration polarization from microchannel-nanochannel interfaces part i: Analytical model and characteristic analysis," *Langmuir*, vol. 25, no. 6, pp. 3898–3908, 2009.

[28] T. A. Zangle, A. Mani, and J. G. Santiago, "On the propagation of concentration polarization from microchannel-nanochannel interfaces part ii: Numerical and experimental study," *Langmuir*, vol. 25, no. 6, pp. 3909–3916, 2009.

[29] T. A. Zangle, A. Mani, and J. G. Santiago, "Theory and experiments of concentration polarization and ion focusing at microchannel and nanochannel interfaces," *Chemical Society Reviews*, vol. 39, no. 3, pp. 1014–1035, 2010.

[30] J. W. Hong and S. R. Quake, "Integrated nanoliter systems," *Nature Biotechnology*, vol. 21, no. 10, pp. 1179–1183, 2003.

[31] A. M. Berezhkovskii, A. Szabo, and G. H. Weiss, "Theory of single-molecule fluorescence spectroscopy of two-state systems," *Journal Of Chemical Physics*, vol. 110, no. 18, pp. 9145–9150, 1999.

[32] E. Barkai, Y. J. Jung, and R. Silbey, "Theory of single-molecule spectroscopy: Beyond the ensemble average," *Annual Review Of Physical Chemistry*, vol. 55, pp. 457–507, 2004.

[33] R. J. McIntyre, "Multiplication noise in uniform avalanche diodes," *Ieee Transactions on Electron Devices*, vol. ED13, no. 1, pp. 164–168, 1966.

[34] R. J. McIntyre, "A new look at impact ionization - part i: A theory of gain, noise, breakdown probability, and frequency response," *Ieee Transactions on Electron Devices*, vol. 46, no. 8, pp. 1623–1631, 1999.

[35] P. Yuan, K. A. Anselm, C. Hu, H. Nie, C. Lenox, A. L. Holmes, B. C. Streetman, J. C. Campbell, and R. J. McIntyre, "A new look at impact ionization - part ii: Gain and noise in short avalanche photodiodes," *Ieee Transactions on Electron Devices*, vol. 46, no. 8, pp. 1632–1639, 1999.

[36] C. E. Shannon, "Communication in the presence of noise," *Proceedings of the Institute of Radio Engineers*, vol. 37, no. 1, pp. 10–21, 1949.

[37] D. Magde, W. W. Webb, and E. Elson, "Thermodynamic fluctuations in a reacting system - measurement by fluorescence correlation spectroscopy," *Physical Review Letters*, vol. 29, no. 11, pp. 705–708, 1972.

[38] D. Magde, E. L. Elson, and W. W. Webb, "Fluorescence correlation spectroscopy .2. experimental realization," *Biopolymers*, vol. 13, no. 1, pp. 29–61, 1974.

[39] D. Magde, W. W. Webb, and E. L. Elson, "Fluorescence correlation spectroscopy .3. uniform translation and laminar-flow," *Biopolymers*, vol. 17, no. 2, pp. 361–376, 1978.

[40] R. D. Kornberg, J. W. Lapointe, and Y. Lorch, "Preparation of nucleosomes and chromatin," *Methods In Enzymology*, vol. 170, pp. 3–14, 1989.

[41] M. Foquet, J. Korlach, W. R. Zipfel, W. W. Webb, and H. G. Craighead, "Focal volume confinement by submicrometer-sized fluidic channels," *Analytical Chemistry*, vol. 76, no. 6, pp. 1618–1626, 2004.

[42] S. M. Stavis, J. B. Edel, K. T. Samiee, and H. G. Craighead, "Single molecule studies of quantum dot conjugates in a submicrometer fluidic channel," *Lab On A Chip*, vol. 5, no. 3, pp. 337–343, 2005.

[43] W. P. Ambrose, P. M. Goodwin, J. H. Jett, A. Van Orden, J. H. Werner, and R. A. Keller, "Single molecule fluorescence spectroscopy at ambient temperature," *Chemical Reviews*, vol. 99, no. 10, pp. 2929–2956, 1999.

[44] T. Kanda, K. F. Sullivan, and G. M. Wahl, "Histone-gfp fusion protein enables sensitive analysis of chromosome dynamics in living mammalian cells," *Current Biology*, vol. 8, no. 7, pp. 377–385, 1998.

[45] K. Wojcik and J. W. Dobrucki, "Interaction of a dna intercalator draq5, and a minor groove binder syto17, with chromatin in live cells-influence on chromatin organization and histone-dna interactions," *Cytometry Part A*, vol. 73A, no. 6, pp. 555–562, 2008.

[46] R. M. Martin, H. Leonhardt, and M. C. Cardoso, "Dna labeling in living cells," *Cytometry Part A*, vol. 67A, no. 1, pp. 45–52, 2005.

[47] H. F. Jorgensen, K. Adie, P. Chaubert, and A. P. Bird, "Engineering a high-affinity methyl-cpg-binding protein," *Nucleic Acids Research*, vol. 34, no. 13, 2006.

[48] X. Wang, Y. Song, M. Song, Z. Wang, T. Li, and H. Wang, "Fluorescence polarization combined capillary electrophoresis immunoassay for the sensitive detection of genomic dna methylation," *Analytical Chemistry*, vol. 81, no. 19, p. 7995, 2009.

[49] D. Stach, O. Schmitz, S. Stilgenbauer, A. Benner, H. Dohner, M. Wiessler, and F. Lyko, "Capillary electrophoretic analysis of genomic dna methylation levels," *Nucleic Acids Research*, vol. 31, no. 2, p. e2, 2003.

[50] T. A. Hagerman, Q. Fu, B. Molinie, J. Denvir, S. Lindsay, and P. T. Georgel, "Chromatin stability at low concentration depends on histone octamer saturation levels," *Biophysical Journal*, vol. 96, no. 5, pp. 1944–1951, 2009.

[51] C. Claudet, D. Angelov, P. Bouvet, S. Dimitrov, and J. Bednar, "Histone

octamer instability under single molecule experiment conditions," *Journal Of Biological Chemistry*, vol. 280, no. 20, pp. 19958–19965, 2005.

[52] C. H. Reccius, S. M. Stavis, J. T. Mannion, L. P. Walker, and H. G. Craighead, "Conformation, length, and speed measurements of electrodynamically stretched dna in nanochannels," *Biophysical Journal*, vol. 95, no. 1, pp. 273–286, 2008.

CHAPTER 3

SINGLE MOLECULE SORTING IN NANOFLUIDICS

3.1 Introduction

In chromatin, chemical modifications to histone proteins and DNA alter the status of the epigenome and influence gene regulation and normal development. Their aberrant placement has been linked to the onset of cancer [1, 2] and other diseases. Bisulfite conversion and immunoprecipitation (IP) have been used extensively to examine these modifications on both locus-specific and genome-wide scales. These approaches have limitations in terms of material handling and/or multiplexed detection. Conventional chromatin immunoprecipitation (ChIP) requires an abundance of input material, often $10^3 - 10^6$ cells, cells for genome-wide studies, to compensate for $> 99\%$ material loss during processing [3, 4]. This problem compounds for sequential re-ChIP reactions, limiting the study of multivalent modifications [4], which could provide a clear view of epigenetic coordination. While DNA methylation analysis using bisulfite conversion can operate on picogram quantities of DNA [5–7], the conversion causes degradation of $> 90\%$ of the input DNA. Methods that combine ChIP and bisulfite sequencing in a sequential process have demonstrated progress in multiplexed epigenetic analysis [8]. There continues to be active research in reducing the input material requirements and in automation of the processes for epigenetic analysis [9–11]. Furthermore, there is interest in additional capability for simultaneous detection of multiple epigenetic modifications in the same material.

[0]This chapter is reprinted (adapted) from B.R. Cipriany, P.J. Murphy, J.A. Hagarman, A. Cerf, D. Latulippe, S.L. Levy, J.J. Benitez, C.P. Tan, J. Topolancik, P.D. Soloway, H.G. Craighead, Real-Time Analysis and Selection of Methylated DNA by Fluorescence-Activated Single Molecule Sorting in a Nanofluidic Channel, PNAS (Accepted for Publication, In Press). Copyright 2012 Proceedings of the National Academy of Sciences, USA. Authors not required to obtain permission for usage in dissertations.

Miniaturized fluidic devices offer a compelling toolset for multiplexed detection and efficient sample handling in analytical and preparatory systems. Microfluidics have performed complicated workflows that include nanoliter sample handling [12] and incorporate electrodes [13–16] or valves [12, 17] for sophisticated processing. Nanofluidics have achieved attoliter-scale fluid volume confinement to isolate and quantify the attributes of individual molecules, which can be obscured during ensemble measurements. These devices have recently been demonstrated for single molecule analysis on native chromatin [18]. However, adaptation of these devices to include fluorescence activated sorting would enable color-multiplexed detection in real-time and collection of molecules with specific epigenetic modifications. Existing fluorescence activated techniques for cell [19, 20] and droplet [21] sorting lack the volume confinement necessary for sorting individual, single fluorophore-labeled molecules at picomolar concentrations and above, which are favorable for protein or antibody binding and chromatin stability [22, 23].

Here we present a bifurcated nanofluidic device for real-time detection and automated sorting of individual methylated DNA molecules. These molecules were selected from a mixture that included unmethylated DNA and were recognized using a fluorescently-labeled methyl binding domain protein-1 (MBD1), which binds specifically to double-stranded, methylated DNA [24]. We discuss the technologies that enabled us to identify methylated DNA bound with MBD1 using its fluorescence signature. We demonstrate accurate evaluation of this fluorescence signature to actuate sorting of these molecules from the mixture. We show recovery of sorted material and independently verify molecule enrichment by quantitative polymerase chain reaction (qPCR) to elucidate opportunities for post-sorting analysis. We report the proof-of-principle demonstration of our single molecule sorter for color-multiplexed epigenetic analysis and sample recovery of limited genetic

material.

3.2 Theoretical Background

3.2.1 Circuit Model for a Nanofluidic Sorter

Circuit Model for a Bifurcated Nanofluidic Device One of the fascinating aspects of nanofluidic devices is their remarkable similarity to solid state circuit components. While this observation applies to hydrodynamic circuit model equivalents for pressure-actuated Poiseuille flows, I will narrowly focus on lumped-element electrical circuit components applicable for electrokinetic flows. Since there is no energy storage in or coupling to magnetic fields, there is no inductive component. Less intuitive is the treatment of capacitive components. From the previous chapter, we evaluated the electroosmotic flow velocity 2.31 from an electric field applied parallel to the wall surface (in the x-direction). Continuing that observation, we note that ion transport giving rise to an electrical current occurs in the x-direction, where the only equivalent circuit element is the resistance of the fluid itself. This seems striking at first, but the charge that is contained with the electric double layer (EDL) does not contribute to the equivalent circuit model for actuation of the device. In fact, after the surface charge at the wall ϕ_{wall} has been electrostatically shielded by the counter-ion in solution, causing the formation of the immobile Stern layer, all y-oriented electric field is confined within the equivalent capacitor of the EDL and, to a rather good approximation, does not couple with the applied electric field in the x-direction. Therefore, in simplest form, a bifurcated nanofluidic device can be modeled as a Y-network of resistive elements.

Actuation of High Resistance Nanofluidic Devices The resistance of our nanofluidic device can be estimated through the following geometric approximation:

$$R = \frac{\rho L}{A} \tag{3.1}$$

where L is the length of the fluidic channel, A is the cross-sectional area, and ρ is the bulk resistivity of the buffer solution, assuming homogeneity. For the given device geometry, the microfluidic component has dimensions 10 mm x 40 μm x 0.25 μ (L x w x h) and the nanofluidic has dimensions 55 μm x 0.5 μm x 0.25 μm (L x w x h). Given a 1x Tris-EDTA solution bulk conductivity of 500-700 $\frac{\mu mhos}{cm}$, or equivalently about 1500 $\Omega - cm$, we estimate an equivalent device resistance of 2×10^{10} Ω. In measurement, as discussed later, the actual resistance is closer to 0.35×10^{10} Ω. In either case, actuation of this device is challenging as there are few switching components with off-state resistances in excess of 100 $G\Omega$ that are also capable of swinging a 100 V potential with $\tau = 1$ ms.

Fortunately, a small collection of suitable components do exist as miniaturized mechanical and solid state relays, named the reed relay and optocoupled solid state relay (SSR), respectively. The reed relay is effectively a microelectromechanical system (MEMS) device, which uses a inductively-coupled reed-like contact that can be deflected to open or close a switch. The reed relay satisfies the aforementioned criteria for switching and also produces a delightful tone when actuated with a function generator at 440 Hz to assist in tuning one's voice during a long experiment. Unfortunately, this relay experiences an electrically-noisy bounce during switching, which can have an adverse affect on molecule switching, and will suffer mechanical failure after about 10 million cycles. The SSR, while not as helpful in musical pursuits, provides no-bounce switching and can be used 'indefinitely.'

Table 3.1: Estimated Capacitance of an Electrode in Tris-EDTA.

Ion	pH	Valence (@pH)	Concentration (mM)	λ_D (nm)	Capacitance (μF)
Tris	8.0	+1	10	3.3	7.2
EDTA	8.0	-3	1	0.98	2.1

The primary downfall of the SSR is the off-state leakage current, which is voltage dependent.

Actuation is not complete without placing electrodes into the reservoir of buffer solution. Normally, for devices operated with a constant DC bias, this is trivial, but in a voltage-switched mode of operation we now consider the capacitance of these electrodes. This capacitance arises from the formation of an EDL at the electrode-electrolyte interface. Using a modified formulation for a parallel-plate capacitor:

$$C_{electrode} = \frac{\epsilon_r \epsilon_0 A}{D} = \frac{\epsilon_r \epsilon_0 A}{\lambda_D} \tag{3.2}$$

$$\lambda_D = \sqrt{\frac{\epsilon_r \epsilon_0 k_B T}{2 N_A (ze)^2 I}} \tag{3.3}$$

where ϵ_r is the relative permittivity (80 in water at low frequencies), ϵ_0 is the free-space permittivity, k_B, the Boltzmann constant, T the temperature in Kelvin, N_A the Avogadro number, z the magnitude of integer charge valence, e is the fundamental charge, I the molar ionic strength multiplied by 1000, A the surface area of the electrode, λ_D the Debye screening length. The following table summarizes the λ_D for several popular buffer components and the resulting electrode capacitance, assuming an electrode with area $A = 10\ mm^2$.

It is important to keep in mind that these are coarse estimates. We know

that the relative permittivity, ϵ_r, strongly depends on the accuracy of the EDL model. For example, if we use the the Gouy-Chapman-Stern model modified to include solvated and adsorbed ions, ϵ_r is better estimated by a value of 8, which when compounded over this calculation would cause a 30-fold reduction in the estimated capacitance. We also know from prior reading that TE experiences strong pH swings, and therefore valence changes, as a function of temperature.

To complete the model, we must incorporate the resistance of the electrodes in the solution. This resistance is a charge-transfer resistance that depends on the electrode material, buffer, and electrochemistry (redox rate). These effects are captured, to some extent, in the equivalent Randles circuit model. The electrode resistance-area product has been estimated for a 1 M buffer concentration to be 10^{-3} to 10^{-5} Ωm^2. Scaling this according to the buffer concentrations we use, around 10 mM, would cause an electrode resistance on the order of 1 $k\Omega$. With this information we can now model the corner frequency (-3 dB point), which coincides with the equivalent τ (RC time constant) for this two-pole, low-pass circuit.

$$Z_\omega = (\frac{R_{e1}}{1 + j\omega C_{e1} R_{e1}}) + R_{soln} + (\frac{R_{e2}}{1 + j\omega C_{e2} R_{e2}}) \tag{3.4}$$

where R_e is the electrode resistance, C_e is the electrode capacitance, and R_{soln} is the resistance of the fluid bulk within the nanofludic channel. Using a Bode plot, we can now visualize the frequency response of this circuit:

In conclusion to these mathematical models, it is clear that the role of electrolyte selection and electrode are the critical factors to controlling the frequency response of our actuation circuit. To the end of characterizing these circuit parameters, it occurs to me that a simple unenclosed slot, perhaps several millimeters in length, filled with a known buffer solution and actuated by electrodes at a known

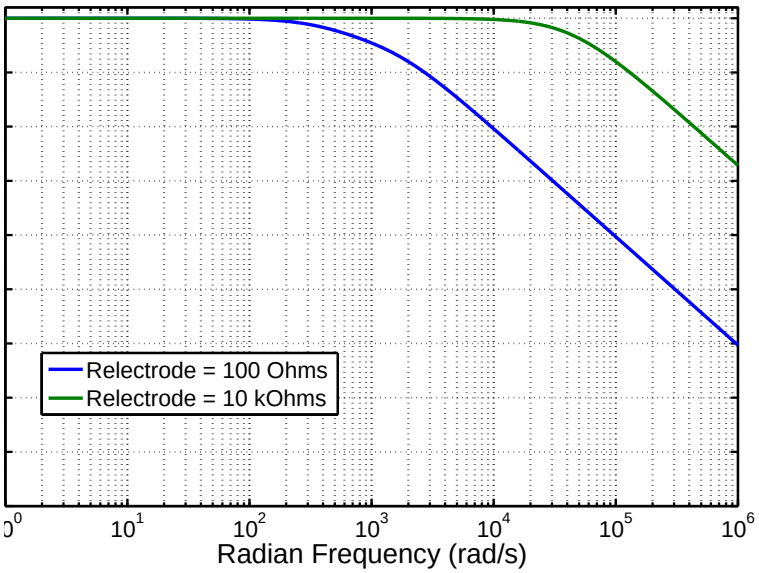

Figure 3.1: Calculated Frequency Response for an Electrode in 1x TE Electrolyte. This Bode plot illustrates the frequency response from a double-pole, low-pass circuit model for two electrodes placed in a 1x TE solution. A pole is associated with the equivalent capacitance from the Debye layer at each electrode, which each have a unique capacitance due to the difference in concentration for the respective counter-ion. The capacitance of these devices is modeled based upon a modified relative permittivity, $\epsilon_r = 8$.

separation would provide a very simple, yet effective way to establish these circuit parameters without a microfluidic or nanofluidic channel. Furthermore, in future experiments, I can envision the use of a deposited, ring-shaped electrode at the surround of a fluid reservoir port to actuate these flows for the purpose of reducing capacitance, as compared to a wire dipped into solution.

Y-Δ Network Impedance Transformations The Y-Δ transformation provides a convenient way to adjust the switching time constant, τ, using a parallel, external resistor network. This transform relates the impedance of a Y-shaped, or sometimes called t-shaped, network to a Δ-shaped, or sometimes called pi-shaped, network.

To transform impedance elements in a Y-network into a Δ-network:

$$R_a = \frac{R_1R_2 + R_2R_3 + R_3R_1}{R_1} \tag{3.5}$$

$$R_b = \frac{R_1R_2 + R_2R_3 + R_3R_1}{R_2} \tag{3.6}$$

$$R_c = \frac{R_1R_2 + R_2R_3 + R_3R_1}{R_3} \tag{3.7}$$

To transform impedance elements in a Δ-network into a Y-network:

$$R_1 = \frac{R_bR_c}{R_a + R_b + R_c} \tag{3.8}$$

$$R_2 = \frac{R_aR_c}{R_a + R_b + R_c} \tag{3.9}$$

$$R_3 = \frac{R_aR_b}{R_a + R_b + R_c} \tag{3.10}$$

We have constructed this network using high-precision, discrete resistor elements for R_a and R_b, since these resistors are paired to branches of the bifurcated device that have equal path length and therefore equal resistance. However, for R_c, the series combination of a discrete resistor and a potentiometer are used to 'tune' the exact resistance. This allows the input microfluidic branch of the sorter

to be of different length. Of course, this can be avoided altogether by making each branch of the device equal in length, but practical constraints sometimes prevent such 3-fold symmetry in the device layout.

The external network of resistors causes the overall RC time constant of the device to be dominated by the capacitance of electrodes and resistance of external network, instead of the extremely high resistance of the fluidic channels. Additionally, because these resistors operate in parallel, they act as a current divider, so the majority of any leakage current from the relays is routed into the external resistors instead of actuating the device, thus providing improved current isolation. When the resistors are set to a balanced configuration, one that matches the resistive split ratios within the nanofluidic, it also serves to enforce the node voltages at each output, such that neither node can drop to a potential below that at the device's bifurcation - ensuring that during switching disconnect, that molecules do not transist in the opposite direction. Unfortunately, the side-effect of this design is a more-crowded electrode interface into the device with resistors that cause substantial joule heating losses, I^2R. These heat losses need to be dissipated using appropriately rated $\frac{1}{8} - \frac{1}{2}\ W$ resistor elements to preserve linear circuit operation and the resistors need to be placed at a modest distance (centimeters) away from the fluidic reservoirs to avoid conducting the dissipated heat into the sample.

Complete Network Model for a Nanofluidic Sorter We now superposition the various circuit elements that have been developed and modeled for the nanofluidic sorter. At the heart of the design is the resistive Y-network representing the bifurcated nanofluidic device, in electrical parallel is a Δ-network of external resistors to tune the applied voltages at the device nodes and reduce the overall switching time constant, and a lumped-element equivalent for the electrodes and the SSR switches. A complete diagram is provided in Fig. 3.2.

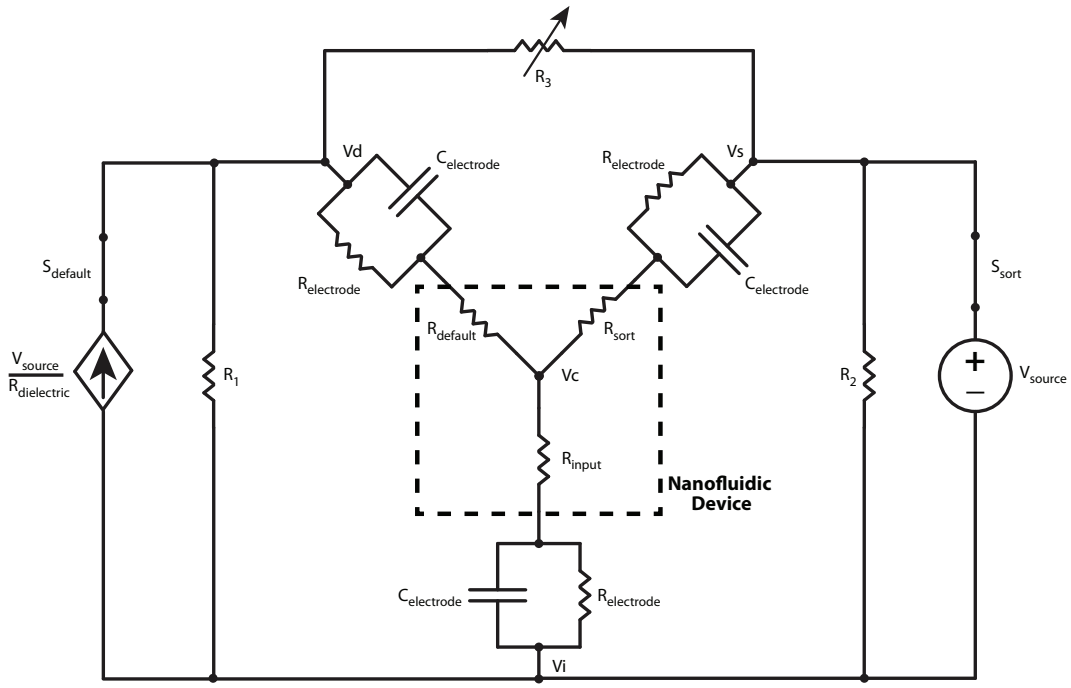

Figure 3.2: Circuit Model for Nanofluidic Sorter. R_1,R_2,and R_3 compose the external delta network of resistors used to adjust the switching time constant of the nanofluidic device. Solid state relays actuate each branch of the Y-junction fluidic channel. Since these relays do not physically disconnect from the circuit, the voltage-dependent leakage current of the off-state relay is modeled with a dependent current source.

The circuit has been illustrated with a dependent current source, to emphasize the possible current contributions of the SSR relay when in the electrically-disconnected state. With the external resistor network in place this current source is essentially negligible to the operation of the device and can be replaced with an idealized, open switch. In the open or off-state, either the node V_D or V_S will be forced to the same node voltage as V_C, using the balanced external resistor circuit, and thereby prevent a negative-potential difference for $V_S - V_C$ that would cause sorted molecules to re-enter the input or be driven to the default output.

Experimental Observations on Nanofluidic Sorter Operation Through many repeated uses of the nanofluidic sorter, I have made several observations of potential use to its inheritors. The first observation concerns the tuning of the external resistor network - it need only be made once for a given device layout geometry. Once set, the variations due to fabrication effects will be reasonably uniform across a given device, with the primary exception being asperities and other non-symmetric artifacts occurring within the nanofludic bifurcation itself. The second observation concerns the preparation of the device for sorting - many rinses of the device should be performed prior to applying electrokinetic drive for an extended period of time. Despite care to the contrary, I have noticed that reused external electrodes shed flecks of dried salt into the device reservoir and that electrodes can break off microscale glass shards from the delicate edges of the through-wafer holes. Both sources of nano-shmutz are notorious for being drawn into these devices and it only takes 1 piece to clog and break the device symmetry irreversibly. Remember this is Stoke's flow, don't wait around hoping for some convective mixing to remove your problem, its not going to happen. The third observation pertains to the electrode capacitance - I suggest a future implementation of a thin ring electrode that is deposited on device surface. My

estimates indicate that a 200 μm thick, 4 mm diameter concentric ring placed around the reservoir could reduce the electrode capacitance by 10-50 fold depending on exact geometry. And in tradition of holding people in utter suspense, I've saved the best for last: the fourth observation is that over time (on the order of 1-2 hours) the control of molecule sorting begins to break down. At first observation, I thought it to be fouling of the device from non-specific surface interactions, which does occur. However, more recently I have come to appreciate that this is due to ion concentration polarization effects. The narrowing of the microfluidic channel into a nanofluidic channel causes preferential migration and accumulation or depletion of the ions in buffer near these transitions in geometry. In some cases, I have observed current rectification behaviors in devices where the direction of flow was maintained in one branch for a prolonged period of time and then attempts were made to switch into the adjacent branch. The severity of this effect is both dependent on device geometry and time. Ultimately, this brings a new dimension of device operation that is rooted in non-linear circuits - as this effect breaks the symmetry in time reversible flows and gives rise to diode and transistor operation. It is only now in retrospect that I appreciate having built a 3-terminal device that may possibly be described as the first bipolar junction fluidic transistor.

3.2.2 Real-Time Signal Processing

Until now we have applied our single molecule detection (SMD) as a post-experiment process. This affords the experimenter maximum flexibility in discerning and applying the analysis conditions to optimize SMD. However, if we are to perform sufficiently rapid detection and then actuate molecule sorting, this process must occur in real-time. The concepts that follow are largely derived from digital signal processing methods and therefore have generalized applicability. With the ever-

decreasing cost of digital computation, the following methods can be implemented using cost-effective, off-the-shelf hardware. We will discuss such implementation on a field programmable gate array (FPGA)to achieve real-time SMD.

Basic Real-Time Detection (BRTD) Real-time detection is possible using the general principles developed in the previous chapter. In implementation, this requires hardware that operates by synchronously-clocked computation. Based upon our prior discussion of the Nyquist sampling theorem, the operational frequency, or cycle time, of the system clock should be on the order of the fluorescence radiative lifetime or the minimum pulse-width output by our detectors. Nominally, a system clock of 50 MHz, equivalently a cycle time of 20ns, is sufficient and readily available in virtually any FPGA system.

To compile the photon counts, we will use a counter that operates for a given period of time, our sampling duration, and is then reset. Each sampling duration is equivalent to the sampling interval ΔT previously discussed. The integer value of photons in each sampling interval will compose a value in the signal $x[n]$. Notably, each value of $x[n]$ can be used to accumulate a ongoing 'picture' of the Poisson PDF and to estimate the mean noise for a given detection channel.

The sampled photon count data in $x[n]$ is then compared against a photon threshold using a digital comparator operation. This provides the equivalent functionality of a analog signal discriminator, more commonly found in nuclear instrumentation measurements (NIM). The purpose of the comparator is to evaluate the SMD criteria on the basis of intensity, as described in 2.53. While this is the basic premise of detection, it is not sufficient. In the paragraph following 2.53, we describe the probability of a detection event occurring during to random noise fluctuations, in the given example the probability is 1.7 $x10^{-4}$ for an $SNR = 5$. The probability of two, uncorrelated events occurring in succession is further re-

duced. Since a SMD event represented by a single sampling interval ΔT would be a clear violation of the Nyquist condition, it is necessary that several successive sampling intervals must also contain an value for $x[n]$ that is above the photon threshold. This requirement is the same as the 'width' parameter found in analog signal discriminators and can be implemented in our system as a minimum burst duration criterion. This criterion can be evaluated by a simple pattern match that looks for the rising and falling edge of the photon threshold comparator's output. This pattern match is performed with yet a second comparator, the logical output of which indicates a SMD event. This output is used to drive the SSR input to actuate molecule sorting.

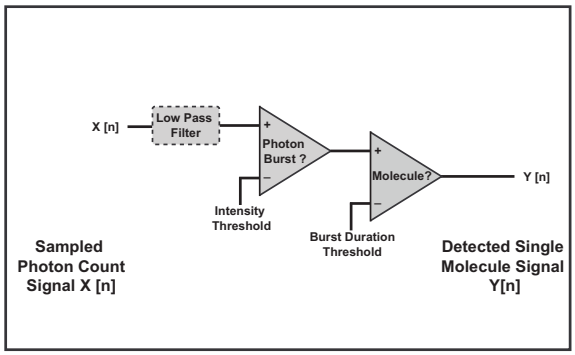

Figure 3.3: Circuit Model for Basic Real-Time Detection (BRTD). A comparator is used to evaluate if a given value of x[n] is above the photon threshold. A second comparator evaluates the duration of the above-threshold signal to ensure it is sufficiently wide to be a single molecule detection event. If both conditions are satisfied a pulse with width equal to the single molecule event is output at y[n]. Note the low-pass filter, shown in a dotted line, is not required for implementation of the BRTD algorithm.

Clock Synchrony, Drift, and Counting Errors To evaluate the accuracy of the BRTD method, the pulses output from the FPGA were compared against the photon data collected in a post-experiment analysis. At first, this was attempted using a parallel connection of the photon-counting hardware correlator

to an FPGA operating with the BRTD algorithm. Humbly confounded by the epic level of disagreement, I realized that each hardware component was operating with an independent system clock. To ensure clock synchrony in the presence of oscillator drift, a master-slave oscillator configuration was implemented wherein the FPGA provided the master clock signal and the time-correlated single photon counter (TCSPC) hardware was slaved to this signal. To maintain near phase-locked operation, the sampling period of the FPGA was set to 50 μs, which caused an undetectable drift of < 2 ns in the TCSPC counting during that period. Here is a short expression for this condition:

$$\Delta T_{FPGA} \leq (\frac{1}{m})(\frac{\Delta T_{TCSPC}}{T_{OSC}}) \tag{3.11}$$

where $\frac{1}{m}$ is the fractional number of wavelengths or cycle errors allowed for phase lock where $m >= 1$, ΔT_{TCSPC} is the sampling rate of 2 ns for the TCSPC detector hardware, T_{OSC} is the stability of the master clock measured in non-dimensional units (i.e. 50 ppm = 50 x 10^{-6}), and ΔT_{FPGA} is the sampling time required to achieve the desired level of phase lock. However, there is a more fundamental difference in the counting of these two hardwares. Unlike the FPGA that counts using a continuously running system clock, the TCSPC hardware operates in time-coordinated sweeps and performs a hardware reset at the end of each sweep. During this hardware reset, or counting deadtime, no counting is performed. On average, the manufacturer specifies an end-of-sweep deadtime of 250 ns, which will occur each 50 μs interval as clocked by the FPGA. If events were equally distributed in time, the counting disagreement would be about 0.5 percent, however, since these events occur stochastically, a group of photon events could be discounted all together.

Digital Signal Filtering Using a discretized signal, I became compelled to consider digital signal processing (DSP) methods, specifically digital filters, toward further reduction of the noise sources during detection and adaptive detection. To this end, there two classes of filters described in DSP literature - the infinite impulse response (IIR) and finite impulse response (FIR) filter. The IIR filters originate from analog circuits because of their impulse response, commonly denoted $h(t)$, support over all time. These filters are commonly realized as band stop, band pass, low-pass, and high-pass filters. However, they can be unstable in their realization due to the possible existence of poles on the right-side of the complex plane. (I'd like to thank former Prof. Hooshang Hemami for sharing a memorable joke on this topic that has always helped me to remember this property.) These poles represent complex frequencies where undamped resonance can occur within the filter causing destabilization. Notably, as it applies to digital filters, IIR implementations are relatively uncommon, because their models are built upon analog circuit equivalents that have more limited versatility. By contrast, FIR filters are commonly found in both analog and digital circuits. The external feedback and finite-duration response of the FIR design ensures stability. In digital implementation, FIR filters afford the designer complete control in shaping magnitude response to achieve optimum signal filtering and are relatively straightforward to implement. The primary downside to these filters is the quantity of computational resources required to perform their operation, however, this is usually not a limiting factor. For these reasons, we will be implementing an FIR design. The greatest downside to digital filtering, in general, is that evaluation on a synchronous clock incurs latency. However, for well-designed filters, this latency can be little as 1 clock cycle.

Improved Event Detection Through Smoothing After performing some initial experiments with the BRTD method, I noticed that some SMD events caused multiple-actuation events by the FPGA. These were the result of SMD events that fluctuated near the threshold during the detection process. In the absence of stochastic fluctuations in fluorescence, we would anticipate the time-resolved shape, or envelope, of a SMD event to be Gaussian from the convolution of a point emitter with a Gaussian profile beam. Since smoothing with a Gaussian was not possible in early complex programmable logic device (CPLD) implementations, I implemented using a fixed-width 5 or 7-bin wide boxcar filter as shown in Figure 3.4.

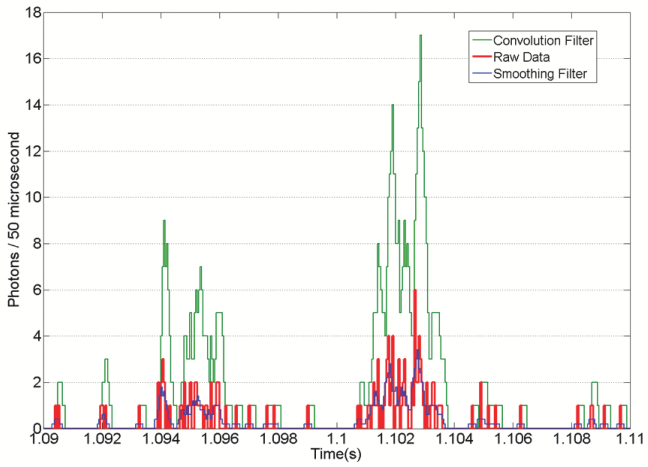

Figure 3.4: Smoothing Filter Implementation. A 7-bin filter was was used to perform smoothing on otherwise difficult to detect single molecule fluorescence. The 'convolution' filter shown is not normalized in magnitude, which allowed it to operate on integer photon counts and output a scaled, integer set of of values. This allowed filter implementation within the hardware constraints of a complex programmable logic device (CPLD).

This method of signal smoothing considerably improved the agreement in SMD and reduced the occupance multiple-actuation events occurring for each SMD event.

Optimum Filter Design Optimum filter design, or matched filter design, is used to maximize the signal to noise ratio (SNR) by identifying the optimum filter shape. In mathematical terms, we can used the generalized model for a signal $x(t)$ previous developed in 2.36 and apply it to a filter with impulse response $h(t)$, and then consider the output $y(t)$ in terms of the SNR. Using the Fourier transform to relate convolution in the time domain to multiplication in the frequency domain as in equation 2.59, one expression for SNR can be:

$$SNR = \frac{|y_s(\omega)|^2}{< |y_n(\omega)|^2 >} = \frac{|h(\omega)\ s(\omega)|^2}{< |h(\omega)\ n(\omega)|^2 >} \tag{3.12}$$

Since the filter $h(t)$ is causal and real-valued in time, it is also Hermitian symmetric, which allows it to be decomposed into $|h(\omega)|^2 = h^\dagger(\omega)\ h^*(\omega)$, a complex conjugate pair. Furthermore, because it is not a stochastic function, it can be removed from within the expectation operator. While a similar Hermitian symmetric operation can be performed on the signal and noise in x(t), the stochastic nature of these components requires they remain within the expectation operator. This allows further expansion of the SNR by removing the filter components from within the expection operator using:

$$< |y_n(\omega)|^2 > =\ h^\dagger(\omega) < |n(\omega)|^2 > h^*(\omega) =\ h^\dagger\ (\omega) R_{nn}\ h^*(\omega) \tag{3.13}$$

where R_{nn} is the autocorrelation of the noise. Ultimately, this decomposition and reorganization of terms can be evaluated using the Cauchy-Schwarz inequality $|\ a^\dagger b^*\ |^2 \leq (a^\dagger a^*)(b^\dagger b^*)$ to arrive upon an expression of the optimum filter.

$$h(\omega) = \alpha R_{nn}^{-1} s^*(\omega) \tag{3.14}$$

$$\alpha = \frac{1}{\sqrt{s^\dagger R_{nn}^{-1} s^*}}, \tag{3.15}$$

It is of little surprise that the optimum filter design that results is essentially the average signal shape for the detected signal itself, by a process of minimizing the noise. In our system, this signal shape is very well approximated by a Gaussian distribution. The characteristic parameters defining this shape can also be well-estimated using a mathematical fit of the autocorrelation function to extract the value of τ when $G(\tau) = 0.5$.

3.3 Experimental Details

3.3.1 Device Fabrication

A 100 mm diameter fused silica substrate (Mark Optics) was used to construct the nanofluidic devices (Mark Optics). The device pattern was defined by projection photolithography and then etched into the substrate by reactive ion processing to form a channel cross-section 500 nm x 250 nm (width by depth) in the constricted region. To access the fluid reservoirs of the device, through-wafer holes were formed using a focused jet of alumina abrasive. The device was cleaned rigorously in a heated, RCA1 standard base bath (6 H_2O : 1 NH_4OH : 1 H_2O_2), to facilitate touch bonding with a 170 μm-thin fused silica substrate that enclosed the fluidic channels. The wafer stack was annealed at 1080 °C to form a permanent bond. Additional details are described elsewhere (14).

3.3.2 Optical Measurement Setup

Optical measurements were performed using an inverted microscope platform (Olympus IX-71). Fluorescence was induced using laser sources emitting at 488 nm and 637 nm (Coherent Corporation) operating at powers of 10 mW and 28 mW, respec-

tively. The collinear beams were elongated using a cylindrical lens (Thorlabs) to create a near-uniform line of illumination. The beam was focused onto the nanofluidic device using a 40x water immersion objective (Olympus). A polychoric mirror and emission filter pair (Chroma) separated the laser excitation and fluorescence emission. Collected fluorescence was chromatically split and then passband filtered at 525/40 nm and 685/40 nm (Semrock). A linear array of multimode optical fibers mounted in a silicon v-groove chip (OZ optics) served as confocal apertures and also delivered the collected fluorescence to single photon counting avalanche photodiodes (Perkin Elmer). Photon counts were assessed using a custom-programmed FPGA (Terasic Technologies) and recorded by two, TCSPC cards (FastComTec P7888).

3.3.3 Real-Time and Post-Experiment Single Molecule Analysis

Real-time photon counting and signal analysis was performed using an Altera Cyclone-III FPGA. The FPGA hardware was operated with an adjustable, 50 μs time-base or 'bin' to achieve 5-10 fold oversampling of each single molecule event, depending on the electrokinetic flow rate. To achieve single molecule detection, photon events were counted during each bin, processed by a digital low-pass filter to smooth noise that could lead to incorrect sorting, and compared against an intensity threshold to identify fluorescence bursts. To eliminate spurious bursts, a two-bin minimum burst duration was enforced. Single molecule events satisfied both thresholds and their detection actuated the sorting trigger. Post-experiment single molecule analysis was performed on the time-resolved photon record file from the TCSPC hardware using a custom Matlab routine. For sorting of multicolor events, real-time analysis using an AND gate evaluated the time-coincidence

of each color event and actuated the sorting trigger when bound molecules were observed. This FPGA trigger was time-correlated with detection events during post-experiment analysis using Matlab.

3.3.4 Electrical Characterization of Sorter Hardware

Operation of the FPGA and high voltage switch were verified using an arbitrary waveform generator (Tektronix AFG 3252) and oscilloscope (Tektronix DPO 3052). Nanofluidic channel resistance and solid-state relay (Vishay) leakage current were measured using a picoammeter with built-in voltage source (Keithley 6487). To measure impulse response, buffer-filled nanofluidic channels were placed in a faraday cage, actuated by time-isolated voltage pulses, and their ion current response was monitored using a low-noise current amplifier (Ithaco 1201) and visualized using an oscilloscope.

3.3.5 DNA and MBD Sample Preparation

Both pUC19 and pML4.2 were grown in dam-/dcm- E.coli (New England Biolabs - C2925). Culture was done in 200mL flasks and plasmids were then purified using a QIAGEN Plasmid Midi Kit. Purified DNAs from pML4.2 and pUC19 were linearized with AscI and EcoRI to generate fragments measuring 2.7 Kb and 15.0 Kb, respectively. The pML4.2 was in-vitro methylated using MsssI and the qualitative degree of methylation was confirmed using HhaI and DdeI restriction digests (Fig. 3.5). DNA staining was performed with TOTO-3 (Invitrogen) at a dye to basepair ratio of 1:5.

The 1xMBD probe was expressed in E. coli, purified, and then labeled using an Alexa-488 amine-reactive dye (Invitrogen A20000) as described [18]. Labeled MBD was purified by size exclusion chromatography using a Superdex 75 resin

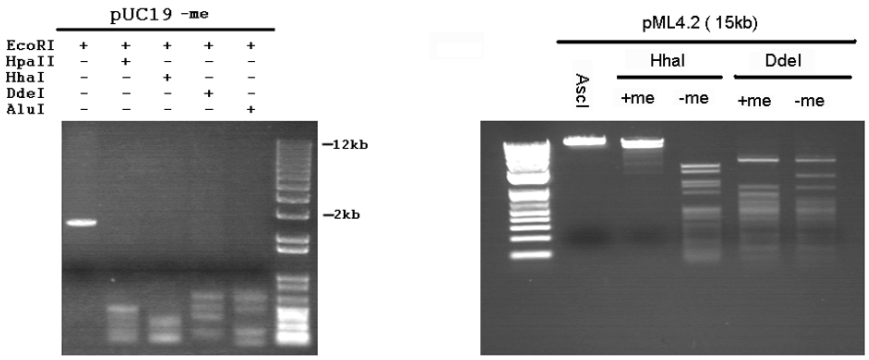

Figure 3.5: Linearized Plasmid Methylation Sensitive Digest.

(GE healthcare) in Phosphate Buffered Saline (PBS) buffer to remove unreacted dye and then confirmed for probe activity.

The MBD-DNA binding reaction was performed in 1x Tris-buffered saline (TBS) at pH 8.0 in 0.5% bovine-serum-albumin and 0.1% Triton X-100. DNA components were dissolved in the binding buffer and then mixed with MBD dissolved in PBS with 50% glycerol. The mixture was covered with aluminum foil and then slow-rotated overnight at 4 °C. All biological samples were diluted into a 'flow buffer', 10mM Tris and 1mM EDTA buffered to pH 8.0 (1x TE buffer, Sigma Alrich) that also contained 0.1% Triton X-100 (Sigma Alrich) and 0.3% polyvinylpyrrolidone (Sigma Alrich), to flow them through the nanofluidic device.

3.3.6 Actuation of Electrokinetic Flow

Each bifurcated nanofluidic channel was filled with flow buffer and then conditioned for 1 hour under electrokinetic flow. After conditioning, the buffer was collected to establish a baseline for device content (i.e. a blank for qPCR analysis). A biological sample was then loaded into the device input and driven at +50 V toward

the default output during a 15 minute loading period. A baseline measurement of the molecule flow was performed during the final minutes of the loading period to evaluate transit time between input and output for programming the sort trigger duration, to observe any misdirected molecules and correct any voltage drive imbalance, and to measure the photon noise floor for programming the intensity threshold within the FGPA. With these conditions set, molecule sorting was then performed. At the conclusion of a sorting experiment, sample in the input reservoir was recovered and the reservoir was rinsed 6 times with flow buffer to remove residual sample. Electrokinetic drive was then applied and molecules were sorted until the input tract of the device was clear. Flow was then directed to the sorted output to recover molecules for analysis by qPCR.

3.3.7 Sample Recovery and qPCR Amplification

Samples were extracted from the fluid reservoir by pipette, transferred into low-adhesion microcentrifuge tubes, and stored at -20 °C. qPCR amplification was performed on an ABI 7500 system using SybrGreen mastermix (Applied Biosystems) with primers specific for either pUC19 (F-,R-) or pML4.2 (F-,R-). Standard curves were made from purified plasmid DNA and used to quantify sorted material. qPCR measurements were performed in triplicate using 1 μL of material collected from the sorter placed into a reaction volume of 20 μL. This value was compared with in-situ measurement of the total molecules sorted to calculate molecule

3.4 Results and Discussion

3.4.1 A Fluorescence-Actuated Single Molecule Sorter

We designed our nanofluidic sorter to operate using materials prepared by established methods to ensure its integration within an epigenetic analysis workflow. For this design, we implemented a process (Fig. 3.6), wherein fluorescently-labeled probes, such as antibodies or proteins, are bound to epigenetic modifications located on histone proteins or DNA. This mixture is then loaded into our nanofluidic device to identify these molecules and their corresponding modifications by fluorescence color signature. Each molecule with a color signature that matches the criteria for collection is then sorted during a brief actuation, or pulse, that redirects flow to the sorted output. The flow direction returns to the default output following a sort event. Sorted molecules are then collected for subsequent qPCR analysis.

In order to develop a sorting device, we modified the nanofluidic device previously described [18] in several fundamental ways. First, we added a bifurcation to create two outflow paths for molecules and then adapted the optics to detect input molecules flowing towards the bifurcation and output molecules flowing away from the bifurcation in both paths; second, we developed computational hardware to evaluate the fluorescence signal from each input molecule in real-time and then actuate sorting; third, we developed a circuit to rapidly direct the flow of molecules to either outflow path during sorting and optimized sorting accuracy by tuning the circuit parameters. These modifications are discussed in the following paragraphs.

To perform in-situ optimization of sorting performance, we developed a method to simultaneously monitor multiple nanofluidic paths for tracking each molecule within the device. This detection method utilizes a linear array of confocal aper-

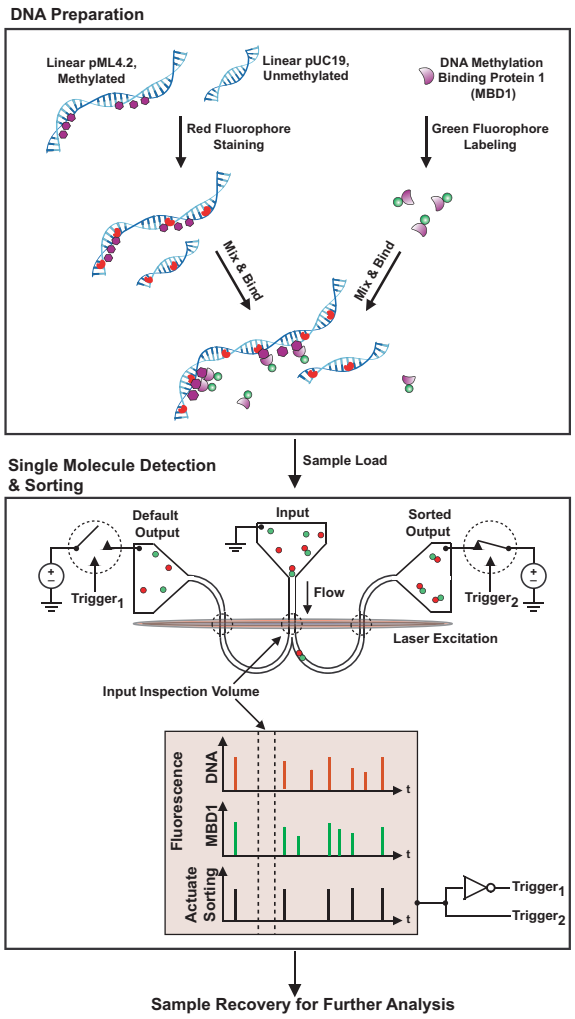

Figure 3.6: An Epigenetic Analysis Workflow Using Fluorescence-Activated, Single Molecule Sorting. (Top) DNA Preparation. Linearized DNA plasmids, unmethylated pUC19 and methylated pML4.2, were fluorescently labeled with a red stain and then mixed with green-labeled methyl binding domain protein-1 (MBD1) during a bulk reaction. (Middle) Single Molecule Detection and Sorting. Samples were loaded into the input of a bifurcated nanofluidic device. An applied voltage flowed molecules through the device. As each fluorescently labeled molecule passed through the input inspection volume, its fluorescence signature was detected and then evaluated in real-time. In this panel, an MBD1 bound to methylated DNA was identified by its two-color fluorescence signature. This signature actuated a sorting trigger and a pair of opposing switches to direct the molecule toward the sorted output. After a molecule was delivered to the sorted output, the flow was redirected to the default output. (Bottom) Material in the sorted output was recovered by pipette and quantified by qPCR analysis.

tures whose spacing is geometrically-matched to the branches of the m-shaped nanofluidic channel (Fig. 3.6 and 3.8). As fluorescence is emitted from each molecule, it is imaged within the inspection volume formed by the overlap of one confocal aperture to a region of nanofluidic channel. The confocal apertures are formed by a linear array of optical fibers (Fig. 3.8 and 3.7), which are aligned simultaneously to all branches of the nanofluidic channel. To ensure the fluorescence from a given inspection volume does not affect those adjacent, we measured a low optical cross-talk, -13dB, for apertures spaced 500 μm apart (Fig. 3.7). We evaluated the parallel fluorescence detection and tracking accuracy of this method by monitoring the input and outputs of a bifurcated nanofluidic device during flow of a fluorescently labeled plasmid, pML4.2. To track uniquely one molecule at a time within the path between input and output, detection was performed at a 50pM sample concentration; we calculate a $< 2.6 \times 10^{-3}$ probability of multiple molecules co-occupying this path. In this experiment, 99.7% of all molecules detected at the input were tracked to the output. The molecules not tracked had fluctuated above or below the detection threshold, but were distinct from noise, suggesting slight photobleaching during transit and differences in beam illumination uniformity. Therefore, our design demonstrated facile alignment and simultaneous detection of single molecule fluorescence from multiple fluidic channels to enable in-situ optimization of sorting performance.

Real-time analysis is required for automated, fluorescence-activated sorting to be practical over a wide-range of molecule flow speeds. To perform real-time analysis, we selected a field programmable gate array (FPGA) for its capabilities in digital signal processing (DSP) and facile integration with existing avalanche photodiode (APD) and time-correlated single photon counting (TCSPC) hardware (Fig. 3.8). The process of real-time detection within the FPGA began with digital elec-

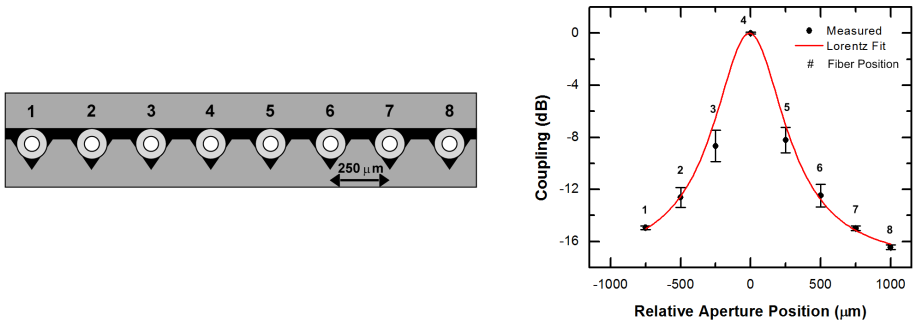

Figure 3.7: Linear Array of Confocal Apertures. (Left) Silicon v-groove array used to secure optical fibers at a 250 μm spacing. (Right) Laser induced fluorescence is aimed at fiber four in an array of eight fibers. Fluorescence collected by each fiber within the array was measured (N=5 per position, $\pm$1 S.E.M.). The optical coupling to the apertures was well-described by a Lorentz function fit (R^2=0.999). A spacing of 500 μm between fibers was used during in-situ measurements of molecule sorting. At a spacing of 500 μm, the coupling of light to adjacent confocal apertures is approximately -13 dB and was used during in-situ measurements of molecule sorting.

trical signals representative of individual photons measured by the APDs. These signals were counted, low-pass filtered, and then compared against both a burst intensity and duration threshold to identify a single molecule (Fig. 3.8). We found low pass filtering necessary to smooth and reduce noise fluctuations around the intensity threshold that otherwise caused some molecules to be multiple-counted and actuated for sorting. The low pass filter designs we implemented, a boxcar and a Gaussian-shaped filter, were used during subsequent DNA-size and methylation sorting experiments. While DSP with these filters introduced detection delay, the time necessary to analyze single molecule fluorescence scaled proportionally with flow rate and often occurred in <1 ms. (Fig. 3.8). To verify the accuracy of our real-time detection method, we flowed fluorescently labeled pML4.2 molecules because of their high (200) signal to noise ratio (SNR) during detection and then compared a time-resolved record of their fluorescence against real-time, FPGA-detected events. We measured > 98% agreement between real-time and post-experiment detection methods using the same analysis conditions. Since these detection methods operated in clock-synchrony and using similar algorithms, we attribute differences in detection primarily to the dead-time specification of TC-SPC hardware as compared to the FPGA. In summary, our FPGA-based analysis has shown highly accurate, real-time single molecule detection.

For sorting individual molecules into the nanofluidic output paths, we used electrokinetic flow because it can be actuated by rapidly-switched, externally-applied voltages. To exert precise flow control, we began with an electric circuit model for the nanofluidic device that used channel geometry and buffer ion concentration to describe the equivalent channel resistance and double layer capacitance, respectively, and then characterized the electrical operation of the nanofluidic device. The electrical resistance of the nanofluidic device filled with 1x Tris-EDTA (1x

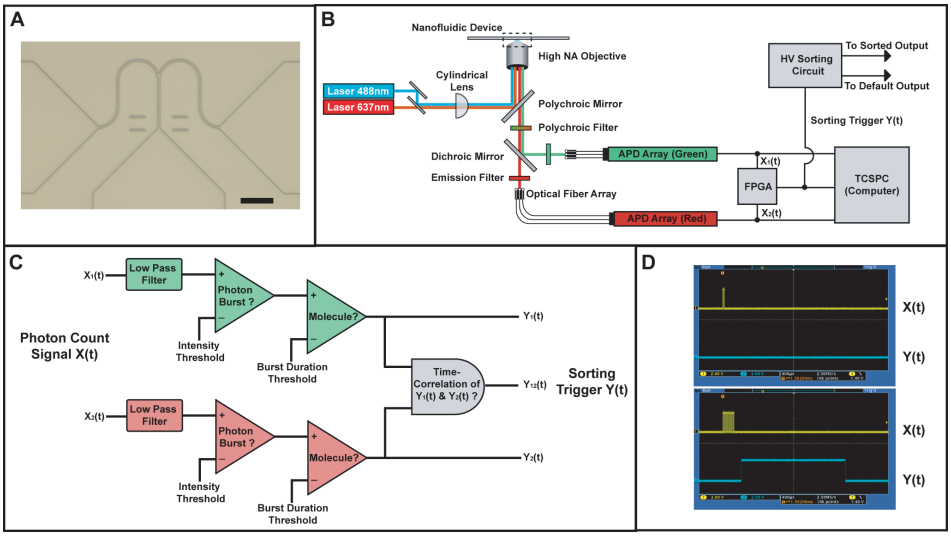

Figure 3.8: Constructing a Fluorescence-Actuated, Single Molecule Sorter. (A) A brightfield photomicrograph of a bifurcated nanofluidic channel (cross-section 500 nm wide by 250 nm deep) for sorting molecules. The scale bar is 10 μm. (B) The nanofluidic device was mounted onto a confocal fluorescence microscope and illuminated by two overlapped lasers to simultaneously excite molecule fluorescence. Single molecule fluorescence was imaged using an optical fiber array connected to single photon counting avalanche photodiodes (APDs). A field programmable gate array (FPGA) performed real-time fluorescence analysis at the input inspection volume and triggered a high voltage (HV) sorting circuit to direct the electrokinetic flow of a molecule to the sorted or default output. All detection events were recorded using time-correlated single photon counting (TCSPC) hardware operated in synchrony with the FPGA. (C) An FPGA-based electrical circuit was used to evaluate photon count signals, $X_1(t)$ and $X_2(t)$, each reporting a different fluorescence color. Detection noise was reduced using a digital low pass filter. Photon detection events were compared against an intensity threshold and a minimum time duration threshold to identify single molecules, which actuated the trigger signal $Y_1(t)$ or $Y_2(t)$. Molecules bound with multiple fluorescence colors caused time-correlation of $Y_1(t)$ and $Y_2(t)$, evaluated by a logical AND gate, which output $Y_{12}(t)$. (D) An oscilloscope photomicrograph illustrates FPGA operation using a 5-pulse train and a 25-pulse train, shown as X(t), to simulate a photon burst. Only the simulated burst in the bottom panel exceeded the 5 pulse/50μs and 100 μs threshold and a 2 ms sorting trigger.

TE) buffer measured 3.5 ± 0.1 GΩ (Fig. 3.9), which indicated that relays with low off-state leakage current were necessary to electrically disconnect the device during flow switching. We also found that external voltage balancing minimized fabrication-induced variations in channel geometry and further sculpted the electric field at the bifurcation. These adjustments lead to symmetric sorter operation and a misdirection rate of approximately $< 10^{-3}$ molecules when operated in a fixed voltage configuration. We then assessed electrokinetic flow response to a voltage impulse to mimic sorting actuation. The impulse response of the nanofluidic demonstrated an upper limit of 10 kHz on switching speed, based upon a transient settling time of approximately 50μs (Fig. 3.10). Switching at this frequency could allow sorting at rates up to 100,000 molecules/min using the present device geometry.

3.4.2 Sorting for Molecule Enrichment and Recovery

A 50pM mixture of DNA molecules was loaded into the nanofluidic device to evaluate molecule counting and tracking during a single-color sorting experiment to size-separate the molecules. The mixture was composed of linearized pUC19 (2.7 kbp) and pML4.2 (15.2 kbp) DNA plasmids intercalated with TOTO-3. The approximate 5 fold difference in molecule size was observed proportionally in fluorescence intensity [25] and allowed molecule identification for sorting. A threshold value of 50 photons/50 μs distinguished the DNA molecule sizes (Fig. 3.11) and was programmed into the FGPA to identify and actuate sorting of the pML4.2 molecules. A time-resolved record of this molecule sorting experiment (Fig. 3.12) illustrated the bursts of fluorescence from pML4.2 matched to the sorting actuation trigger. This record confirmed successful sorting by in-situ tracking of each above-threshold molecule from input to sorted output. A transit time of 4.3 ± 0.3 ms

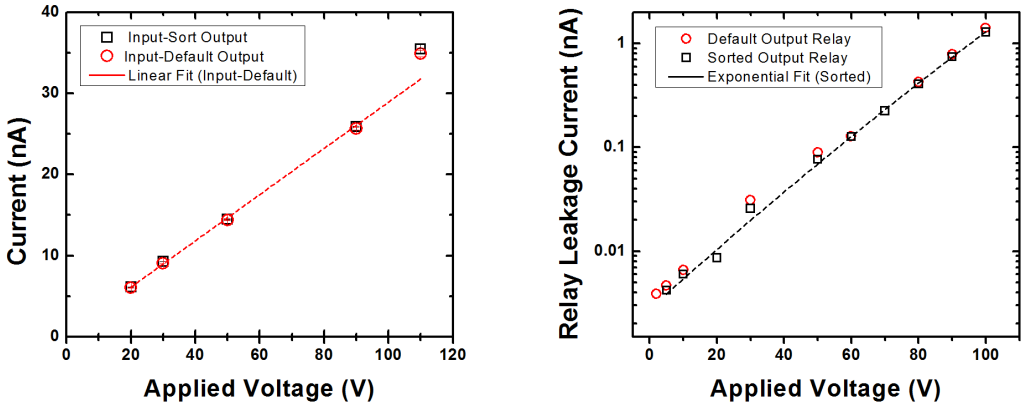

Figure 3.9: DC Electrical Characterization. (LEFT) Nanofluidic Channel Resistance. Channel resistance was measured from the input to each output reservoir when filled with 1x TE buffer (N=3 current measurements per drive voltage, error bars ±1 S.E.M.). A linear fit (R^2=0.995 of these points reveals a slope that corresponds to a channel resistance of 3.5±0.1 GΩ ±1 S.D). (RIGHT) High Voltage Relay Leakage Current. The electrical properties of switching relays were measured independently to verify matched operation. An exponential fit (R^2=0.999) of the leakage current was determined, which motivated operation of the relays at 50 V and below to achieve a 190:1 current isolation for switching.

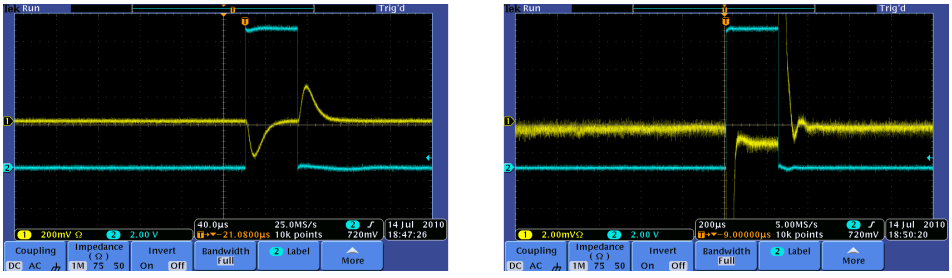

Figure 3.10: Impulse response of nanofluidic channel. A voltage impulse from a function generator (blue trace) was applied to the input and one output of the nanofluidic channel. Using a current preamplifier, the ion current response within the device is monitored (yellow trace) and its time-dependent response is recorded. We observed an RC time constant of approximately 50 μs before the steady state response was achieved.

through the bifurcated region was calculated by fitting a time-correlated measurement of the delay between molecule observations (Fig. 3.11). These measurements successfully demonstrated real-time detection and in-situ tracking of individual DNA molecules during fluorescence-activated sorting at >500 molecules/min.

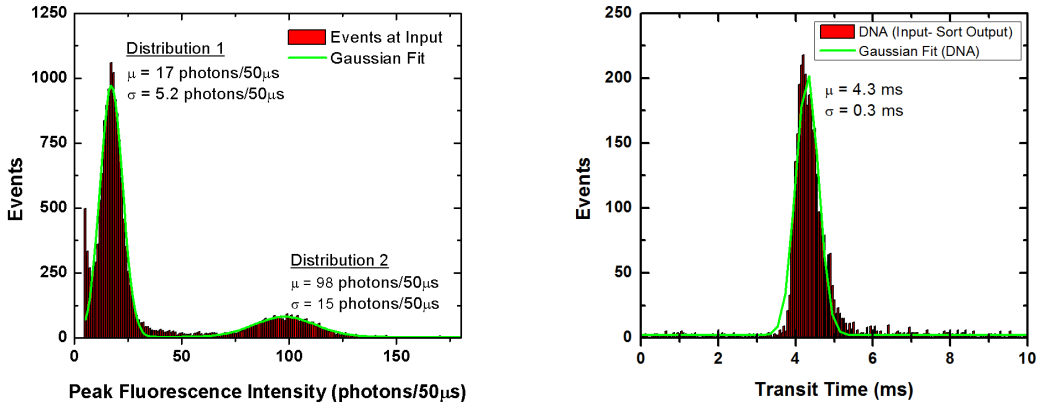

Figure 3.11: Parameters to Actuate Sorting (LEFT) Determination of the intensity threshold for sorting. This histogram illustrates the peak fluorescence intensity of pUC19 and pML4.2 molecules, distributions 1 and 2 respectively, observed at the input to a sorting device. The Poisson distributed noise for this system was 0.44 photons/50μs, leading to a signal to noise ratio of 38 and 220 for the pUC19 and pML4.2 fragments, respectively. Separation of the two populations, based upon post-processing analysis, would be optimally balanced using an burst intensity of 37 photons/50μs, which occurs 4σ from the mean of each distribution. Given limited counting statistics to estimate the optimum threshold at the beginning of our experiment, we chose a burst intensity threshold of 50 photons/50μs and programmed it into the FPGA for sorting.(RIGHT) Time-correlated detection of molecules for sorting actuation. Based upon a Gaussian fit (R^2=0.966), molecules were observed to transit between input and output within 4.3 ± 0.3 ms ($\pm$1 S.D.).

We proceeded to investigate sorting accuracy by measuring the rate of false positive and negative sorting events. These figures of merit determine the limit of molecule enrichment that can be attained by sorting. Our sorting device was

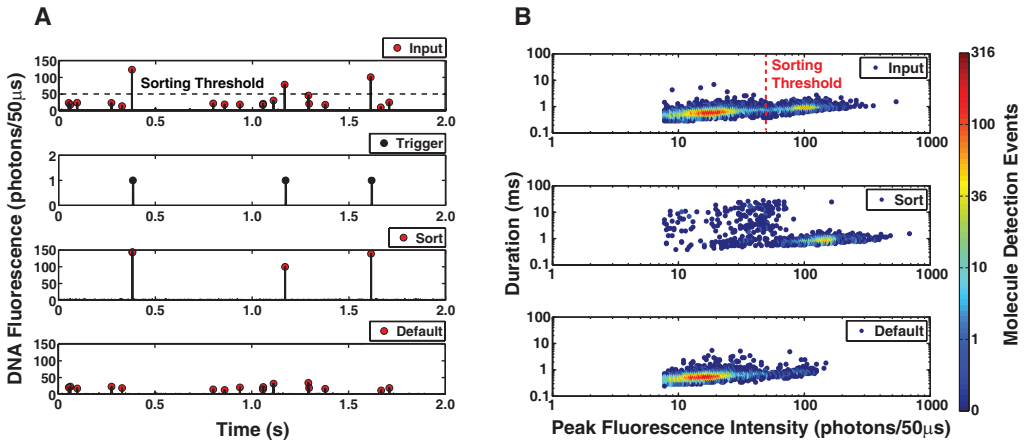

Figure 3.12: Optimization of Molecule Sorting Efficiency. A 1:4 molar ratio mixture of red-intercalated pML4.2 (15.2 Kb) and pUC19 (2.7 Kb) DNA was loaded into the nanofluidic device and sorted on differences in fluorescence intensity to collect pML4.2. (A) A time-resolved record of single molecule events, black pulses marked with a red dot, illustrates 2 s from a 30 min sorting experiment. At the nanofluidic channel input, a molecule with fluorescence >50 photons/50 μs actuated the sorting trigger to direct pML4.2 molecules to the sorted output, while pUC19 molecules were directed to the default output. Sorting performance was optimized by tracking each molecule's trajectory in-situ to either of the output inspection volumes and then adjusting electrical actuation parameters to improve sorting accuracy. (B) The nanofluidic sorter evaluated a mixture of 15,848 molecules at the input and sorted 3,394 pML4.2 molecules to the sort output. At the device output inspection volumes, in-situ measurements revealed a false positive rate of $1.9 \pm 0.1\%$ (± 1 S.D.) and 49 ± 3 (± 1 S.D.) fold enrichment of pML4.2 in single step.

configured to collect the pML4.2 molecules from mixtures with pUC19 at molar ratios of 1:4 and 1:12, respectively. To allow for sufficient sampling of false positive and negative events, over 15,000 molecules were observed in both experiments. False negative events, defined as input pML4.2 molecules directed to the default output, were present as $8.2 \pm 0.5\%$ and $3.4 \pm 0.4\%$ of all pML4.2 molecules for the 1:4 and 1:12 mixtures, respectively. This false negative rate was attributed to molecules not identified or sorted by the FPGA. False positive events, pUC19 molecules directed to the sorted output, are significant for the purpose of maximizing enrichment purity. Using bivariate analysis with a scatter plot (Fig. 3.12), we categorized false positive sorting events as either 'co-occupant' or 'uncontrolled' molecules. Co-occupant molecules are a consequence of the Poisson-distributed arrival of two or more molecules in the inspection volume at the same time, which can cause a single trigger actuation to direct multiple molecules to the sorted output. By contrast, uncontrolled molecules migrate to the sorted output without actuation and exhibit widely varying, 2-20 ms, burst durations. Since symmetric operation of the device is calibrated at the start of an experiment, uncontrolled molecules occurred as the result of ion concentration effects and fouling of the channel surface that accumulated over time and led to slightly asymmetric operation. Together, these sources of false positive events occurred as $1.9 \pm 0.1\%$ and $1.0 \pm 0.1\%$ of all pUC19 molecules for the 1:4 and 1:12 mixtures, respectively. This translates into a pML4.2 enrichment of 49 ± 3 and 88 ± 5 fold in a single sorting step. Sorted material was then recovered and analyzed by qPCR, which confirmed the enrichment of pML4.2 observed in-situ and demonstrated successful recovery of a sample enriched by automated sorting. The levels of enrichment measured in-situ are commensurate with other fluorescence-activated sorting methods [20, 26, 27], presently limited to the study of cells and large particles.

3.4.3 Application of Sorting to DNA Methylation Analysis

To demonstrate our single molecule sorter for epigenetic analysis, we proceeded to develop its capability for identifying DNA methylation using two-color fluorescence detection. Similar to the experiments described above, we generated linearized pUC19 and pML4.2 plasmids from methylation deficient hosts, but then in-vitro methylated pML4.2 to form a mixture of methylated and unmethylated DNA. Both DNA species were red-labeled with TOTO-3 and then mixed with green-labeled MBD1. MBD1 was used for its ability to bind methylcytosines on full-duplex DNA, the native configuration of DNA in chromatin [24]. We then analyzed the fluorescence of individual molecules within a mixture of unmethylated pUC19: methylated pML4.2: MBD1, prepared at a 2.8:1:200 molar ratio. The FPGA identified input molecules with a two-color fluorescence signature as MBD1 bound to methylated DNA (MBD1-DNA) and directed these molecules to the sorted output. Two-color fluorescence detection was achieved by reconfiguring the FPGA design with Gaussian filter coefficients and evaluating the outputs from multiple copies of the design using a logical AND gate (Fig. 3.8); and co-propagating a second laser emitting at 488nm with the existing 640nm laser (Fig. 3.8). Proper operation of the FPGA for multi-color detection was verified during a separate experiment. Using independent thresholds of 3 and 6 photons/50 μs to identify MBD1 and DNA molecules, our device identified and sorted MBD1-DNA molecules (Fig. 3.13).

To investigate MBD1 binding specificity, we characterized the molecules from a 20 minute sorting experiment (Fig. 3.13) according to their two-color status and then DNA fluorescence intensity. This post-experiment analysis measured 297 MBD1-DNA events at the device input, composed of 27 unmethylated pUC19 and 270 methylated pML4.2 molecules. We then verified genuine detection of MBD1-

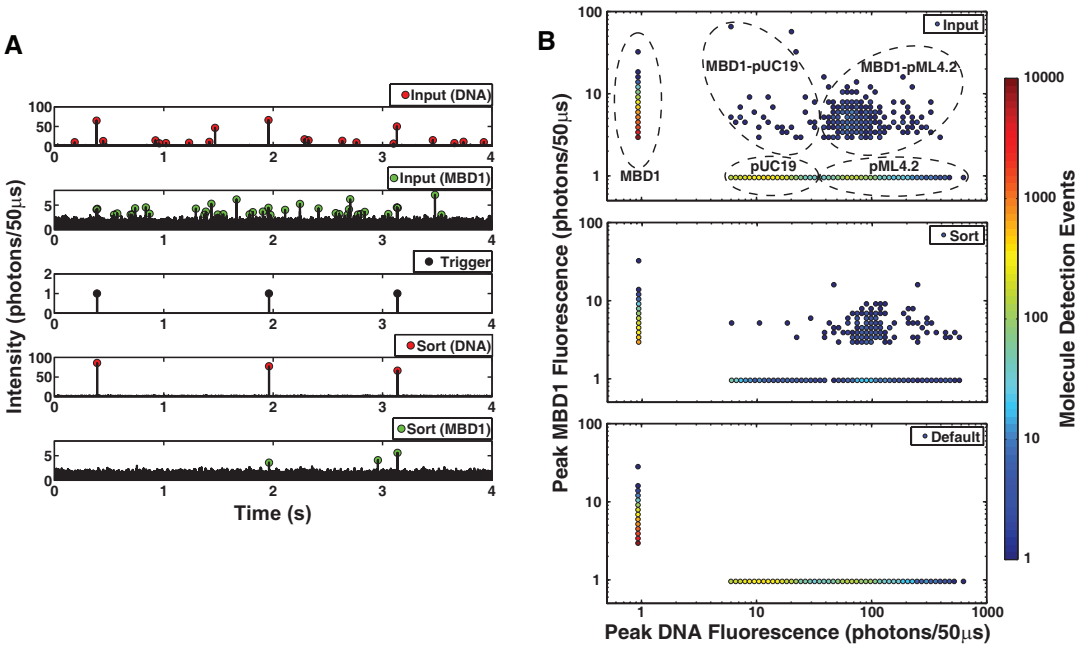

Figure 3.13: Single Molecule Detection and Sorting of Methylated DNA. DNA methylation state was identified using a green-labeled methyl binding domain-1 (MBD1) protein incubated in a mixture of red-labeled DNAs including unmethylated-pUC19 and methylated-pML4.2. Methylation-specific binding was confirmed by two-color fluorescence identification, which actuated sorting collection of bound MBD1-DNA complexes from the original mixture during a 20 minute sorting experiment. (A) This 4 s, time-resolved record illustrates three, two-color molecules identified by the FPGA trigger at the device input. After sorting, the fluorescence from two of the three MBD1 molecules remained paired with DNA, while the third had fluctuated below the intensity threshold. (B) A total of 5723 DNA molecules were analyzed at the device input during this experiment and 297 MBD1-DNA events were identified in this analysis. These MBD1-DNA events were composed of 27 MBD1-pUC19 and 270 MBD1-pML4.2, which demonstrated specific binding of MBD1 to methylated pML4.2 molecules. Unbound molecules were plotted along fluorescence = 1 photon/50 μs to accommodate logarithmic plotting. In-situ molecule tracking demonstrated a false positive rate of $5.6 \pm 0.4\%$ (± 1 S.D.) and 3.5 ± 0.3 (± 1 S.D.) fold enrichment of methylated pML4.2 at the sorted output.

DNA events using a time coincidence histogram analysis and measured 294 ± 21 molecules above a background of randomly-correlated, two-color detection events. These results confirm that MBD1 was specifically bound to methylated DNA.

In-situ fluorescence detection was used to evaluate sorting accuracy by tracking molecules from device input to output. During the 20 minute sorting experiment (Fig. 3.13), all 5723 DNA molecules entering the device input were analyzed and 420 MBD1-DNA molecules were identified and directed toward the sorted output by the FPGA. In our post-experiment analysis, only 297 of the 420 events were identified as MBD1-DNA due to the low SNR (<20) of MBD1 that accentuated photon counting hardware differences. The fluctuations and low-intensity of green fluorescence from MBD1, indicative of unbound or singly bound MBD1 to pML4.2, limited our ability to track MBD1-DNA complexes. Therefore, we used DNA fluorescence to successfully track over 90% of all DNA molecules from input to output. From DNA tracking measurements, we evaluated the false negative and false positive sorting rates, respectively $81 \pm 3\%$ and $5.6 \pm 0.4\%$, for this experiment. The high false negative sorting rate was the result of the low concentration of MBD1 and pML4.2 in the analyte, and the high K_D value for their binding, which resulted in a low concentration of the complex at equilibrium. Based upon experimental observations of MBD1-DNA binding at the device input, we calculate MBD1 binding to an average of 0.15 of 737 methylcytosine sites on pML4.2; this result corroborates with our theoretical estimate for MBD1 binding to an average of 0.95 of 737 methylcytosine sites on pML4.2, given experimental conditions and a 3 μM K_D [24]. These observations emphasize the need for improved detection through enhanced binding conditions. By contrast, the low false positive rate indicates control over the molecule sorting process, yielding 3.5 ± 0.3 fold enrichment of methylated pML4.2 with a 39% background of pUC19 at the sorted output.

Our results for sorting DNA plasmids compare well with existing literature for immunoprecipitation reactions, which report typical 2-8 fold enrichment levels [3, 28], binding-limited methylation detection [28], and collection of 60-99% background DNA [29].

3.5 Summary and Conclusions

We have described the development of a nanofluidic device that can be used as part of an epigenetic analysis workflow. This device provides nanofluidic confinement to isolate individual molecules for color-multiplexed detection and to sort these molecules by voltage-actuated flow. These attributes have enabled us to perform real-time fluorescence detection and automated sorting on individual molecules based upon their fluorescence signature. We have optimized the sorting operation using time-correlated in-situ detection to achieve up to 98% accuracy in sorting; and confirmed sample recovery of sorted material by qPCR to suggest opportunities for post-sorting sample analysis by microarray or DNA sequencing methods. We have applied this technology to detect and sort methylated DNA molecules bound with MBD1 protein from within 11 fg of total genetic material.

We envision several goals for continued development of this device. The first goal is to improve detection efficiency by using different methylcytosine binding probes or modified conditions that enhance MBD1 binding to DNA. This could be achieved using high affinity antibody probes with nanomolar K_D values to enhance binding to methylated ssDNA or chemical cross-linking at high sample concentrations to enhance MBD1 binding to dsDNA [30, 31]. Yet another goal is to increase sample throughput toward studying DNA or chromatin sources at a whole genome scale. Throughput may be increased in several ways including: disabling the in-situ single molecule tracking used in this work, to increase input

sample concentration and throughput by 20-fold; removing unbound fluorescent probes, to pre-concentrate the collection of informative molecules; and scaling the system, to include a collection of devices operated in parallel and monitored using alternative fluorescence readout methods [32]. A third goal could explore workflow integration by joining the single molecule sorter with recent advances in cell processing [12, 27, 33, 34]. The sorter operates using small quantities of input material, a feature that pairs well with targeted extraction of genetic material from specific and limited (1-100) cell populations. Such integration could provide an alternative to the off-chip material preparation steps used in this work and lead to more efficient sample workflows. The fourth goal would further develop methods for post-sorting material extraction to allow library preparation and downstream microarray or deep sequencing by adapting single cell sequencing methods [35, 36]. These goals for development establish abundant opportunity to explore the application of single molecule sorting for epigenomic analysis and a variety of molecule separation workflows.

References

[1] P. A. Jones and S. B. Baylin, "The fundamental role of epigenetic events in cancer," *Nature Reviews Genetics*, vol. 3, no. 6, pp. 415–428, 2002.

[2] K. D. Robertson, "Dna methylation and human disease," *Nature Reviews Genetics*, vol. 6, no. 8, pp. 597–610, 2005.

[3] T. I. Lee, S. E. Johnstone, and R. A. Young, "Chromatin immunoprecipitation and microarray-based analysis of protein location," *Nature Protocols*, vol. 1, no. 2, pp. 729–748, 2006.

[4] B. E. Bernstein, T. S. Mikkelsen, X. H. Xie, M. Kamal, D. J. Huebert, J. Cuff, B. Fry, A. Meissner, M. Wernig, K. Plath, R. Jaenisch, A. Wagschal, R. Feil, S. L. Schreiber, and E. S. Lander, "A bivalent chromatin structure marks key developmental genes in embryonic stem cells," *Cell*, vol. 125, no. 2, pp. 315–326, 2006.

[5] S. J. Clark, J. Harrison, C. L. Paul, and M. Frommer, "High-sensitivity mapping of methylated cytosines," *Nucleic Acids Research*, vol. 22, no. 15, pp. 2990–2997, 1994.

[6] S. J. Clark, A. Statham, C. Stirzaker, P. L. Molloy, and M. Frommer, "Dna methylation: Bisulphite modification and analysis," *Nature Protocols*, vol. 1, no. 5, pp. 2353–2364, 2006.

[7] Z. G. Xiong and P. W. Laird, "Cobra: A sensitive and quantitative dna methylation assay," *Nucleic Acids Research*, vol. 25, no. 12, pp. 2532–2534, 1997.

[8] Y. Li and T. O. Tollefsbol, *Combined Chromatin Immunoprecipitation and Bisulfite Methylation Sequencing Analysis Epigenetics Protocols*, vol. 791 of *Methods in Molecular Biology*, pp. 239–251. Humana Press, 2011.

[9] A. R. Wu, J. B. Hiatt, R. Lu, J. L. Attema, N. A. Lobo, I. L. Weissman, M. F. Clarke, and S. R. Quake, "Automated microfluidic chromatin immunoprecipitation from 2,000 cells," *Lab On A Chip*, vol. 9, no. 10, pp. 1365–1370, 2009.

[10] B. A. Flusberg, D. R. Webster, J. H. Lee, K. J. Travers, E. C. Olivares, T. A. Clark, J. Korlach, and S. W. Turner, "Direct detection of dna methylation during single-molecule, real-time sequencing," *Nature Methods*, vol. 7, no. 6, pp. 461–U72, 2010.

[11] P. W. Laird, "Principles and challenges of genome-wide dna methylation analysis," *Nature Reviews Genetics*, vol. 11, no. 3, pp. 191–203, 2010.

[12] A. K. White, M. VanInsberghe, O. I. Petriv, M. Hamidi, D. Sikorski, M. A. Marra, J. Piret, S. Aparicio, and C. L. Hansen, "High-throughput microfluidic single-cell rt-qpcr," *Proceedings Of The National Academy Of Sciences Of The United States Of America*, vol. 108, no. 34, pp. 13999–14004, 2011.

[13] T. E. McKnight, C. T. Culbertson, S. C. Jacobson, and J. M. Ramsey, "Electroosmotically induced hydraulic pumping with integrated electrodes on microfluidic devices," *Analytical Chemistry*, vol. 73, no. 16, pp. 4045–4049, 2001.

[14] J. G. Kralj, M. T. W. Lis, M. A. Schmidt, and K. F. Jensen, "Continuous dielectrophoretic size-based particle sorting," *Analytical Chemistry*, vol. 78, no. 14, pp. 5019–5025, 2006.

[15] L. Wang, L. A. Flanagan, N. L. Jeon, E. Monuki, and A. P. Lee, "Dielectrophoresis switching with vertical sidewall electrodes for microfluidic flow cytometry," *Lab On A Chip*, vol. 7, no. 9, pp. 1114–1120, 2007.

[16] V. Studer, A. Pepin, Y. Chen, and A. Ajdari, "An integrated ac electrokinetic pump in a microfluidic loop for fast and tunable flow control," *Analyst*, vol. 129, no. 10, pp. 944–949, 2004.

[17] T. Thorsen, S. J. Maerkl, and S. R. Quake, "Microfluidic large-scale integration," *Science*, vol. 298, no. 5593, pp. 580–584, 2002.

[18] B. R. Cipriany, R. Q. Zhao, P. J. Murphy, S. L. Levy, C. P. Tan, H. G. Craighead, and P. D. Soloway, "Single molecule epigenetic analysis in a nanofluidic channel," *Analytical Chemistry*, vol. 82, no. 6, pp. 2480–2487, 2010.

[19] P. S. Dittrich and P. Schwille, "An integrated microfluidic system for reaction, high-sensitivity detection, and sorting of fluorescent cells and particles," *Analytical Chemistry*, vol. 75, no. 21, pp. 5767–5774, 2003.

[20] A. Y. Fu, C. Spence, A. Scherer, F. H. Arnold, and S. R. Quake, "A microfabricated fluorescence-activated cell sorter," *Nature Biotechnology*, vol. 17, no. 11, pp. 1109–1111, 1999.

[21] J. C. Baret, O. J. Miller, V. Taly, M. Ryckelynck, A. El-Harrak, L. Frenz, C. Rick, M. L. Samuels, J. B. Hutchison, J. J. Agresti, D. R. Link, D. A. Weitz, and A. D. Griffiths, "Fluorescence-activated droplet sorting (fads): efficient

microfluidic cell sorting based on enzymatic activity," *Lab On A Chip*, vol. 9, no. 13, pp. 1850–1858, 2009.

[22] C. Claudet, D. Angelov, P. Bouvet, S. Dimitrov, and J. Bednar, "Histone octamer instability under single molecule experiment conditions," *Journal Of Biological Chemistry*, vol. 280, no. 20, pp. 19958–19965, 2005.

[23] T. A. Hagerman, Q. Fu, B. Molinie, J. Denvir, S. Lindsay, and P. T. Georgel, "Chromatin stability at low concentration depends on histone octamer saturation levels," *Biophysical Journal*, vol. 96, no. 5, pp. 1944–1951, 2009.

[24] H. F. Jorgensen, K. Adie, P. Chaubert, and A. P. Bird, "Engineering a high-affinity methyl-cpg-binding protein," *Nucleic Acids Research*, vol. 34, no. 13, 2006.

[25] M. Foquet, J. Korlach, W. Zipfel, W. W. Webb, and H. G. Craighead, "Dna fragment sizing by single molecule detection in submicrometer-sized closed fluidic channels," *Analytical Chemistry*, vol. 74, no. 6, pp. 1415–1422, 2002.

[26] S. H. Cho, J. M. Godin, C. H. Chen, W. Qiao, H. Lee, and Y. H. Lo, "Review article: Recent advancements in optofluidic flow cytometer," *Biomicrofluidics*, vol. 4, no. 4, 2010.

[27] E. Brouzes, M. Medkova, N. Savenelli, D. Marran, M. Twardowski, J. B. Hutchison, J. M. Rothberg, D. R. Link, N. Perrimon, and M. L. Samuels, "Droplet microfluidic technology for single-cell high-throughput screening," *Proceedings Of The National Academy Of Sciences Of The United States Of America*, vol. 106, no. 34, pp. 14195–14200, 2009.

[28] I. Keshet, Y. Schlesinger, S. Farkash, E. Rand, M. Hecht, E. Segal, E. Pikarski, R. A. Young, A. Niveleau, H. Cedar, and I. Simon, "Evidence for an instructive mechanism of de novo methylation in cancer cells," *Nature Genetics*, vol. 38, no. 2, pp. 149–153, 2006.

[29] S. Pepke, B. Wold, and A. Mortazavi, "Computation for chip-seq and rna-seq studies," *Nature Methods*, vol. 6, no. 11, pp. S22–S32, 2009.

[30] L. Schmiedeberg, P. Skene, A. Deaton, and A. Bird, "A temporal threshold for formaldehyde crosslinking and fixation," *Plos One*, vol. 4, no. 2, 2009.

[31] M. J. Solomon and A. Varshavsky, "Formaldehyde-mediated dna protein crosslinking - a probe for invivo chromatin structures," *Proceedings Of The*

National Academy Of Sciences Of The United States Of America, vol. 82, no. 19, pp. 6470–6474, 1985.

[32] P. M. Lundquist, C. F. Zhong, P. Q. Zhao, A. B. Tomaney, P. S. Peluso, J. Dixon, B. Bettman, Y. Lacroix, D. P. Kwo, E. McCullough, M. Maxham, K. Hester, P. McNitt, D. M. Grey, C. Henriquez, M. Foquet, S. W. Turner, and D. Zaccarin, "Parallel confocal detection of single molecules in real time," *Optics Letters*, vol. 33, no. 9, pp. 1026–1028, 2008.

[33] D. Di Carlo, L. Y. Wu, and L. P. Lee, "Dynamic single cell culture array," *Lab On A Chip*, vol. 6, no. 11, pp. 1445–1449, 2006.

[34] T. Geng, N. Bao, M. D. Litt, T. G. Glaros, L. W. Li, and C. Lu, "Histone modification analysis by chromatin immunoprecipitation from a low number of cells on a microfluidic platform," *Lab On A Chip*, vol. 11, no. 17, pp. 2842–2848, 2011.

[35] F. B. Dean, J. R. Nelson, T. L. Giesler, and R. S. Lasken, "Rapid amplification of plasmid and phage dna using phi29 dna polymerase and multiply-primed rolling circle amplification," *Genome Research*, vol. 11, no. 6, pp. 1095–1099, 2001.

[36] K. Zhang, A. C. Martiny, N. B. Reppas, K. W. Barry, J. Malek, S. W. Chisholm, and G. M. Church, "Sequencing genomes from single cells by polymerase cloning," *Nature Biotechnology*, vol. 24, no. 6, pp. 680–686, 2006.

CHAPTER 4

SYSTEMS INTEGRATION FOR SINGLE MOLECULE ANALYSIS

4.1 Introduction

The development of lab-on-a-chip technologies bears many similarities to the development of radio and computer technology. In the early 1900's, vacuum tubes provided the necessary amplification to hear radio broadcasts. Each radio was expensive and often encased in a desk-sized housing making it a centerpiece household appliance. However, in the early 1960's the transistor began to replace the vacuum tube, allowing manufacture of radio units with smaller size and more power efficient operation. With manufacturing economy of scale, transistor components became increasingly affordable. Ultimately, methods for dense integration of the transistor enabled the development of increasingly portable radios and new system-level functionality to perform computational tasks.

In analogous progression, nanofluidics have demonstrated the miniaturization of discrete detection and sorting functions currently performed by tools that require considerably more sample material for analysis. While the existing infrastructure of the semiconductor industry could be used to manufacture these components with economy of scale, nanofluidic components presently require a laboratory of equipment and support infrastructure. For nanofluidics to become truly 'lab-on-a-chip' systems, which are practical for clinical and bedside diagnostic tools, considerable integration is required. This integration can take many forms: monolithic integration of optical sources and detectors, parallelized fluidic channel layouts, multi-function or multi-stage reagent processing, and dedicated information processing and computation.

Considerable effort in lab-on-a-chip development has been made in recent years.

Innovations in massively parallel, microfluidic processors have been developed to provide chemical processing on hundreds of independent nanoliter reaction chambers addressed using valve network that mimic the operation of multiplexors used for electrical signals [1]. Multi-function and multi-stage biochemical reagent processing has been shown in devices that entropically select molecules based upon their propagation through pillar arrays [2, 3] and sensitive detection using on-chip quantitative PCR [4]. The ubiquitous, low-cost availability of high power computing resources has allowed the construction of systems that perform real-time signals processing and thus enabled the development of anti-Brownian motion traps to study individual molecules [5, 6] and particle tracking for super-resolution imaging [7–9]. While several of these exciting developments have been incorporated to microfluidic and nanofluidic systems that examine individual molecules, scaling the accompanying systems necessary for optical excitation and detection of faint fluorescence signals remains a considerable scientific and engineering challenge. This challenge is largely the result of the low-autofluorescence requirement necessary to observe an individual fluorophore attached to a single molecule. In this regime, the combination of materials selection, fabrication technique, and optical engineering become paramount. In this chapter, we will discuss several engineering advancements in materials and fabrication techniques, toward enabling integrated optical excitation of single molecule fluorescence.

4.2 Spin-on-Glass Thin Films for Integrated Microfluidics

4.2.1 Introduction

We present a bilayer resist process for patterning hydrogen silesquioxane (HSQ) films using a single photolithographic step. Following a high temperature anneal,

our results reveal a significant transformation in the structure, surface morphology, and optical properties of the HSQ film. This film exhibits optical and chemical properties similar to fused silica, but in a processing context that offers unique opportunities for device integration, several of which are currently found only with precast polymers such as polydimethylsiloxane (PDMS). Laser-excited autofluorescence was shown to be identical to fused silica throughout the visible spectrum. Microfluidic structures formed using this bilayer process were applied to the study of single DNA molecules using laser-induced fluorescence (LIF) spectroscopy. Our method is amenable to integration with other complex materials and device structures, such as micro- and nano- electromechanical systems (MEMS and NEMS), nanophotonics, and electronic sensors.

Hydrogen silsesquioxane (HSQ) and spin-on-glass (SOG) are two porous silicates widely utilized in research and industrial microfabrication processes [10–13]. Feature dimensions scaling to sub-10nm and with high aspect ratios have been reported with HSQ as a negative tone electron beam lithography resist [13, 14]. The microelectronics industry has evaluated HSQ and SOG as a low-k dielectric for ultra-large-scale-integration circuit designs in order to reduce interlayer capacitance-voltage characteristics and achieve faster switching [15–19]. Boron and phosphorous doped SOGs are used as spin-on-diffusants to achieve spatially localized doping profiles for deep electronic junctions and contacts.

Films of HSQ can be spun to thicknesses ranging from 10-1000 nm by varying the percent solid content in the liquid solvent. In most cases, these films are easily removed with either tetra methyl ammonium hydroxide (TMAH) based developers or hydrofluoric-acid. Various studies of chemical and mechanical properties report that HSQ undergoes a transition from compressive to tensile stress during annealing [11, 15]. Exposure to oxygen plasma has shown to drastically change

surface wetting. Optical studies of these films using Fourier Transform InfraRed (FTIR) spectroscopy have demonstrated the stretching of Si-O bonds critical to the cage structure of the silsequioxane and the incorporation of -OH bonds during plasma treatment [10, 18–20]. Additionally, HSQ-metal interfaces can form silicide intermediates at the boundary layer during annealing [15, 17, 21].

While great emphasis has been placed on maintaining the porous structure and low-k dielectric properties of HSQ, our interests stem from possible interdisciplinary applications that would benefit from a silica-like material that is versatile in processing. Biological systems are now being studied using micro- and nanofluidics [22, 23], micro- and nano-electrical-mechanical-systems (MEMS/NEMS) [24, 25], and integrated optics [26, 27] created with conventional microfabrication techniques. A growing collection of literature even demonstrates integration of microfluidics with carbon-nanotube electrical sensors [28, 29], MEMS/NEMS resonators [30, 31], and integrated photonics [32, 33]. To maintain design and fabrication simplicity in these systems with increasingly complex functionality, materials serving multiple purposes and demonstrating low integration cost are desirable. Similar motivations have been central to the recent and widespread adoption of PDMS for lab-on-a-chip applications [28, 29, 32, 33].

We demonstrate a new bilayer resist process for interdisciplinary applications that uses HSQ. This process produces dense, silica-like films with low-loss optical characteristics in the visible spectrum and with ultra-low autofluorescence. The film was chemically stable with complete resistance to aqueous solutions and most solvents. Ridge-shaped features of dimension similar to the film thickness were successfully integrated within microfluidic channels without altering the ridge surface roughness, channel critical dimensions, or the conformal and hermetic seal with the substrate. The microfluidic channels were capped with a fused silica wafer using a

direct bonding method and then used to flow single DNA molecules, as measured with laser induced fluorescence spectroscopy. We envision future applications of this method will continue into the fields of MEMS/NEMS, nanophotonics, and electronic sensors.

4.2.2 Experimental Details

Material Processing The bilayer resist process is illustrated in Figure 4.1. Silicon (or fused silica) wafers were spin coated with the HSQ material, XR-1541 (Dow Corning) containing either 6% or 22% solids and then baked on a contact hotplate for 4 minutes at 170 °C. Wafers were air-cooled to room temperature to avoid film stress fracturing. A 10nm layer of cross-linked HSQ was formed by exposure to oxygen plasma using a reactive ion etcher (Oxford 80, Oxford Instruments). SPR700-1.2 Photoresist (Rohm Hass) in conjunction with an adhesion promoter were spun at 3000 RPM to form the bilayer resist stack, which was subsequently soft and post-exposure baked at 115 °C on a contact hotplate. The microfluidic channel pattern was exposed using a i-line stepper tool (GCA Autostep 200) and then developed using a TMAH-based developer, AZ MIF 300 (Clariant). Using the resist as a pattern mask, the 10 nm crosslinked layer was then removed from the developed regions with a 25 s etch in HF 100:1. A second development in AZ MIF 300, time dependent on HSQ film thickness, removed the unprotected HSQ film. The photoresist pattern mask was removed in successive cycles of heated oxygen plasma (Branson Barrel Etcher), which self-terminates at the previously cross-linked HSQ interface.

The porous film structure was collapsed and impurities were removed during a furnace anneal from 115-800 °C in argon. The ramped anneal was performed during four gradual temperature increases, each 80 minutes in duration and followed by

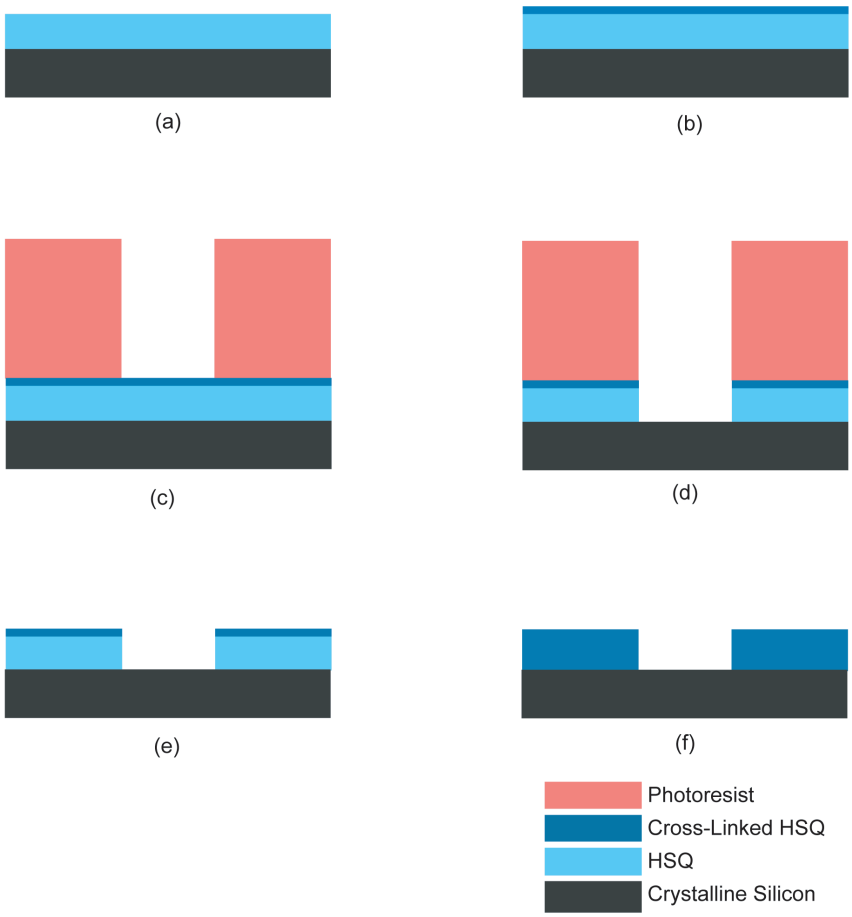

Figure 4.1: Schematic of the HSQ microfabrication process: (a) HSQ spin-coated (b) Top layer of HSQ is cross-linked using an oxygen plasma (c) Photoresist patterned using conventional photolithography (d) Pattern transfer into the HSQ (e) Photoresist removed in a heated, non-directional oxygen plasma. (f) Ramped anneal to 800 °C in argon ambient removes voids in the HSQ, forming a smooth amorphous silica film.

a 30 min dwell. The first and second ramps each increased the temperature by 100 °C, while the third and fourth ramps increased by 200 °C. This process lasted approximately 8 hr and was necessary for films greater than 600 nm thick. For sub-150 nm films, the anneal duration could be decreased to 3-4 hrs, starting at about 400 °C.

Process robustness and latitude were studied for various resist thicknesses and annealing conditions. Resist films of XR-1541 containing 6% or 22% solids content were formed with thickness ranging from 50-150 nm or 600-800 nm, respectively. The formation of stress-induced film fractures were monitored during process steps involving significant thermal cycling - the resist softbake, photoresist removal, and high temperature anneal.

Material Optical Properties Refractive index properties were measured using a variable angle spectroscopic ellipsometer (VASE, J.A. Wollam Co.) at the conclusion of each processing step which altered the HSQ material structure. The VASE collected polarization-dependent reflection values at three angles near the Brewster Angle, each over the 300-1000 nm wavelength range. Collected values were then fit using a generalized oscillator model to calculate film thickness along with both real and imaginary refractive index values.

Material autofluorescence spectra were collected using a customized microscope (IX-71, Olympus) for laser-induced fluorescence. A 488 nm wavelength diode-pumped solid state laser (Sapphire, Coherent Corp.) was incident on a dichroic mirror (Z488RDC, Chroma Technologies) and focused onto the thin film sample using a 50x 0.5 numerical aperture microscope objective (Olympus). Collected fluorescence was filtered through a 505 nm long-pass filter (HQ505LP, Chroma Technology) and detected through the confocal aperture of an optical fiber-coupled spectrometer (QE65000, Ocean Optics). Two milliwatts of laser power continually

excited the sample during a 5 min integrated collection of the autofluorescence spectra. Spectral scans were conducted for wavelengths 450 - 950 nm, with the transmitted autofluorescence spectra limited by the 505 nm long-pass filter.

Characterization and Application to Microfluidics This HSQ process was studied for viable integration with other device structures by applying HSQ atop silica substrates with ridge-shaped features on the surface. An atomic force microscope (AFM; DI3000 - Digital Instruments) operating in tapping mode (TESPA tips, Vecco) was used to measure process-induced surface roughness of both the HSQ film surface and the exposed regions of the silica ridge. These measurements were used to evaluate the feasibility of direct bonding techniques to HSQ film surfaces. Scanning electron microscopy was performed (Zeiss Ultra FESEM) to assess the reproduction accuracy of device critical dimensions and the coating conformality around ridges of various widths.

To culminate our findings, this bilayer resist process was used to form a microfluidic device to study fluorescently-labeled deoxyribonucleic acid (DNA). The microfluidic channel had cross-sectional dimensions of 80 nm by 1.9 μm (width by height) and was formed in annealed HSQ to produce a dense, amorphous film, free of fissures that could cause a fluid leak. Both sides of the fused silica wafer were coated with a protective layer of photoresist and then holes approximately 3 mm in diameter were sandblasted through the wafer to create access ports for fluidic reservoirs. The sandblasting powder was removed and the surface cleaned with various organic solvents. The patterned HSQ substrate and a 170 μm thick double-side polished fused silica substrate were submerged in an RCA standard clean bath (6 H_2O : 1 NH_4OH : 1 H_2O_2, heated to 70 °C). The wafers were dried and then caped by direct press bonding of the 170 μm silica substrate to the HSQ substrate, forming a wafer stack. The wafer stack was annealed during an 8

hour ramp from room temperature to 1050 °C and then cooled, making the bond permanent. The fluidic channels were filled with 0.45 M Tris-Borate EDTA (5x Concentrate TBE, Fluka) buffer and an applied voltage was used to electrokinetically drive fluid flow through the channel. A buffer solution containing 8 Kbp DNA intercalated with the fluorescent dye YOYO-1 (Invitrogen) was added to reservoirs and flowed. Flow was observed directly by passage of fluorophores in the channels using laser-induced fluorescence microscopy.

4.2.3 Results and Discussion

Materials Processing

A barrier layer or 'shell' of cross-linked HSQ was necessary to form the bilayer resist stack. Dissolution of the HSQ film by adhesion promoter or photoresist solvents occurred when the cross-linked shell was not formed. Cross-link formation was attempted with the RIE plasma chemistries of, CF_4, CHF_3O_2, and O_2. Fluorine-based chemistries did form a barrier layer, but caused undesirable film thinning during the plasma treatment. Barrier layers formed with oxygen plasma, however, exhibited a sub-10nm decrease in the overall film thickness from 628.5 ± 3.5 nm to 619.2 ± 2.8 nm. Treatments of 30-150 s duration were performed on various spun films and caused no measurable change in the 'shell' layer thickness or in processing parameters - all cross-linked films were etched during a 25 s submerge in HF 100:1. Since 'shell' layer formation was not plasma chemistry specific, we concluded that plasma damage from ion-bombardment was responsible for crosslink formation.

The HSQ film underlying the cross-linked barrier layer was removed with TMAH-based developer, instead of a fluorine-based RIE chemistry. The developer functioned as a highly-selective isotropic etchant, which removed exposed HSQ patterns without increasing substrate surface roughness. While the photore-

sist mask development continued during this etch step, the patterned HSQ 'shell' served as the dominant etch mask. Cross-sectional scanning electron micrographs of the film shown in Figure 4.2 illustrate a concave sidewall profile, indicative of an isotropic etch process, and a thin overhang, formed from the HSQ 'shell' layer. In significantly over-etched films, the cantilevered 'shell' layer collapsed and, in many cases, covered the film cross-section and terminated further etching. Calibration of the development time was necessary to achieve accurate feature size reproduction.

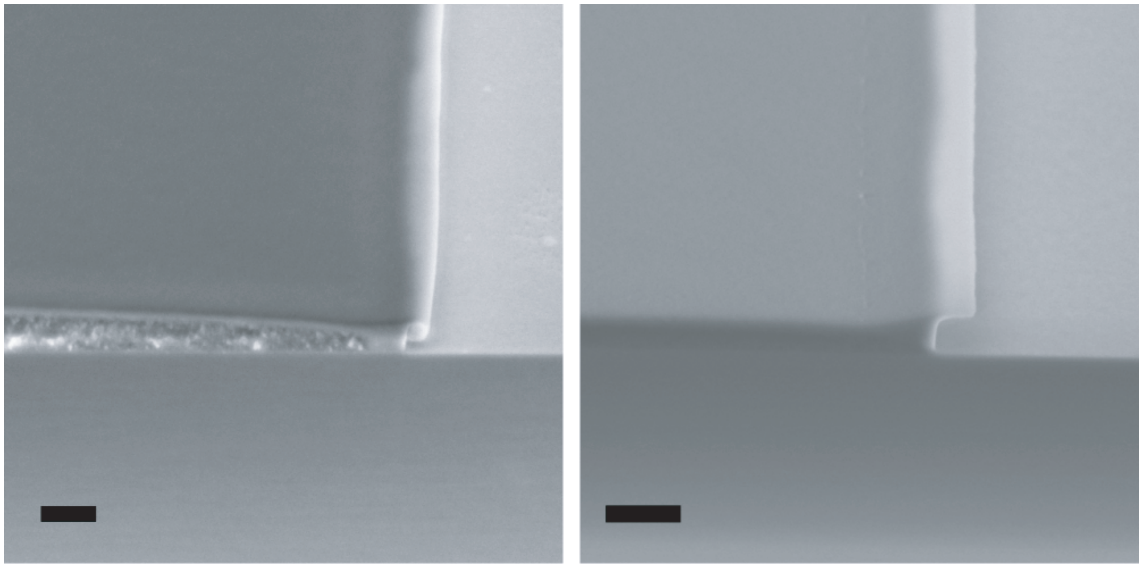

Figure 4.2: Electron micrographs illustrate the effect of annealing an HSQ film (Film made with 6% solids HSQ solution applied to a silicon substrate). Scale bars correspond to 200 nm. (left) HSQ film cross-section prior to annealing. The cross-linked top-layer was approximately 10 nm thick. The HSQ film bulk exhibited a porous, sponge-like structure and is compressively-stressed. (right) Following an 800 °C anneal in an argon ambient, the HSQ film cross-section collapsed into a smooth layer of amorphous silica, which is tensile-stressed.

Photoresist removal with chemical solvents, such as acetone and n-methylpyrrolidone, damaged the HSQ film prior to annealing and necessitated the use of RIE methods. Etchers that formed a directional plasma on a cooled electrode caused photoresist

microclusters to form and bind permanently to the HSQ surface. A resist asher that utilized a heated, non-directional plasma was effective at removing photoresist quickly and without surface residues on wafers with thin HSQ films (< 150 nm). However, the rapid thermal cycling (> 200°C/min) during resist ashing caused significant film stresses and widespread cracking on thick (> 300 nm) HSQ layers. A high-power barrel etcher (Branson/IPC) with a thermal budget of 160 °C, provided a more gradual elevation in temperature and was able to remove the photoresist without surface residues or film cracking.

A high-temperature anneal in argon was used to collapse the porous film structure and remove impurities. Annealing requirements were found to vary as a function of film thickness. Layers of thickness 50-150 nm were annealed starting at 400 °C and ramped to 600, 700, 800, or 900 °C over 1 hour. Thin film coloration changes became more widespread and uniformly distributed at the onset of complete film collapse near 800 °C. Collapsed films exhibited a dense, amorphous structure as show in Figure 4.2. Thin films applied to both pieces and whole-wafer substrates did not experience stress fracture formation with this thermal gradient. By comparison, HSQ films 600-800 nm thick had stringent thermal budget requirements. A lower starting temperature of 115 °C was necessary to reduce the quantity and size of stress-induced fractures. Fracture formation was studied during anneal ramp times of 4, 6, and 8 hr, all from 115-800 °C. As the ramp time increased to 8 hr, the number of stress fractures decreased to fewer than 10 on a 100 mm diameter substrate.

Material Optical Properties

Thermal and plasma processing of HSQ films demonstrated visible changes in thin-film coloration and refractive index properties. Changes in film thickness were studied after the HSQ softbake at 170 °C, cross-linked 'shell' formation, and high

temperature anneal steps, using a VASE. The film thicknesses measured (with one standard error) were 628.5 ± 3.5 nm, 619.2 ± 2.8 nm, and 514.9 ± 0.5 nm, respectively. Treatment with oxygen plasma did reduce overall film thickness by approximately 9 nm, but caused a sub-0.001 change in the real refractive indices, as shown in Figure 4.3. A anneal to 800 °C, however, caused a 17% reduction in overall film thickness, in corroboration with cross-sectional SEM images shown in Figure 4.2 for an 80 nm thin film. The inert argon ambient present during annealing excluded the possibility of refractive index changes due to chemical incorporation into the film. Therefore, increased real refractive indices shown in Figure 4.3 were attributed to increased effective film density, causing the optical constants to approach fused silica characteristics. Annealing removed trapped impurities, causing a dramatic reduction in the imaginary refractive indices and film optical absorption, shown in Figure 4.3. The constant imaginary refractive index for all wavelengths is indicative of a lossless optical film.

Annealing caused autofluorescence spectra of HSQ films to become indistinguishable from fused silica. Fused silica is the 'gold-standard' in fluorescence microscopy for its broadband, ultra-low autofluorescence over visible wavelengths and was used as the supporting substrate in the aurofluorescence study of all films. Normalization of autofluorescence per unit thickness was not performed, because in an applied context, each material has a dramatically different usable thickness. Film thicknesses studied within this context include: 514-628 nm HSQ films, 100-1000 μm PDMS films, and 170 μm fused silica. Initially, avalanche photodiodes (APDs) were used to collect emitted fluorescence, however, the unannealed HSQ and PDMS exhibited considerable time-dependent photobleaching. To standardize the film autofluorescence in the presence of photobleaching and to characterize its spectral content, a spectrometer with integrated cooling on the detection CCD was

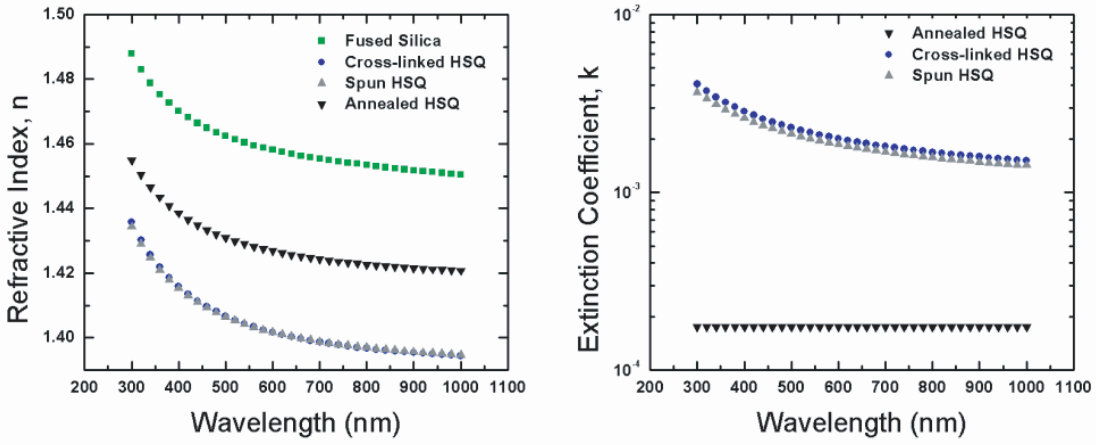

Figure 4.3: HSQ film optical properties were measured as a function of material processing using a variable angle spectroscopic ellipsometer. (left) Annealing removed voids in the HSQ film, causing the effective refractive index to increase. The film thickness prior to annealing was 619.2 ± 2.8 nm and following annealing was 514.9 ± 0.5 nm. (right) Impurities causing absorption were removed by annealing, rendering the film virtually lossless. Fused silica (not shown) demonstrated an extinction coefficient of 0 across this spectral range.

chosen to achieve a low-noise, 5 min integrated measurement for all films. PDMS exhibited pronounced photobleaching and a cluttered autofluorescence spectral signature, shown in Figure 4.4, with both elevated broadband emission and distinct peaks at 504, 522, and 566 nm, as compared to fused silica in Figure 4.4. Spun HSQ films also exhibited a dominant fluorescent emission at 546 nm. We believe this peak was caused by organic solvents and material impurities trapped within the porous film structure, like that of Figure 4.2. A high temperature anneal on HSQ removed absorption-based pathways to fluorescence emission, and reduced the annealed HSQ autofluorescence in Figure 4.4 to approximately that of fused silica. Fused silica-like autofluorescence of annealed HSQ films makes them a new and important material system for fluorescence applications.

Versatility in Integration and Application to Microfluidics

HSQ films of two different thicknesses were used to construct microfluidic devices, as shown in Figure 4.5. Thick films of HSQ were used to form selectively cover ridge-shaped lines, to demonstrate integration and a no-damage property during processing. Ridges were 2 mm long and with widths 0.3-5.0 μm, were etched 200 nm into the surface of a fused silica wafer. The bilayer resist process was performed atop these structures using a solution of HSQ with 22% solids, which resulted in a silica film 514 nm thick. Microfluidic trenches were formed in the HSQ during lithographic patterning steps, revealing select regions of underlying ridges, as shown in Figure 4.6. For ridge widths less than the 514 nm film thickness, trench walls were continuous and hermetically sealed around the ridge, however noticeable line edge roughness was observed. The designed trench width was 10.0 μm and the fabricated width was 11.1 μm. The difference is attributed to the etch isotropy, which extends the trench width by approximately 0.5 μm on each side. For ridge widths greater than the film thickness, stress fractures and preferential

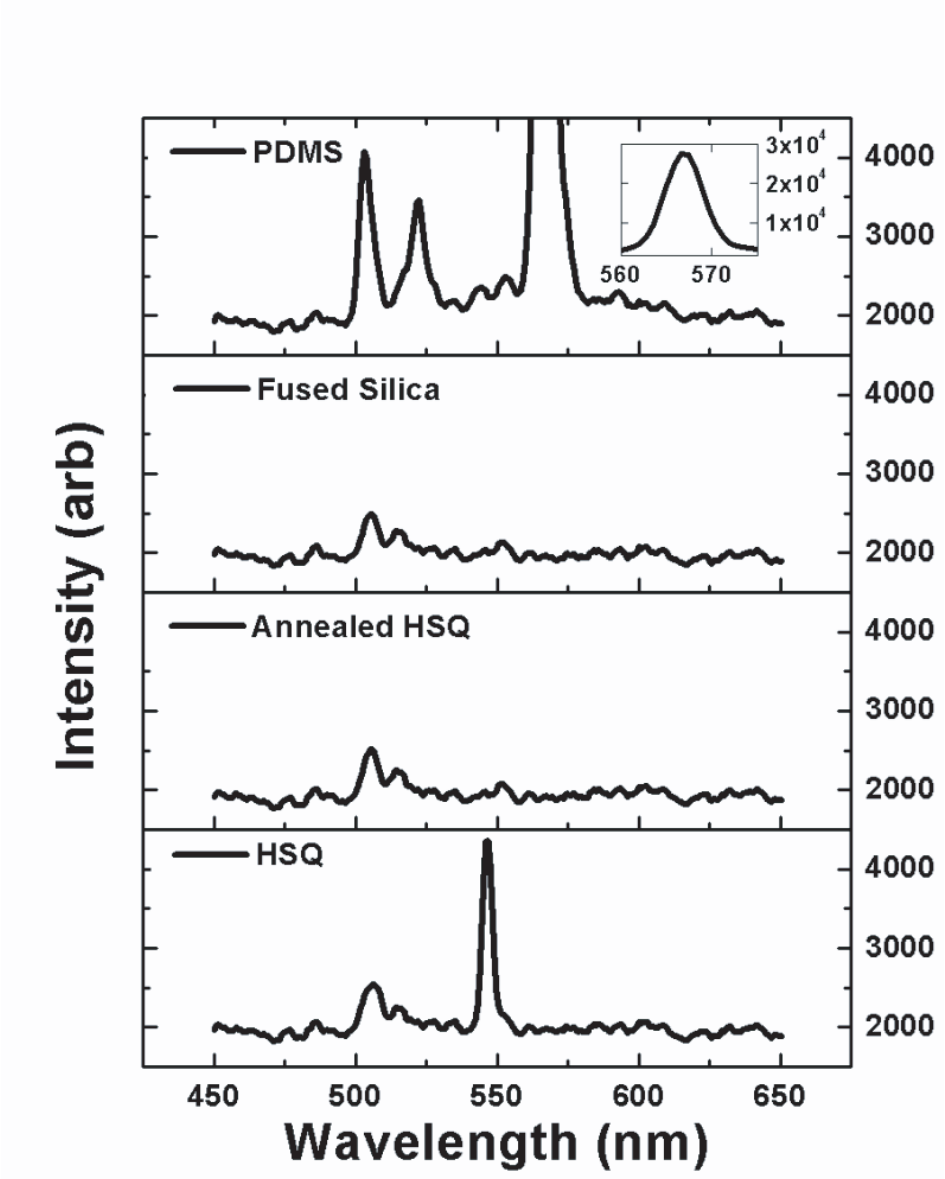

Figure 4.4: Laser-induced material autofluorescence was measured as a function of material processing and relative to another common lab-on-a-chip material, PDMS. Annealing the HSQ removed the autofluorescent spectral peak at 546 nm, reducing the overall autofluorescence spectrum to approximately that of fused silica. PDMS contained significant autofluorescent spectral peaks at 504, 522, 566 nm, far exceeding the annealed HSQ autofluorescence.

etching along the ridge were observed.

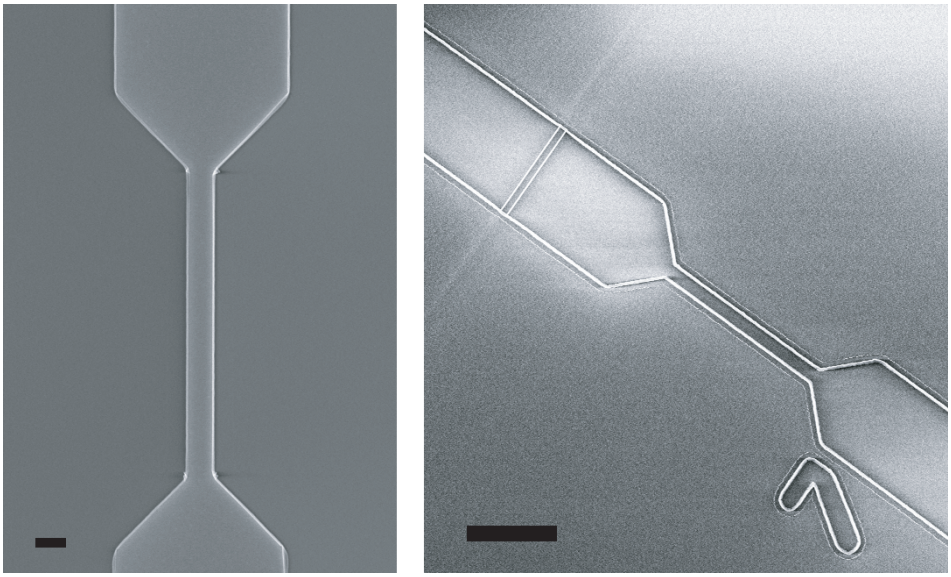

Figure 4.5: Electron micrographs of various fluidic devices demonstrate process versatility. (left) The trench for a microfluidic channel was formed in an 80nm thick layer of HSQ, using a 6% solids content. The constricted channel dimension is 1.9 x 0.08 μm and can be used for laser-induced fluorescence measurements requiring femtoliter fluid confinement. Scale bar corresponds to 2 μm. (right) A microfluidic trench was formed around an optical waveguide using a 514 nm thick layer of HSQ, made with a 22% solids content. In this way, structures of varying height, material, or geometry, such as fluidic mixers and entropic traps, could be incorporated inside microfluidics. Scale bar corresponds to 10 μm.

A direct correlation between film surface roughness and the spun film thickness was observed. Roughness was assessed on 15 different 1 μm^2 areas for each surface type using a tapping-mode AFM. Processing effects on surface morphology were studied before and after a high temperature anneal and in regions where pattern transfer was performed using a wet etch. These results are summarized in Table 4.1. The 6% solids spun films demonstrated remarkably smooth surfaces with sub-10 angstrom surface roughness, making this surface suitable for direct wafer bonding [34], an appealing characteristic for device integration. In contrast, thick HSQ films

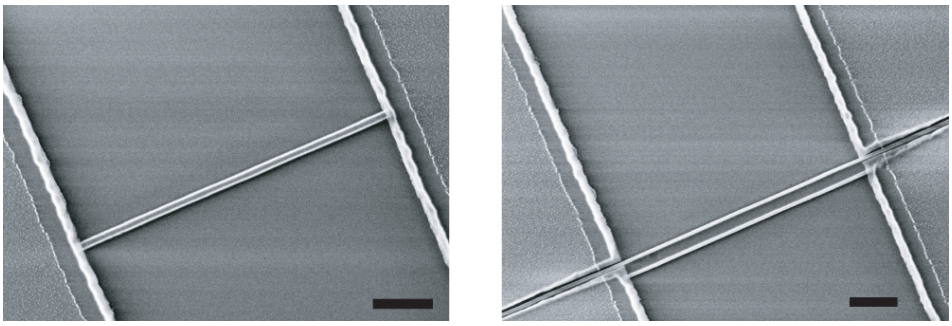

Figure 4.6: Scanning electron micrographs illustrate a ridge spanning the trench (visible), which continues, buried underneath the HSQ trench walls (not-visible). No damage was caused to the ridge during fabrication of the HSQ trench. Scale bars correspond to 2 μm. (left) A hermetic seal was formed at the intersection of trench walls and the ridge, for ridge widths (391 nm) comparable or less than the HSQ film thickness (514 nm). (right) Material stress-induced fractures caused delamination of the HSQ trench around the ridge, when the ridge width (768 nm) was greater than the film thickness (514 nm).

experienced a change in roughness from 3.5 to 5.2 nm, attributed to reorganization of film structure and removal of impurities during the anneal step, rendering them incapable of direct bonding protocols, without subsequent chemical mechanical polishing (CMP). Regions of fused silica substrate uncovered during the pattern transfer were also exceptionally smooth, well below the manufacturer's sub-1 nm surface roughness specification. Some silica ridges formed within the HSQ trenches exhibited an increased surface roughness, as compared to planar regions of exposed silica. The ridge-top morphology was observed to have a significant standard deviation and regions of the ridge with increased roughness possessed a positive-relief profile relative to adjacent exceptionally smooth regions. This suggests that increased surface roughness on the ridges is not due to process damage, but rather trace residues of HSQ remaining from the wet-etch process. Depending on the host substrate material and process requirements, these residues can be removed by a second, brief dip in HF 100:1 following the developer-etch step illustrated in

Table 4.1: Surface Roughness Throughout HSQ Film Processing

Roughness(nm)	Crosslinked HSQ	Annealed HSQ	Silica Surface	Silica Ridge
22% Solids Film	3.5 ± 0.1	5.2 ± 0.2	0.3 ± 0.1	0.7 ± 0.3
6% Solids Film	0.5 ± 0.1	0.6 ± 0.1	0.8 ± 0.1	N/A

Figure 4.1.

Direct bonding of annealed thin HSQ films to fused silica substrates was used to form sealed microfluidic devices. Our bilayer resist process was performed on a 500 μm thick fused silica substrate, which produced HSQ trenches 80 nm x 1.9 μm in cross-section and with surface roughnesses similar to those reported in Table 4.1. Wafers were sandblasted to create fluidic access ports and then cleaned using the RCA process previously discussed. During the initial direct bonding, wafers were aligned using the wafer flat and then pressed together at the center. Pressure was applied starting at the wafer center and moving radially to the perimeter in order to propagate the extent of the bonded region. This process was repeated for a total of about 10 min to bond the available clean surfaces. The extent of bonding can be seen in Figure 4.7. Channels had a hermetic seal that did not leak, evident in the refractive index contrast between the identifying 'number seven' that was air-filled and the adjacent fluid channel that was fluid-filled.

To culminate our findings, HSQ microfluidics bound in the fused silica wafer stack were used to study fluorescently-labeled DNA. Fluidic reservoir access holes, previously formed during sandblasting, were bound by a plastic port and then filled with 5x TBE with 1.0% polyvinylpyrrolidone (PVP) to create fluidic connection between two reservoirs and to reduce electroosomotic flow. The complete channel,

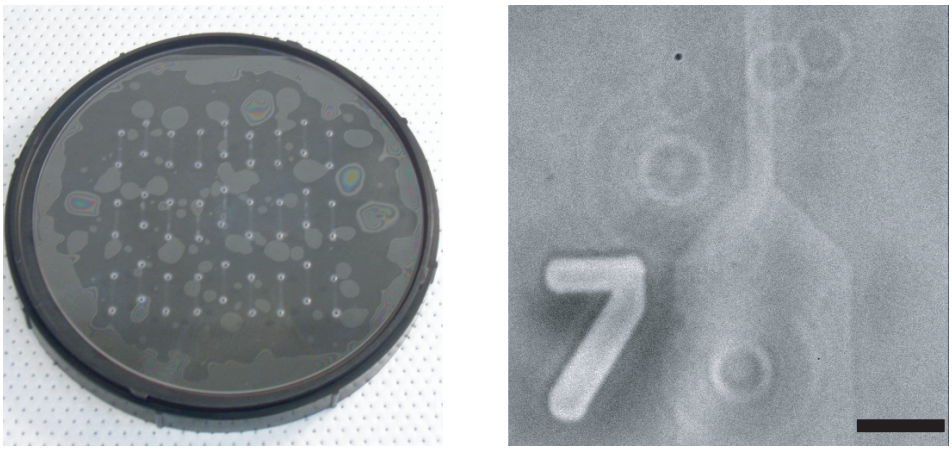

Figure 4.7: Long range bonding of HSQ to fused silica bond and formed a hermetic seal with micrometer scale features. (left) Photograph of the fused silica wafer stack (100 mm diameter) with HSQ fluidics after touch bonding and furnace anneal. Over half of the devices were sealed with no significant defects. (right) Optical micrograph of a fluid-filled channel adjacent to an air-filled number. Scale bar is 5 μm.

approximately 12 mm in total path length, filled in 1 min. A 50 V bias was applied to electrokinetically drive fluid flow at a rate of approximately 0.5 mm/s. Intercalated, 8 Kbp DNA (1:5 dye to base pair ratio) was suspended in the buffer solution at a concentration of approximately 200 pM. A laser excitation power of 225 μW at the 488 nm wavelength was used to induced fluorescence within the channel. The same dichoric and fluorescence emission optics used to measure material autofluorescence were also used in this experiment. Time-resolved photon collection was performed using photon counting APDs. Fluorescently labeled molecules were identified using Matlab routines were used to combine photon counts into 50 μs time bins as shown in Figure 4.8. Using a threshold five standard deviations above the fitted Poission mean noise of the system, we counted over 7,694 molecules in 10 min.

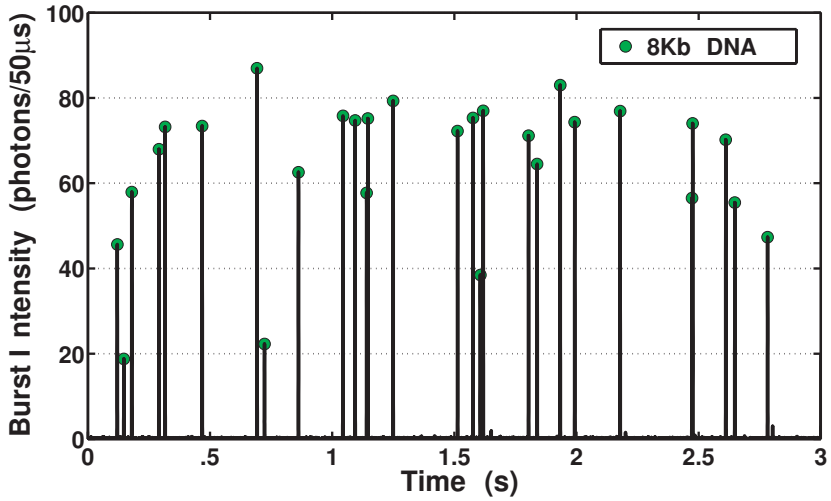

Figure 4.8: Single molecule detection within thin film HSQ channels.

4.2.4 Conclusion

A novel, bilayer resist process for patterning HSQ films using a single photolithographic step was created. This process was enabled by formation of an interfacial layer, or 'shell,' of cross-linked of HSQ that is impermeable to most resist solvents, thus isolating the respective resist films. Process latitude and robustness were demonstrated using the HSQ resist, XR-1541, to form 50-500 nm thin films. When implemented in this process, HSQ was lithographically defined with a positive-tone photoresist mask and then removed using a self-terminating developer-etch process that does not damage the underlying substrate or devices. We incorporated ridge-shaped features within microfluidic trenches and successfully demonstrated the 'no damage' property, while maintaining accurate reproduction of critical feature dimensions. HSQ film surface roughness was measured and demonstrated in wafer bonding to fused silica substrates. Film stress induced defects were virtually eliminated by use of a stringent, sub-200 °C thermal budget during processing and a gradual ramped high-temperature anneal to 800 °C . The anneal step incurred important changes in film structure and optical properties, demonstrating conver-

sion to a smooth, amorphous silica film with virtually lossless transmission and ultra-low autofluorescence characteristics over the visible spectrum. These optical properties were found to be highly similar to fused silica and thermally-grown silica. When compared to its contemporary counterpart, PDMS, annealed films of HSQ exhibit significantly lower autofluorescence and possess complete chemical resistance to aqueous solutions and most solvents. A demonstration of these advantageous film properties was culminated during single molecule measurements of fluorescently-labeled DNA inside a HSQ-based microfluidic channel. We conclude that this process is both versatile and amenable to integration with other device structures and processes for interdisciplinary applications.

4.3 Integrated Waveguides for Optical Excitation

4.3.1 Introduction

Single molecule studies of biological systems are increasingly used to investigate the structure, biochemical status, and role of individual RNA, DNA, and protein molecules in guiding life processes. While these methods provide useful insight to the biological world, their analysis throughput is often limited to a fraction of the total sample or a specific locus within the genome. This limitation has been addressed as part of fluorescence-based, single molecule DNA sequencing technologies [35], however studies of mRNA copy number variation, aptamer-protein complexes, and the epigenetic status of chromatin would benefit greatly from a high-throughput single molecule analysis method. Furthermore, high-throughput detection of these samples would be enhanced by sample sorting and recovery to investigate their properties using complementary techniques.

Systems integration, as part of miniaturized 'lab-on-a-chip' components, has

been the subject of intense research interest to realize high-throughput biochemical detection methods in a compact size. In particular, microfluidic and nanofluidic systems have demonstrated significant advances in systems integration that have led to massively parallel, individually-addressed reaction volumes for cell processing [4]. Many of these innovations are the result of optical-grade polymers, such as PDMS, that allow facile integration of valves, electrodes, and mixers into a common device. This material system has also been used to develop imbeddeded optical waveguides [36, 37], deformable optical elements [38], and frenel zone plate arrays [39, 40], to multiplex the optical excitation and detection process used to probe biological molecules during flow within a microfluidic channel. However, systems integration for excitation and detection of single molecule fluorescence requires ultra-low material autofluorescence across a broad range of visible wavelengths. Therefore, single molecule fluorescence studies in micro- and nanofluidics have been restricted to fused silica, quartz, and other chemical (CVD) or physically (PVD) deposited dielectric thin-films common to the semiconductor industry. Recent work using anti-resonant reflection optical waveguides (ARROWs) [41–43] has made signifcant progress in the integration of optical excitation and detection functions within microfluidics, using Bragg-guiding for fluorescence collection within 135 fL optical inspection volumes formed at the intersection of liquid-core and solid-core waveguides. However, these structures lack the volume confinement to explore individual molecules at nanomolar concentrations or greater, which are conducive to higher-throughput analysis at physiologically-relevant concentrations. Additionally, Bragg-guiding in the thin-film stack of ARROWs imposes challenges in fluorescence collection due to limited wavelength support for efficient guiding and coupling of fluorescence.

Here we present developments toward combining an integrated optical waveg-

uide and an array of parallel nanofluidic channels to excite fluorescence from individual molecules in a high-throughput format. Using a 150 aL optical inspection volume, formed by the intersection of each waveguide and nanofluidic channel, we strive to demonstrate throughput at 50,000 molecules/min using a collection of just 8 fluidic channels. Fluidic channels are etched into the cladding to achieve spatial overlap of the entire fluidic channel cross-section with the waveguide's evanescent mode, creating a permanently-aligned optical probe volume within the fluidic channel and thereby greatly reducing the degrees of freedom for mechanical drift during extended-duration experiments. The evanescent mode profile is engineered using high-index contrast silicon nitride waveguides embedded within a glass cladding, to achieve ultra-low autofluorescence and efficient, wavelength-agile co-propagation through many waveguide-channel junctions; these many attributes are conducive to continued device scaling while retaining single molecule fluorescence sensitivity. A 200 micrometer-thin layer of PDMS caps the fluidic channel at a distance to minimize coupling to autofluorescence, while also allowing the use of cover-slip corrected immersion optics for highly-efficient fluorescence collection with a standard upright fluorescence microscope. This thin PDMS layer creates opportunities for facile on-chip integration with electrodes, valves, and other structures.

Device Fabrication

A 100 mm silicon wafer with $< 100 >$ crystal orientation was used as a substrate. A thermal oxidation of the silicon at 1000°C was performed to grow a 2.0 μm bottom layer clad for the optical waveguide. A 180 nm layer of stichometric silicon nitride was then deposited using a low-pressure CVD process. Electron beam lithography (JEOL 9300FS) was then used to form a positive-tone pattern in a layer of PMMA spun onto the silicon nitride. Following PMMA development, a 20 nm thin layer of chrome was evaporated into the waveguide-shaped openings and an overnight liftoff

was performed, resulting in waveguide-shaped chrome lines. This chrome hardmask was used during a subsequent reactive ion-etch in CF4 to form the waveguides and then removed using a liquid chrome etchant. Wafers were cleaned using a hot piranha solution to remove organic residuals. A layer of silicon dioxide measuring 1.5 μm was then deposited using a plasma-enhanced CVD process to create the top layer clad for the optical waveguide. Photolithography was then performed to create a positive-tone pattern of the nanofluidic channels, which was transferred 950nm into the SiO2 top clad. The photoresist was removed and a whole-wafer etch was performed to thin the top clad from 1.5 μm to a final thickness of 1.0 μm. The devices were coated with a protective layer of photoresist and diced into chips measuring 7.5 x 15 mm. The protective photoresist was removed the devices were ready for capping with a thin PDMS layer.

A 100 mm silicon wafer was treated with SigmaCoat (Sigma Aldrich) to render the surface strongly hydrophobic. A mixture of 1:10 Silgard PDMS was prepared, degassed, and then 3 mL dispensed onto the silicon wafer for spin coating at 200 RPM. After spin coating, the PDMS coated wafer was cured at 160°C for 15 minutes and then removed to cool. The PDMS was then cut into gaskets of matched size to the waveguide chips. The PDMS and waveguide chips were rendered hydrophilic using an oxygen plasma treatment and then pressed together to form a permanent bond and rendered a completed fluidic device.

Optical Measurement Setup

Free-space laser sources at visible wavelengths (488, 561, and 640nm) are fiber coupled using a doublet-lens pair placed on a rotation mount at approximately the same x, y position as the laser source. These fiber-coupled laser sources were coupled into waveguide devices using a free-space aligned optical fiber mounted on a translation stage with spatial freedom in x, y, z, θ, and ϕ. The chip con-

taining optical waveguides and fluidics was mounted on a three-axis translation stage to enable the optical waveguides and fibers to meet within a limited range of motion. An upright microscope system, was formed using a compound zoom lens with an infinity-corrected microscope objective. Fluorescence emitted by the optical waveguide structure was imaged by this system using either an intensified CCD camera or the confocal aperture of a optical fiber coupled to an avalanche photodiode. Standard fluorescence optics, such as dichroic mirrors and emission filters, were placed within the optical path of the microscope system to provide adequate rejection of laser excitation and bandpass collection of fluorescence.

Optical Characterization of Integrated Waveguide Performance

Optical waveguide transmission and coupling losses were fabricated to implement the cutback method. In this method, waveguides are fabricated with tapered couplers on one or both ends and then measured to isolate losses associated with mode field conversion during coupling. This method also allows a measurement of the combined transmission losses, whether due to material absorption, scattering defects, or multi-mode propagation losses. System autofluorescence was quanitified both by the use of a fiber coupled spectrometer with input longpass filtered or by fiber-coupled APDs with input bandpass filtered.

Sample Preparation

Samples of 8 Kbp DNA fragments, isolated from a DNA ladder, were labeled with DNA stain, YOYO-1, to provide bright, easily visible fluorescence.

Actuation of Electrokinetic Flow

Channels were treated with oxygen plasma immediately prior to use to encourage a hydrophilic surface condition for rapid filling. To aid the filling process, 30%

ethanol was added to buffer solutions during the initial filling period to reduce surface tension and improve filling speed. After a fluidic connection was established at both the input and output ports of the device, the ethanol solution was displaced by a buffer solution of 5x Tris-EDTA containing 0.3% PVP and 0.1% Triton X-100.

4.3.2 Results and Discussion

Integrated Optical Waveguide Design - Iteration 1

Early exploratory efforts in waveguide layout were instrumental in understanding the design space constraints when working with integrated optics at visible wavelengths. To explore waveguide efficiency in the visible spectrum, structures with a 2mm lateral offset from input to output across a chip were constructed. With this design, cross-chip coupling through the cladding was significant and the design required two, independent x,y,z stages for waveguide input and output. The intent was to excite and collect fluorescence using a common waveguide. The idea was not fully-developed, given that single molecule fluorescence provides a scarcity of photons and that coupling into a high-index contrast waveguide requires wave vector matching, which is unlikely to happen given the tumbling motion of fluorophores that randomizes the polarization and direction of the emission process. Scattering within the waveguides and off various reflective interfaces was very noticeable, but helped to illustrate the challenges of operating the integrated waveguide structures at visible wavelengths.

Given these lessons all occurred at once and it is best not to change many variables simultaneously, the next revision focused on improving the optical coupling and propagation efficiency of these structures. Since the scattering observed seemed excessive and unrelated to electron beam lithography processing or reactive ion etching, as scattering centers seemed to be randomly placed and rarely

allowing the optical mode to propagate more than 1 mm, efforts were focused on materials characterization of the thin films and device geometries that minimized path length and coupling to cladding modes.

Optical Materials Characterization

We explored a variety of deposited, dielectric thin films suitable for propagation at visible wavelengths. Our options were bounded by the collection of PECVD and LPCVD tools available in the Cornell cleanroom. In PECVD films, silicon oxynitride, silicon nitride, high-stress silicon nitride, and silicon dioxide were the available films with refractive index greater than thermally-grown silicon dioxide. In LPCVD films, low-stress silicon nitride (silicon rich) and high-stress silicon nitride (stichometric) were available. PECVD films available at the time had more hydrogen burried within the film than LPCVD films, typically were less dense and prone to pinhole-defects, and exhibited film thickness nonuniformities that could vary upto 5% across a 100mm wafer depending on recipe conditions and material. Whereas LPCVD films were dense, highly conformal, and exhibited nonuniformities of 2% or less across a wafer. Optical films were measured using a variable-wavelength, spectroscopic ellipsometer. This tool is particularly useful in characterizing these films for optical waveguides, because it allows development of various mathematical models to accurately fit and extract both the n (real refractive index) and k (imaginary refractive index) parameters for a film at wavelengths extending from 350-1700nm, the near ultraviolet to the infrared. This ellipsometer was also used in corroboration with high temperature furnaces to study the optical effect of high temperature annealing on removing hydrogen or other CVD byproducts trapped within the film during formation. Notably, oxyntride and low-stress silicon nitride exhibited substantial imaginary refractive index components, making them lossy optical films for waveguiding. It became clear that these losses were

evident in the LPCVD film of low-stress silicon nitride used to construct the first generation of optical waveguides. Based upon these measurements, stichometric silicon nitride became the material of choice for low-loss optical propagation at visible wavelengths.

Integrated Optical Waveguide Design - Iteration 2

Building upon lessons learned, the next iteration of waveguide design utilized a waveguide core composed of stoichmetric silicon nitride and were formed in U-shaped geometries. This geometry allowed the use of silicon v-groove structures to mount the optical fibers for both input and output coupling on a common side of the device, therefore only requiring a single, three-axis translation stage. Additionally, the silicon v-groove has a 0.5 μm absolute center-to-center position tolerance, all optical fibers within the array would be simultaneously aligned on a 250 μm incremental spacing. These v-groves were prepared with single-mode and multi-mode optical fibers with a straight cleave. This allowed for a single-mode, Gaussian optical profile with mode field diameter of 5 μm to excite to excite the waveguide and a comparatively higher numerical aperture multi-mode optical fiber with mode-field of 50 μm to more efficiently capture the light at the waveguide into a wide-collection output. These design changes made a significant improvement in the coupling and propagation efficiency of guided, visible light within these structures.

Examples of the multi-millimeter scale propagation of light was demonstrated at the 488nm and 561nm wavelength to then measure the coupling and propagation efficiency. At the 488nm wavelength, tapered couplers caused a loss of -3dB of the power launched when using end-fire butt coupling to a straight-cleaved optical fiber and propagation losses appeared to be on the order of -1 dB/mm. At the 561nm wavelength, tapered coupler loss was closer to -2dB and propagation loss was closer

to -0.5dB/mm. Considerable scattering is still observed in these structures, but is uniformly emitted from the structure sidewalls.

The next step was to incorporate fluidic channels within the top clad above the waveguide without damaging the waveguide itself. In this iteration, chemical mechanical polishing was not used to planarize the structures, unlike in subsequent designs, because the goal was to encapsulate the fluidic devices using a simple glass to PDMS bond. Fluidic channels were etched 950 nm into a 1500 nm clad. Based upon computational simulations of the evanescent optical mode profile, the optimal region of excitation should occur within approximately 200nm of the waveguide. Therefore, a 'blanket' or whole-wafer etch was performed for an additional 400 nm to lower the height of the fluidic channel to within reach of the evanescent field. While the entire cross-section of the fluidic channel will not be uniformly excited in this design, the intent was to demonstrate proof of principle and to minimize coupling to the bonded PDMS layer capping the structure. PDMS gaskets 2 mm thick were prepared, cut, and plasma treated along with the completed waveguide device in Clark Hall using gasses present in the ambient room environment. Despite considerable efforts and literature suggesting this basic procedure, we were unable to form a rigid PDMS bond to the device.

As a result of the first waveguide design iteration, we attempted the use of microscope objective-based fluorescence collection normal to the plane of the device. However, due to geometric considerations it was not possible to optically couple the waveguides into the device using a standard inverted microscope platform. Therefore, a custom-built upright microscope was constructed using a zoom lens system adapted with an infinity-corrected microscope objective. While this seemed a good idea in principle and in general CAD design, practical implementation helped us to appreciate the experimental challenge of trying to place optical fibers, fluidic

reservoirs, and the footprint of a high magnification microscope objective within the 7.5 x 15 mm waveguide chip dimensions. This experience taught one of the most important lessons of all, accessing the fiber and fluidic inputs of the device on the same side as the optical collection is virtually impossible within practical geometric constraints. Furthermore, when this result was considered in view of poor PDMS bonding, we were resolved to create devices on fused silica and to bond using coverslip thickness fused silica wafers, as per the process more typical of our previous nanofluidic channel devices.

Integrated Waveguide Design - Iteration 3

With an appreciation for geometric design constraints, both on and off-chip, we proceeded to construct optical waveguides on a fused silica substrate to allow optical access on both sides of the wafer. While most process steps established for processing on silicon were directly translated to fused silica, direct wafer bonding with a cover-slip thickness fused silica wafer requires a surface with RMS roughness less than 2 nm and good overall planarity. To accommodate this requirement, the top-clad of PECVD deposited oxide must be planarized using chemical mechanical polishing (CMP) prior to etching of the embedded nanofluidic structures. This is a considerably challenging task because the available metrology for post-CMP evaluation utilized film thickness mapping tools that do not work well with completely transparent substrates and since wafer-to-wafer variation in PECVD is inherent to single-wafer processing. Despite these challenges, monitor wafers using a silicon substrate and processed using the same parameters, provided a reasonable estimate of process parameters and variability. However, due to complications beyond control, the post-CMP ammonium hydoxide cleanup failed to remove all the silica colloid particles (SS12) used during planarization from the wafer surface. Since this colloid only remains in suspension over a narrow range of pH, these particles

were found irreversibly bound across the wafer surface after the post-CMP cleanup step, which inhibited direct bonding to the coverslip-thickness glass. Additionally, we noticed a slight bowing of the wafer, possible due to the stresses of he deposited film, that affected the wafer planarity necessary for bondin. However, given additional time, both of these complications can be resolved by proper operation of the post-CMP cleanup tool and a deposited film on the wafer backside to balance stress effects.

The greatest unresolved challenge pertained to the endface polishing of waveguides on a fused silica substrate. Unlike the silicon devices of design iterations 1 and 2, polishing the waveguide endface of these device resulted in substantial surface damage that typically caused tearing and shattering of the glass films surrounding the waveguide. Given the excellent thermal conductivity of silicon with even the slightest doping, we anticipate that the endface damage in these fused silica devices is likely due to substantial thermally-induced stress from heating at the grind and polish edge. While the sample is continually sprayed with water during the polishing process to wash away debris and dissipate heat, it is likely that considerable polishing recipe development is necessary to eliminate this thin-film fracturing. Given that a design using grating-coupling would eliminate the need for endface polishing, it is an attractive option, but at a significant compromise to coupling efficiency and to limited wavelength support, as compared to edge-coupling.

4.3.3 Conclusion

The notion of systems integration for dramatically improved single molecule analysis throughput remains a compelling and worthwhile technical challenge. Efforts discussed in this chapter have shown substantial improvements in our understand-

ing of the optical materials and design constraints necessary for these devices. We have explored numerous optical thin-films and shown that stoichmetric silicon nitride is among the best, given the collection of available materials, for creating high refractive-index optical waveguides with propagation support throughout the entire visible spectrum. We have demonstrated relatively moderate loss-waveguiding (5-10 dB/cm) in these nanophotonic components at the visible wavelengths of 488nm and 561nm. Our efforts have elucidated the overall system design challenges to operating these structures for the collection of faint, single molecule fluorescence signatures, and with some additional effort will likely yield a viable solution.

In more recent times, almost three years after the demonstrated design iterations one through three were performed, we have begun exploring this topic again with new insights and capabilities. While most of the lessons learned in previous iterations remain accurate, we have considerably improved in our ability to bond PDMS to glass. Additionally, with the increased literature on PDMS processing methods, we now possess an ability to form and place layers of PDMS ranging from 50-250 μm in thickness, which given the real refractive index of PDMS is nominally 1.36-1.40 at a 1:10 mixture composition, opens exciting possibilities. For example, using coverslip-corrected water immersion optics, PDMS could not be used in place of glass to overcome previous challenges in wafer bonding. The structural flexibility of PDMS could also enable valves, electrodes, and other functions to be integrated adjacent to a fused silica device with ultra-low autofluorescence.

We have also explored the use of lensed, SMF-28 optical fibers. Though these fibers are intended for single mode operation within the telecom c-band (1530-1570nm), their lens has proven to be an excellent method for injecting light into nitride waveguides more efficiently than previous results with straight-cleaved fibers, resulting in less coupling to the cladding and scattered light that could increase

autofluorescence. Overall, these findings emphasize that continued scientific and engineering design could enable a generation of completely integrated optical-fluidic devices that achieve single molecule detection for applications requiring high-throughput analysis.

References

[1] T. Thorsen, S. J. Maerkl, and S. R. Quake, "Microfluidic large-scale integration," *Science*, vol. 298, no. 5593, pp. 580–584, 2002.

[2] J. Han and H. G. Craighead, "Separation of long dna molecules in a microfabricated entropic trap array," *Science*, vol. 288, no. 5468, pp. 1026–1029, 2000.

[3] J. Y. Han and H. G. Craighead, "Characterization and optimization of an entropic trap for dna separation," *Analytical Chemistry*, vol. 74, no. 2, pp. 394–401, 2002.

[4] A. K. White, M. VanInsberghe, O. I. Petriv, M. Hamidi, D. Sikorski, M. A. Marra, J. Piret, S. Aparicio, and C. L. Hansen, "High-throughput microfluidic single-cell rt-qpcr," *Proceedings Of The National Academy Of Sciences Of The United States Of America*, vol. 108, no. 34, 2011.

[5] A. E. Cohen and W. E. Moerner, "Suppressing brownian motion of individual biomolecules in solution," *Proceedings Of The National Academy Of Sciences Of The United States Of America*, vol. 103, no. 12, pp. 4362–4365, 2006.

[6] A. E. Cohen and W. E. Moerner, "Controlling brownian motion of single protein molecules and single fluorophores in aqueous buffer," *Optics Express*, vol. 16, no. 10, pp. 6941–6956, 2008.

[7] M. J. Rust, M. Bates, and X. W. Zhuang, "Sub-diffraction-limit imaging by stochastic optical reconstruction microscopy (storm)," *Nature Methods*, vol. 3, no. 10, pp. 793–795, 2006.

[8] S. W. Hell, "Far-field optical nanoscopy," *Science*, vol. 316, no. 5828, pp. 1153–1158, 2007.

[9] S. Manley, J. M. Gillette, G. H. Patterson, H. Shroff, H. F. Hess, E. Betzig, and J. Lippincott-Schwartz, "High-density mapping of single-molecule trajectories with photoactivated localization microscopy," *Nature Methods*, vol. 5, no. 2, pp. 155–157, 2008.

[10] W. C. Chen, S. C. Lin, B. T. Dai, and M. S. Tsai, "Chemical mechanical polishing of low-dielectric-constant polymers: Hydrogen silsesquioxane and methyl silsesquioxane," *Journal Of The Electrochemical Society*, vol. 146, no. 8, pp. 3004–3008, 1999.

[11] K. Maex, M. R. Baklanov, D. Shamiryan, F. Iacopi, S. H. Brongersma, and Z. S. Yanovitskaya, "Low dielectric constant materials for microelectronics," *Journal Of Applied Physics*, vol. 93, no. 11, pp. 8793–8841, 2003.

[12] W. Henschel, Y. M. Georgiev, and H. Kurz, "Study of a high contrast process for hydrogen silsesquioxane as a negative tone electron beam resist," *Journal Of Vacuum Science and Technology B*, vol. 21, no. 5, pp. 2018–2025, 2003.

[13] F. van Delft, J. P. Weterings, A. K. van Langen-Suurling, and H. Romijn, "Hydrogen silsesquioxane/novolak bilayer resist for high aspect ratio nanoscale electron-beam lithography," *Journal Of Vacuum Science and Technology B*, vol. 18, no. 6, pp. 3419–3423, 2000.

[14] A. E. Grigorescu, M. C. van der Krogt, C. W. Hagen, and P. Kruit, "10 nm lines and spaces written in hsq, using electron beam lithography," *Microelectronic Engineering*, vol. 84, no. 5-8, pp. 822–824, 2007.

[15] S. Sivoththaman, R. Jeyakumar, L. Ren, and A. Nathan, "Characterization of low permittivity (low-k) polymeric dielectric films for low temperature device integration," *Journal Of Vacuum Science and Technology A-Vacuum Surfaces And Films*, vol. 20, no. 3, pp. 1149–1153, 2002.

[16] M. G. Albrecht and C. Blanchette, "Materials issues with thin film hydrogen silsesquioxane low k dielectrics," *Journal Of The Electrochemical Society*, vol. 145, no. 11, pp. 4019–4025, 1998.

[17] Y. X. Zeng, S. W. Russell, A. J. McKerrow, P. J. Chen, and T. L. Alford, "Thin film interaction between low-k dielectric hydrogen silsesquioxane (hsq) and ti barrier layer," *Thin Solid Films*, vol. 360, no. 1-2, pp. 283–292, 2000.

[18] S. K. Singh, A. A. Kumbhar, and R. O. Dusane, "Resisting oxygen plasma damage in low-k hydrogen silsesquioxane films by hydrogen plasma treatment," *Materials Letters*, vol. 60, no. 13-14, pp. 1579–1581, 2006.

[19] F. vanDelft, "Delay-time and aging effects on contrast and sensitivity of hydrogen silsesquioxane," *Journal Of Vacuum Science and Technology B*, vol. 20, no. 6, pp. 2932–2936, 2002.

[20] S. K. Singh, A. A. Kumbhar, and R. O. Dusane, "Repairing plasma-damaged low-k hsq films with trimethylchlorosilane treatment," *Materials Science And Engineering B-Solid State Materials For Advanced Technology*, vol. 127, no. 1, pp. 29–33, 2006.

[21] J. S. Jeng and J. S. Chen, "Characterization of the thermal reactions for cu/thermal sio2 and cu/hydrogen silsesquioxane on silicon," *Journal Of The Electrochemical Society*, vol. 148, no. 4, pp. G232–G236, 2001.

[22] S. M. Stavis, S. C. Corgie, B. R. Cipriany, and H. G. Craighead, "Single molecule analysis of bacterial polymerase chain reaction products in submicrometer fluidic channels," *Biomicrofluidics*, vol. 1, no. 3, 2007.

[23] R. Riehn, M. C. Lu, Y. M. Wang, S. F. Lim, E. C. Cox, and R. H. Austin, "Restriction mapping in nanofluidic devices," *Proceedings Of The National Academy Of Sciences Of The United States Of America*, vol. 102, no. 29, pp. 10012–10016, 2005.

[24] B. Ilic, Y. Yang, and H. G. Craighead, "Virus detection using nanoelectromechanical devices," *Applied Physics Letters*, vol. 85, no. 13, pp. 2604–2606, 2004.

[25] P. S. Waggoner and H. G. Craighead, "Micro- and nanomechanical sensors for environmental, chemical, and biological detection," *Lab On A Chip*, vol. 7, no. 10, pp. 1238–1255, 2007.

[26] F. Prieto, B. Sepulveda, A. Calle, A. Llobera, C. Dominguez, A. Abad, A. Montoya, and L. M. Lechuga, "An integrated optical interferometric nanodevice based on silicon technology for biosensor applications," *Nanotechnology*, vol. 14, no. 8, pp. 907–912, 2003.

[27] A. Ksendzov and Y. Lin, "Integrated optics ring-resonator sensors for protein detection," *Optics Letters*, vol. 30, no. 24, pp. 3344–3346, 2005.

[28] X. J. Zhou, J. M. Moran-Mirabal, H. G. Craighead, and P. L. McEuen, "Supported lipid bilayer/carbon nanotube hybrids," *Nature Nanotechnology*, vol. 2, no. 3, pp. 185–190, 2007.

[29] L. Larrimore, S. Nad, X. J. Zhou, H. Abruna, and P. L. McEuen, "Probing electrostatic potentials in solution with carbon nanotube transistors," *Nano Letters*, vol. 6, no. 7, pp. 1329–1333, 2006.

[30] K. L. Aubin, J. Huang, S. M. Park, Y. Yang, M. Kondratovich, H. G. Craighead, and B. R. Ilic, "Microfluidic encapsulated nanoelectromechanical resonators," *Journal Of Vacuum Science and Technology B*, vol. 25, no. 4, pp. 1171–1174, 2007.

[31] M. Godin, A. K. Bryan, T. P. Burg, K. Babcock, and S. R. Manalis, "Measuring the mass, density, and size of particles and cells using a suspended microchannel resonator," *Applied Physics Letters*, vol. 91, no. 12, 2007.

[32] S. Mandal and D. Erickson, "Nanoscale optofluidic sensor arrays," *Optics Express*, vol. 16, no. 3, pp. 1623–1631, 2008.

[33] A. Nitkowski, L. Chen, and M. Lipson, "Cavity-enhanced on-chip absorption spectroscopy using microring resonators," *Optics Express*, vol. 16, no. 16, pp. 11930–11936, 2008.

[34] J. Haisma, G. Spierings, T. M. Michielsen, and C. L. Adema, "Surface preparation and phenomenological aspects of direct bonding," *Philips Journal Of Research*, vol. 49, no. 1-2, pp. 23–46, 1995.

[35] P. M. Lundquist, C. F. Zhong, P. Q. Zhao, A. B. Tomaney, P. S. Peluso, J. Dixon, B. Bettman, Y. Lacroix, D. P. Kwo, E. McCullough, M. Maxham, K. Hester, P. McNitt, D. M. Grey, C. Henriquez, M. Foquet, S. W. Turner, and D. Zaccarin, "Parallel confocal detection of single molecules in real time," *Optics Letters*, vol. 33, no. 9, pp. 1026–1028, 2008.

[36] D. B. Wolfe, R. S. Conroy, P. Garstecki, B. T. Mayers, M. A. Fischbach, K. E. Paul, M. Prentiss, and G. M. Whitesides, "Dynamic control of liquid-core/liquid-cladding optical waveguides," *Proceedings Of The National Academy Of Sciences Of The United States Of America*, vol. 101, no. 34, pp. 12434–12438, 2004.

[37] D. B. Wolfe, D. V. Vezenov, B. T. Mayers, G. M. Whitesides, R. S. Conroy, and M. G. Prentiss, "Diffusion-controlled optical elements for optofluidics," *Applied Physics Letters*, vol. 87, no. 18, 2005.

[38] S. K. Y. Tang, C. A. Stan, and G. M. Whitesides, "Dynamically reconfigurable liquid-core liquid-cladding lens in a microfluidic channel," *Lab On A Chip*, vol. 8, no. 3, pp. 395–401, 2008.

[39] E. Schonbrun, W. N. Ye, and K. B. Crozier, "Scanning microscopy using a short-focal-length fresnel zone plate," *Optics Letters*, vol. 34, no. 14, pp. 2228–2230, 2009.

[40] E. Schonbrun, A. R. Abate, P. E. Steinvurzel, D. A. Weitz, and K. B. Crozier, "High-throughput fluorescence detection using an integrated zone-plate array," *Lab on a Chip*, vol. 10, no. 7, pp. 852–856, 2010.

[41] D. L. Yin, J. P. Barber, A. R. Hawkins, and H. Schmidt, "Waveguide loss optimization in hollow-core arrow waveguides," *Optics Express*, vol. 13, no. 23, pp. 9331–9336, 2005.

[42] P. Measor, L. Seballos, D. L. Yin, J. Z. Zhang, E. J. Lunt, A. R. Hawkins, and H. Schmidt, "On-chip surface-enhanced raman scattering detection using integrated liquid-core waveguides," *Applied Physics Letters*, vol. 90, no. 21, 2007.

[43] H. Schmidt and A. R. Hawkins, "Optofluidic waveguides: I. concepts and implementations," *Microfluidics And Nanofluidics*, vol. 4, no. 1-2, pp. 3–16, 2008.

CHAPTER 5

CONCLUDING REMARKS AND FUTURE PERSPECTIVES

Studies at the single molecule level provide access to the fundamental unit of biochemistry to explore the staggering heterogeneity of biological systems and to identify those molecules involved in critical life processes. While numerous methods exist for single molecule measurements of binding force, electrical charge, and Raman scattering, this dissertation has focused on the development of fluorescence-detection of individual molecules within miniaturized fluidic and optical systems. Application of these systems to the study of chromatin has remained unexplored. Until now, studies of DNA and chromatin epigenetic status have been performed using serial immunoprecipitation steps on the genetic material from millions of cells.

The purpose of this dissertation is to demonstrate the applicability and utility of nanofluidic systems to study epigenetic status at a single molecule level. This dissertation has demonstrated the development of tools for detection, quantification, selection, and recovery of individual molecules bearing specific epigenetic modifications. This is the first demonstration of an approach that can provide these functionalities at a single molecule level, thus opening the possibility for simultaneous detection of multiple epigenetic marks to elucidate the complex regulatory pathways of the epigenome. As an indirect result, efforts accompanying this dissertation have also demonstrated the ability to use nanofluidic systems for the study of DNA amplification [1], cellulase proteins [2], and RNA aptamers (in progress) to establish a broad-basis of utility for analytical studies at the single molecule level. The method of real-time molecule sorting, initially developed to collect molecules of specific epigenetic modification, represents a building block for preparative single molecule manipulation, opening new possibilities for

selecting and recovering femotgram to picogram quantities of genetic material. This approach is adaptable to variety of fluorescence-activated biomolecule separations. Considerable effort has also been focused on scaling and integrating these nanofluidic tools to achieve high-throughput detection, increasing their relevance for genome-wide studies. This effort has focused on combining materials (HSQ, silicon nitride, etc), fabrication methods, and optical waveguides to achieve systems integration of both optical excitation and fluorescence collection.

Future development of these single molecule technologies could include its application to explore mRNA copy number variations from within a single cell leading to an analysis of genetic expression; detection and selection of chromatin bearing multiple epigenetic marks followed by DNA sequencing; and massively-parallel detection and sorting of individual aptamer molecules from vast libraries of unique sequences. These approaches would be valuable as diagnostics that provide real-time analysis of each and every molecule from a sample to perform early detection of cancer, identification of genetic predisposition to disease, or rapid search for new drug targets. Given the existing infrastructure of the semiconductor industry for constructing these devices, the growing selection of inexpensive and powerful computational systems, the ever improving detector technologies, and new tools for modeling and layout of these devices, it is my hope and belief that these miniaturized analytical and preparative tools will find ubiquitous application in the near future.

Throughout the course of my PhD, I have become increasingly interested in the use of computational and mathematical models as predictive tools to guide the study and application of nanotechnology. While my training as an experimentalist has been most rewarding and empowered me with a strong sense of guided intuition about the physical world, my experiences have clarified the inherently complex na-

ture of physical processes at the nanoscale. At this scale, boundary properties blur the line between physically-descriptive equations and their relevant boundary conditions. As physicists and engineers, we are trained in the importance of scaling and simplifying our descriptions of the physical world to the most relevant dimension; however, balancing these considerations in multi-disciplinary applications of nanotechnology poses a particularly fascinating challenge that tends to span multiple relevant scales. In my observation, our ability to control and interrogate the physical and chemical properties at these boundaries will continually improve our ability to generate predictive mathematical models. In this fashion, it is my belief that future advancements in nanoscale science will benefit greatly by blurring traditional academic lines, encouraging cooperative development of predictive computational models and empirically-derived observations to achieve rapid convergence in our understanding. In my mind, I view this circumstance as having analogy to the Mobius Strip, a mathematical topology made popular by the Dutch artist M.C. Escher for his seamless blurring of mathematical and physical reality. This topology has only one boundary and is equivalent to a circle, so while it may appear that theoretical and experimental excursions are guided along different paths at the edge of the Mobius Strip they actually copropagate to form a complete picture of the nanoscopic world. So while this dissertation concludes my journey as a PhD student, it also marks the beginning of my fascinating and exciting future in science.

References

[1] S. M. Stavis, S. C. Corgie, B. R. Cipriany, H. G. Craighead, and L. P. Walker, "Single molecule analysis of bacterial polymerase chain reaction products in submicrometer fluidic channels," *Biomicrofluidics*, vol. 1, no. 3, 2007.

[2] J. M. Moran-Mirabal, S. C. Corgie, J. C. Bolewski, H. M. Smith, B. R. Cipriany, H. G. Craighead, and L. P. Walker, "Labeling and purification of cellulose-binding proteins for high resolution fluorescence applications," *Analytical Chemistry*, vol. 81, no. 19, pp. 7981–7987, 2009.